Magnetic resonance imaging of tumour biomarkers in ovarian cancer

Surrin Shazam Deen

Trinity Hall

05/09/2019

This dissertation is submitted for the degree of

Doctor of Philosophy

Declaration

This dissertation is the result of my own work and includes nothing which is the outcome of work done in collaboration except as declared in the Preface and specified in the text.

It is not substantially the same as any that I have submitted, or, is being concurrently submitted for a degree or diploma or other qualification at the University of Cambridge or any other University or similar institution except as declared in the Preface and specified in the text. I further state that no substantial part of my dissertation has already been submitted, or, is being concurrently submitted for any such degree, diploma or other qualification at the University of Cambridge or any other University or similar institution except as declared in the Preface and specified in the text. It does not exceed the prescribed word limit for the relevant Degree Committee.

TABLE OF CONTENTS

Preface

This PhD was designed to investigate the use of novel magnetic resonance imaging methods in ovarian cancer. Funding was provided by Cancer Research UK (CRUK), the CRUK Cambridge Centre, the Gates Cambridge Foundation, National Institute of Health Research-Cambridge Biomedical Research Centre, The Human Research Tissue Bank of Cambridge University Hospitals NHS Foundation Trust, Cancer Research UK/Engineering and Physical Sciences Research Council Imaging Centre in Cambridge and Manchester, The Medical Research Council (MRC), Addenbrooke's Charitable Trust and the Cambridge Experimental Cancer Medicine Centre.

Support with imaging (operation of the MRI scanner) was obtained from Dr Mary McLean (proton, sodium and carbon-13 imaging) and Dr Frank Riemer (sodium imaging) both of whom work at University of Cambridge Department of Radiology with additional support from the MRI radiographers employed at Addenbrooke's hospital.

The construction of carbon-13 images and the post-processing of carbon-13 data to produce quantitative maps was done by Dr Mary McLean. The post-processing of diffusion data to produce diffusion parameter maps was performed by Dr Andrew Priest from Cambridge University Hospitals NHS Foundation Trust Department of Radiology. For sodium imaging assistance was provided by Dr Frank Riemer and Dr Andrew Gill from the University of Cambridge Department of Radiology in creating the software for post-processing of the images. Dr Joshua Kaggie operated the MRI scanner for the MR fingerprinting mentioned in Chapter 10 and also carried out the post-processing of this data into T_1, T_2 and proton density maps.

Histological and immunohistochemistry staining of tissue samples was performed by laboratory staff at The Human Research Tissue Bank of Cambridge University Hospitals NHS Foundation Trust and the Cancer Research UK (CRUK) Cambridge Institute Histopathology and in situ hybridization core facility. Quantification of stains was performed with the assistance of Mrs Cara Brodie of the Cancer Research UK (CRUK) Cambridge Institute.

Dr Ferdia Gallagher from the University of Cambridge Department of Radiology assisted with checking the positioning of region of interest outlines. No advanced statistical methods

were required during this PhD work however advice on simple statistical methods was provided by Dr Andrew Gill.

The supervisors for this PhD and its associated research work were Dr Ferdia Gallagher and Dr James Brenton from Cancer Research UK (CRUK) Cambridge Institute.

The following publications and presentations have originated from this PhD

Surrin S. Deen, Andrew N. Priest, Mary A. McLean, Andrew B. Gill, Cara Brodie, Robin Crawford, John Latimer, Peter Baldwin, Helena M. Earl, Christine Parkinson, Sarah Smith, Charlotte Hodgkin, Ilse Patterson, Helen Addley, Susan Freeman, Penny Moyle, Mercedes Jimenez-Linan, Martin J. Graves, Evis Sala, James D. Brenton, Ferdia A. Gallagher. "Diffusion kurtosis MRI as a predictive biomarker of response to neoadjuvant chemotherapy in high grade serous ovarian cancer." *Scientific reports* 9, no. 1 (2019): 10742.

Surrin S. Deen, Frank Riemer, Mary A. McLean, Andrew B. Gill, Joshua D. Kaggie, James T. Grist, Robin Crawford, John Latimer, Peter Baldwin, Helena M. Earl, Christine A. Parkinson, Sarah A. Smith, Charlotte Hodgkin, Elizabeth Moore, Mercedes Jimenez-Linan, Cara R. Brodie, Helen C. Addley, Susan J. Freeman, Penelope L. Moyle, Evis Sala, Martin J. Graves, James D. Brenton, Ferdia A. Gallagher. (2019). Sodium MRI with 3D-cones as a measure of tumour cellularity in high grade serous ovarian cancer. *European Journal of Radiology Open*. 6. 10.1016/j.ejro.2019.04.001.

Joshua D. Kaggie, Surrin Deen, Dimitri A. Kessler, Mary A. McLean, Guido Buonincontri, Rolf F. Schulte, Helen Addley, Evis Sala, James D. Brenton, Ferdia A. Gallagher. "Feasibility of Quantitative Magnetic Resonance Fingerprinting in Ovarian Tumours for T1 and T2 Mapping in a PET/MR Setting." *IEEE Transactions on Radiation and Plasma Medical Sciences* (2019).

Surrin Deen, Andrew N Priest, Mary A McLean, Andrew B Gill, Helena Earl, Christine Parkinson, Sarah Smith, Robin Crawford, John Latimer, Peter Baldwin, Helen Addley, Susan Freeman, Charlotte Hodgkin, Ilse Patterson, Mercedes Jimenez-Linan, James Brenton, and Ferdia Gallagher. Diffusion kurtosis imaging for the diagnosis and prediction of response to treatment in high grade serous ovarian cancer. 2018. Electronic Poster. Joint annual meeting ISMRM-ESMRMB.

Surrin Deen, Andrew Priest, Mary Mclean, John Griffiths, James Brenton, Ferdia Gallagher. The repeatability of magnetization transfer imaging in the healthy female pelvis. 2016. Presentation at British Chapter of ISMRM Postgraduate Meeting.

Glossary of terms

ADC	apparent diffusion coefficient
ADP	Adenosine diphosphate
AFP	alpha fetoprotein
ALT	alanine transaminase
ATP	Adenosine triphosphate
AUC	area under the curve
beta-hCG	beta human chorionic gonadotrophin
BM	Basement membrane
CA	Carbonic anhydrase
CA 125	cancer antigen 125
CBAL	Core Biochemical Assay Laboratory)
CMO	Chief Medical Officer
COV	coefficient of variation
CR	Complete Response
CRUK	Cancer Research UK
CT	Computed tomography
D_{app}	apparent diffusion
DKI	Diffusion kurtosis imaging
DNA	Deoxyribonucleic acid
DNP	dynamic nuclear polarization
DWI	Diffusion weighted imaging
ECM	Extracellular matrix
ECOG	Eastern Cooperative Oncology Group
EPA	electron paramagnetic agent
ETC	electron transport chain
EV_f	extracellular volume fraction
FA	Flip angle

FDG-PET	fluorodeoxyglucose positron emission tomography
^{18}F-FDG	^{18}F-fluorodeoxyglucose
^{18}F-FDG-PET	^{18}F-fluorodeoxyglucose positron emission tomography
FIGO	Fédération Internationale de Gynécologie et d'Obstétrique
FoV	field of view
FSPGE	fast spoiled gradient echo
FWHM	Full width at half maximun
GCP	Good clinical practice
GE	gradient echo
GE	General electric
GLUT	Glucose transporter
GTP	Guanosine triphosphate
H&E	haematoxylin and eosin
HGSOC	high grade serous ovarian cancer
HP ^{13}C-MRI	Hyperpolarized carbon-13 magnetic resonance imaging
HP ^{13}C-MRI	Hyperpolarized carbon-13 MRI
ICC	Intraclass correlation coefficient
ICH	International conference on harmonisation
IHC	immunohistochemistry
IR	Inversion recovery
IT	inversion time
IV	intravenous
IV_f	intracellular volume fraction
IWS	intracellular weighted sodium
K_{app}	apparent kurtosis
k_{PL}	Rate constant for pyruvate to lactate exchange
LDH	Lactate dehydrogenase
MCT	monocarboxylate transporter
MISSION-Ovary	(Molecular Imaging and Spectroscopy with Stable Isotopes in Oncology and Neurology - Ovary

MR	Magnetic resonance
MRC	Medical Research Council
MRF	magnetic resonance fingerprinting
MRI	Magnetic resonance imaging
MT	Magnetization transfer
MTR	magnetization transfer ratio
NACT	neoadjuvant chemotherapy
NAD^+	Nicotinamide adenine dinucleotide (oxidized form)
NADH	Nicotinamide adenine dinucleotide (reduced form)
$[Na^+_{EC}]$	Extracellular sodium concentration
$[Na^+_{IC}]$	Intracellular sodium concentration
^{23}Na-MRI	Sodium magnetic resonance imaging
NAWM	normal appearing white matter
NEX	number of excitations
NHS	National Health Service
OECD	Organisation for Economic Co-operation and Development
PARP	poly ADP-ribose polymerase
PARPi	PARP inhibitor
PCOD	Polycystic ovarian disease
PD	Progressive Disease
PD	Proton density
PDC	Pyruvate dehydrogenase complex
PDH	dehydrogenase enzyme complex
PET	Positron emission tomography
PID	pelvic inflammatory disease
PIS	Patient information sheet
PR	Partial Response
rB1	Relative B1
REC	Research Ethics Committee
RECIST	Response Evaluation Criteria In Solid Tumours

RF	radiofrequency
RMI	risk of malignancy index
RMS COV	root mean square coefficient of variation
ROCA	risk of ovarian cancer algorithm
ROI	Region of interest
RRID	Research Resource Identifier
S	signal
S.D.	standard deviation
SD	Stable Disease
SNR	Signal to noise
SoS	stack-of-stars
SSFP	Steady-state free precession
SUV	standardized uptake value
SUV_{max}	Maximum standardized uptake value
T_1W	T_1-weighted
T_2W	T_2-weighted
TCA	Tricarboxylic acid
TE	Echo time
TR	Repetition time
TSC	Tissue sodium concentration
TSC	tissue sodium concentration
US	ultrasound
UTE	ultra-short echo time
VEGF	Vascular endothelial growth factor
VOI	volume of interest
α	Flip angle
α_{true}	True flip angle
ρ_c	cellular density

Chapter 1

Research aims and study design

1.1 Background

Ovarian cancer has the highest mortality of any gynaecologic cancer in the developed world. In the UK, the Chief Medical Officer (CMO) reported 4,227 deaths from the condition in 2016. Mortality from ovarian cancer in the UK is among the highest for OECD (Organisation for Economic Co-operation and Development) nations, with a 5-year survival rate of only 36% (1). In the UK, ovarian cancer currently accounts for 5% of all female cancer deaths, making it the fifth-most lethal cancer in women (2). Over 7,000 new cases of ovarian cancer are currently diagnosed each year and 90% of these new cases are of the epithelial subtype, the deadliest form of ovarian cancer.

Several new magnetic resonance imaging techniques in cancer have recently been shown to have clinical relevance for the detection, management and monitoring of malignancies. For example, diffusion kurtosis imaging (DKI) in glioma has been shown to differentiate high grade from low grade disease (3, 4), sodium imaging in the brain and breast is able to differentiate cancerous from normal tissue (5, 6) and one study showed that hyperpolarized carbon-13 MRI in the prostate may be more sensitive than proton MRI at detecting malignancies (7). Evidence is also emerging that some older magnetic resonance imaging techniques like magnetization transfer (MT) imaging may have a role in clinical medicine for imaging microstructural cancer properties like fibrosis (8). One of the newest forms of MRI, magnetic resonance fingerprinting (MRF) has also demonstrated the ability to accelerate image acquisition which could aid clinical translation for a range of different proton MRI techniques (9).

Despite the promise of these magnetic resonance imaging methods, there has been a lack of application of these techniques to ovarian cancer. This is despite ovarian cancer being

acknowledged as a cancer where improvements in care are desperately required (10). The reasons behind the lack of usage of new imaging in ovarian cancer are not clear but may relate to the difficulty of imaging a large, complex anatomical area such as the abdomen and pelvis and to the lack of definitive evidence of clinically relevant information that may be gained from novel imaging techniques that can influence the limited management options currently available for ovarian cancer patients.

1.2 Aims of this research

The overarching aim of this PhD was to recruit a cohort of patients with ovarian cancer and to evaluate on the ovarian cancer lesions of these patients the use of metabolic and microstructural imaging techniques that have previously shown promise for clinical applications in oncology.

Secondary aims of this PhD were: to demonstrate the feasibility of imaging in a clinical setting for those techniques that had never previously been applied to ovarian cancer, and for all the techniques evaluated apart from MRF: to find correlations of the ovarian cancer tissue properties and patient demographics with the imaging results.

The reason these aims were chosen was because of the perceived need by the research team for an improvement in the treatment of ovarian cancer that could potentially come from a better understand of *in vivo* ovarian cancer biology provided by imaging. It was also felt that a furthering of knowledge about the biological origin of the imaging signal for the various techniques from a comparison with ovarian cancer tissue could help to identify future clinical applications for the imaging.

The imaging techniques selected for this study were DKI, sodium MRI, MT imaging, hyperpolarized carbon-13 MRI and MRF. These were selected as they have all shown potential for clinical applications in cancer imaging but have not yet been fully explored for their utility in the assessment of ovarian cancer or any sub-population of ovarian cancer patients. The use of these techniques in ovarian cancer therefore represent a gap in scientific knowledge which this PhD seeks to help address.

1.3 Study design and protocol

The patient imaging in this study was performed as part of the MISSION-Ovary (Molecular Imaging and Spectroscopy with Stable Isotopes in Oncology and Neurology - Ovary) clinical study. Much of the first year of this PhD was spent designing the protocol for MISSION-ovary and gaining ethical approval for the study, in addition to performing some related in vitro cell experiments that are presented in Chapter 8.

MISSION-ovary was primarily funded by a grant from Cancer Research UK but also benefitted from the use of equipment and the assistant of staff funded by the Wellcome Trust. MISSION-ovary was designed around hyperpolarized carbon-13 imaging in high grade serous ovarian cancer (HGSOC) patients, with permission also obtained from the ethics committee and sponsors for non-invasive proton imaging, sodium imaging and FDG-PET (fluorodeoxyglucose positron emission tomography) imaging.

Hyperpolarized carbon-13 MRI was initially intended as the primary research focus of this PhD as based on pre-clinical trials this imaging technique had the potential for the most clinically impactful results, including the non-invasive mapping of *in vivo* enzyme activity (11) and the early detection of response to cancer treatment (12). Unfortunately, due to global shortages in the specialist materials like the clinical grade carbon-13 labelled molecules required for hyperpolarized carbon-13 imaging and because of the time constraints for completing this PhD, the focus of this research project shifted more towards proton and sodium imaging than carbon-13 imaging as time progressed.

The MISSION-ovary study protocol nevertheless was still used to outline the eligibility criteria for participants, patient recruitment methods, the time points of imaging and tissue collection during the treatment course and the general tissue analysis methods that would be used for the alternative imaging techniques evaluated in this PhD in place of hyperpolarized carbon-13 MRI.

The protocol for MISSION-ovary was reviewed and approved by the South Cambridge Research Ethics Committee (REC). Patients with ovarian masses were identified through the gynaecological oncology multidisciplinary team meetings and clinics at Cambridge University Hospitals NHS Foundation Trust, Addenbrooke's hospital. The clinical team was responsible for the initial approach to patients and for determining whether patients might be suitable

for participation. If deemed suitable be the clinical team, potential participants were then offered a meeting with researchers to discuss the details of the research study further.

To be included in the study the patients needed to meet the following inclusion criteria:

1. Be 18 years or older.
2. Have a confirmed or likely diagnosis of HGSOC.
3. Be aware of their diagnosis.
4. Be a likely surgical candidate who is fit for possible surgery.
5. Have no contraindications to the use of the intravenous contrast agents involved in the study.
6. Be able to provide written informed consent according to ICH (International conference on harmonisation), GCP (good clinical practice), national and local regulations.
7. Have a negative pregnancy test, either urinary or blood prior to enrolment if of childbearing potential.
8. Have ECOG (Eastern Cooperative Oncology Group) performance status 0 or 1.
9. Express willingness and ability to comply with scheduled visits, laboratory tests, imaging and other study procedures.

The following criteria excluded patients from the study:

1. Any disorder that could adversely affect levels of pyruvate or lactate such as diabetes mellitus.
2. The use of medications that may affect levels of pyruvate or lactate such as metformin or insulin.
3. Known allergy or adverse reaction to any of the injected contrast agents proposed for use in the study.
4. Pregnancy or breastfeeding.

5. Other severe acute or chronic medical or psychiatric conditions that may increase the risk associated with study participation or in the judgement of the investigators make it undesirable for the patient to enter the study.
6. Laboratory abnormalities that may have an unknown or unpredictable impact on study results.
7. Unsuitability for magnetic resonance imaging e.g. severe obesity, inability to lie still or contraindicated metal implants such as the intrauterine contraceptive device.

Permission was also obtained from the REC to collect tissue before and after imaging via percutaneous biopsy or a surgical procedure. The approved study protocol detailed the main analytic methods to be applied to tissue including genetic profiling, histology and immunohistochemistry.

1.4 Research team members and roles

Due to the multidisciplinary nature of imaging in oncology and the specialist types of imaging evaluated here, a large and diverse team was involved in the MISSION-ovary research project and this PhD. The contributing research team included physicists, oncologists, surgeons, radiologists, pathologists, nurses, radiographers and laboratory technicians.

After study approval by the REC, my role as a PhD student included the overall co-ordination of study activities. I was the primary person responsible for identifying participants, explaining the study and providing the patient information sheet (PIS) to potential participants. I also contacted the patients to elicit their final decision on participation, liaised with the radiology department to book scans, arranged supporting staff such as radiographers and physicists to be present to assist with imaging at the scheduled scan dates, assisted with the collection of tissue at surgery, transferred tissue that was collected for further laboratory analysis, analysed the imaging and tissue measurement results, performed the statistical analyses on the data obtained and interpreted the study results.

Assistance was obtained with recruitment primarily from the oncologists and surgeons of the gynaecologic oncology team at Addenbrooke's Hospital who initially approached potential participants with the invitation to take part and to speak to a researcher for more study details. Consultant radiologists from the Department of Radiology obtained image guided percutaneous biopsies from patients for use in research. The surgeons collected further, larger tissue specimens in theatre for research. Tissue samples were either frozen or fixed in paraffin at the Addenbrooke's Tissue Bank by the Tissue Bank staff. Tissue bank staff also sectioned and stained tissue for histology and IHC as requested by the research team for the various MISSION-ovary imaging types. Additional IHC stains were performed by the Cancer Research UK, Cambridge Institute Histopathology and in situ hybridization core facility through the Brenton lab.

Assistance with the operation of the MRI and PET scanners was obtained from radiographers and physicists at the Department of Radiology. Physicists from the department also assisted with the post-processing of imaging data including providing the Matlab code for the construction of diffusion parameter maps, sodium concentration maps, carbon-13 parameter maps and MRF maps. The respective individuals and their specific contributions are detailed in the relevant sections of the later Chapters of this dissertation which is divided according to imaging modality.

Chapter 2

Ovarian cancer biology and current imaging techniques

2.1 Introduction

In order to identify which patient demographics and biological properties of ovarian cancer it would be best to measure for comparison with each imaging technique studied here, it is essential to first understand ovarian cancer biology and the theory behind the imaging methods being employed. This chapter therefore summarises the current body of knowledge about ovarian cancer and the imaging techniques being explored in this PhD. The dissertation then goes on during subsequent chapters to look at each imaging technique in more detail and to provide results from human participants and preclinical experiments where relevant.

2.2 Ovarian cancer origin and development

Ovarian cancer like other cancers is caused by dysfunctions in the regulation of the cell cycle and other cellular processes, leading to uncontrolled replication and a build-up of excess cancer cells. The malignant transformation can include genetic changes and leads to cellular properties and behaviours that promote cancer progression such as a loss of contact inhibition between neighbouring cells, failure of the G_1-S or G_2 checkpoints of the cell cycle, an inability to enter the quiescent G_0 phase after mitosis (13), metabolic alterations and angiogenesis.

Multiple endogenous and environmental factors can contribute to an increased risk of ovarian cancer. Any factor that increases the rate of DNA replication in the ovaries or fallopian tube increases the risk that a DNA replication error can occur that may affect the

cell cycle and lead to cancer. For example, a greater number of ovulations increases the number of cell divisions that will have to occur in the ovaries to repair the corpus luteum after each ovulation. Hormones that stimulate growth and activity of the ovaries such as oestrogen can similarly cause an escalation of the risk for developing cancer. Germline genetic mutations and exposure to carcinogens that damage DNA are other common ovarian cancer risk factors. Table 2.1 gives a more comprehensive list of the risk factors for developing ovarian cancer.

Risk factors for the development of ovarian cancer

1. Nulliparity
2. *TP53* mutation
3. *BRCA1* and *BRCA2* germline mutations.
4. Conditions like endometriosis, polycystic ovarian disease (PCOD) and obesity which increase the levels of hormones that stimulate ovarian cell proliferation.
5. Early menarche or late menopause due to a larger number of ovulations during the lifetime.
6. The use of hormone replacement therapy.
7. A family history of cancers such as endometrial, colon or gastrointestinal cancers which may indicate the presence of syndromes that are associated with ovarian cancer like hereditary non-polyposis colorectal cancer or Lynch syndrome.
8. Peutz–Jeghers syndrome.
9. Icelandic, Hungarian, European Jewish and Ashkenazi Jewish descent.
10. Environmental factors possibly related to diet and socio-economic class. Ovarian cancer is more common in industralised nations and has 30-40% higher prevalence in the white population when compared to the black and Hispanic populations of the USA.
11. Older age up to 80 years after which risk declines possible due to hormonal changes associated with menopause.
12. Breast cancer or a family history of breast cancer since many of the risk factors for breast cancer and ovarian cancer overlap.
13. A family history of ovarian cancer.

Table 2.1: Risk factors for developing ovarian cancer

The risk of developing ovarian cancer can be reduced by any event that lessens the number of ovulations over an individual's lifetime, by the avoidance of exposure to carcinogens, and by reduced exposure to hormones that cause ovarian growth (14). Some factors that protect against the development of ovarian cancer are given in Table 2.2.

Factors that protect against the development of ovarian cancer

1. Use of the oral contraceptive pill especially the progesterone only pill.
2. Breastfeeding.
3. Pregnancy.
4. Hysterectomy or tubal ligation since this prevents the passage of carcinogens through the fallopian tubes and to the ovaries.
5. A low-fat diet.
6. Sterility.

Table 2.2: Protective factors against the development of ovarian cancer

2.3 Ovarian cancer tumour classification

Ovarian cancer develops most commonly from epithelial cells, germ cells or stroma cells in the female reproductive tract. The World Health Organization (WHO) classifies ovarian tumours into the following six categories: serous, mucinious, seromucinous, endometroid, clear cell and Brenner tumours (15). Tumours of epithelial origin make up around 90% of ovarian cancers and include the serous, clear cell, mucinous and Brenner tumours. Of the epithelial tumours, serous cancers are the most frequently occurring (16). Primary peritoneal cancer is similar to epithelial ovarian cancer and is treated in the same way. After epithelial tumours, the next most common cell of origin of ovarian cancers are the germ cells. Germ cell tumours include teratoma, dysgerminoma and choriocarcinoma (17). Stromal tumours occur less frequently and include fibroma, granulosa-theca cell tumours and metastatic lesions to the ovaries.

Definitive diagnosis of ovarian cancer subtype is by histology and immunohistochemistry (IHC) staining. Serum tumour biomarkers and imaging also play a role clinically in determining cancer subtype, particularly in cases where biopsy is not possible. Diagnosis of disease subtype is essential for determining the optimal cancer treatment and is usually performed with a combination of histological analysis and imaging.

2.4 Ovarian cancer staging

Ovarian cancer is staged according to the FIGO (Fédération Internationale de Gynécologie et d'Obstétrique) classification (18). There are four numbered stages of the disease. In Stage 1 the cancer is confined to the ovaries. In Stage 2 there is spread of cancer to the pelvis or peritoneum but nowhere else in the abdomen. At Stage 3 the cancer has spread out of the pelvis or it has spread to the retroperitoneal lymph nodes in the abdomen. In Stage 4 disease there are metastases to areas of the abdomen that are outside the peritoneum or the liver and spleen capsule. The stages of ovarian cancer can be further subdivided as outlined in Table 2.3.

Stage	Description
1a	The cancer is inside only one ovary, which has an intact capsule.
1b	The cancer is present in both ovaries but still confined to the insides i.e. both capsules are intact.
1c	There is cancer in one or both ovaries as well as cancer on the surface of one or both ovaries. If no cancer is detected on the surface of an ovary a classification of Stage 1c can also be made if there are cancer cells in ascitic fluid, washings or spillage of the cancer at surgery.
2a	There is spread of cancer to the fallopian tubes or uterus.
2b	There is spread to other tissues in the pelvis not included in 2a such as the bladder or rectum.
2c	The cancer meets the criteria for 2b classification and there are cancer cells in abdominal ascitic fluid or washings.
3a	There is microscopic spread detectable in the peritoneum or cancer has spread to retroperitoneal lymph nodes.
3b	There are visible metastases to the peritoneum that are 2cm in diameter or less.
3c	Metastases larger than 2cm are present in the peritoneum, or metastases to liver or spleen capsule have occurred.
4	The metastases are more distant and occur for example in the lung or liver parenchyma. Stage 4 disease may also be diagnosed if metastases are confirmed to extra abdominal lymph nodes or the inguinal lymph nodes.

Table 2.3: Ovarian cancer staging

Stage of disease at the time of diagnosis is currently an important predictor of outcome in ovarian cancer. Imaging of the chest, abdomen and pelvis with contrast enhanced CT is the usual method of disease staging. Stage also affects management as it has an influence on suitability for surgery and on the goals of chemotherapy administration which may for example be either therapeutic or palliative.

2.5 Ovarian cancer presentation

The signs and symptoms of ovarian cancer can be very mild during the early stages of the disease but as it progresses lesions occupy more space and can spread to other parts of the body leading to more pronounced symptoms. Common presenting symptoms include discomfort in the lower abdomen, back or pelvis and a feeling of bloating and abdominal fullness (19). Pre-menopausal women sometimes experience irregular periods while post-menopausal women can have vaginal bleeding. As the lesion becomes large enough to compress nearby organs, there may be increased urinary frequency, constipation, bowel involvement, indigestion, early satiety, pain during intercourse and a noticeable lump or swelling of the abdomen or pelvis. The constitutional symptoms of cancer develop at later stages and include weight loss, anorexia, tiredness, malaise and possibly symptoms in distant organ systems due to metastases.

2.6 Serum tests

There is currently no appropriate screening test for ovarian cancer. Because of the vague nature of early symptoms, patients often present at a late stage. The first investigation in the diagnosis is a physical examination. This may reveal a palpable mass in the pelvis or abdomen, ascites or symptoms in other organ systems such as respiratory or neurological problems if the cancer has already metastasized at presentation.

The CA 125 (cancer antigen 125) blood test is performed if a suspicion of ovarian cancer has been raised from the history and examination of a patient. CA 125 is a protein that can be elevated in some types of ovarian cancer as well as other malignancies and several benign conditions. CA 125 is elevated in cancers of the ovaries, fallopian tubes, lungs, breast and gastrointestinal tract. It also goes up in endometriosis, leiomyoma, pelvic inflammatory disease (PID), salpingitis, menstruation, pregnancy, liver cirrhosis, pancreatitis, and inflammatory conditions of the abdomen. Serum CA 125 can also be used as a measure of treatment response and to screen for relapse in ovarian cancer patients (20).

When used to assess a patient with a pelvic mass, one study found an elevated CA 125 level above 30 U/ml had a sensitivity of 81% and specificity of 75% for detecting ovarian cancer (21). In patients with an average risk of ovarian cancer CA 125 is not considered to be a suitable screening test in isolation due to the high likelihood of falsely positive results that may lead to unnecessarily harmful and invasive procedures. Studies are ongoing to determine whether screening with CA 125 might be feasible in patients at a higher than average risk such as those with a strong family history of ovarian cancer or those who are known to have the *BRCA* mutation. Despite the difficulty in interpreting its value, CA 125 is still the most widely used blood marker for ovarian cancer and an important clinical question to address in the future would be the role of combining CA 125 with imaging or other novel technologies to assess for ovarian cancer more effectively in a multiparametric fashion.

There are several other less specific markers of ovarian cancer. NICE (National Institute for Health and Care Excellence) recommends "In women under 40 with suspected ovarian cancer, measure levels of alpha fetoprotein (AFP) and beta human chorionic gonadotrophin (beta-hCG) as well as serum CA 125, to identify women who may not have epithelial ovarian cancer" (22). Serum measurement of circulating tumour DNA is an emerging test that may also find a role in diagnosis and monitoring of ovarian and other cancers (23).

2.7 Diagnosis of ovarian cancer

Ultrasound (US) is the initial imaging test recommended to investigate a pelvic or adnexal mass. If the US result is indeterminate and there is a strong suspicion of cancer, CT (computed tomography) or MRI (magnetic resonance imaging) can be undertaken to provide more information on the nature of the mass.

On imaging, malignant lesions tend to be larger in size than benign lesions, they also display solid components of a heterogenous composition, contain internal structures if cystic, have lobulated shapes, contain areas of necrosis and blood vessels and can present with surrounding lymphadenopathy or peritoneal deposits visible on the imaging (24-26). MRI has been found to have a diagnostic accuracy of 88% to 93% at distinguishing between benign and malignant masses (27) and one study found that the sensitivity and specificity of

ultrasound for differentiating benign and malignant ovarian masses were 91% and 96% respectively (26).

If the ovarian mass is in a location that is amenable to biopsy, a histological diagnosis can be attempted. In cases where no mass is seen on imaging, abdominal paracentesis is sometimes carried out to look for cancer cells in ascitic fluid. Definitive diagnosis of ovarian cancer can only be made through cytology or histology performed on specimen samples obtained from surgery or biopsy. After a diagnosis of cancer has been confirmed, a staging CT of the chest, abdomen and pelvis is usually performed.

In cases where blood tests and imaging investigations do not lead to a clear diagnosis of ovarian cancer, risk scoring can be applied to determine the likelihood that the patient has ovarian cancer. The most widely used method of risk scoring in suspected ovarian cancer is the RMI (risk of malignancy index). RMI is calculated as follows:

RMI = ultrasound score x menopausal status x CA-125 level in U/ml

The ultrasound score is determined from the number of abnormalities found on US scan. An abnormality is defined as the presence of any of the following 5 findings: multilocular cysts, solid areas of malignancy, ascites, abdominal metastases and bilateral ovarian cysts or masses.

Zero abnormalities give an ultrasound score of 0

One abnormality gives an ultrasound score of 1

Two or more abnormalities give and ultrasound score of 3

For menopausal status:

Pre-menopausal women are given a menopausal status score of 1

Post-menopausal women are given a menopausal status score of 3

An RMI score over 200 is considered to indicate a high risk of malignancy (28).

The risk of ovarian cancer algorithm (ROCA) is an alternative scoring method that assesses the probability a patient has ovarian cancer. ROCA can be applied in lower risk cases prior to imaging and follows the CA-125 or other serum biomarker levels over time with serial blood tests. ROCA scoring recommends imaging when the calculated risk from serum biomarkers is high (29).

2.8 Ovarian cancer treatment

Treatment options for ovarian cancer include surgery and chemotherapy. The optimal treatment strategy for an individual patient depends on the disease subtype, stage at diagnosis and any existing co-morbidities. The type of surgery undertaken is usually determined by the extent and location of disease, particularly the relationship and proximity to surrounding structures like blood vessels that may be affected or damaged during an operation. In addition to removal of the pelvic mass, surgery usually involves lymph node biopsy, omentectomy, hysterectomy and bilateral salpingo-oophorectomy, unless there is a desire to retain fertility. When a patient is not suitable to undergo surgery or when surgery alone is not enough to remove all of the disease, chemotherapy treatment can also be applied. The majority of chemotherapy drugs in ovarian cancer are prescribed for epithelial ovarian cancer, which is most commonly high grade serous ovarian cancer.

For advanced ovarian cancer it is still unclear whether the best treatment strategy is primary debulking surgery followed by chemotherapy or neoadjuvant chemotherapy (NACT) followed by interval debulking surgery. When surgery leaves less than 1cm maximal diameter of residual disease it is considered optimal debulking (30). Primary debulking surgery attempts to remove cancerous tissue as the first therapeutic intervention following diagnosis. NACT on the other hand is chemotherapy given prior to surgical intervention. After NACT the patient is imaged to identify the current location of cancer and surgery is then performed to remove remaining cancer and is referred to as interval debulking surgery (IDS). IDS may be followed by further chemotherapy and surgery.

For ovarian tumour types that are known to be poorly chemosensitive, primary debulking surgery is a better option than NACT. For patients with poor performance status who may not be fit enough to withstand the insult of a major operation, NACT to reduce the tumour burden followed by interval debulking surgery is often a better option (31). The treatment for each individual patient is decided by a multidisciplinary team (MDT) comprising oncologists, surgeons, radiologists, histopathologists and allied health professionals.

2.9 High grade serous ovarian cancer

Serous ovarian cancer may be classified as low grade, high grade or indeterminate grade based on the nuclear grade of the cancer cells, with nuclear grade 1 classified as low grade, nuclear grade 2 classified as indeterminate and nuclear grade 3 classified as high grade. Recent studies have suggested that indeterminate grade may not represent a truly separate classification and some clinicians prefer to use a two tier classification comprised of only low and high grade (32).

Tumour grades are determined histologically according to the appearances of cells under light microscopy as follows:

GB: borderline cancer - cells appear borderline cancerous

G1: low grade - cells are well differentiated.

G2: intermediate grade - cells are moderately differentiated.

G3: high grade - cells are poorly differentiated.

GX: grade cannot be evaluated.

Mutations in the *KRAS*, *BRAF* and *ERBB2* genes are characteristics of low grade serous ovarian cancer (LGSOC) whereas *TP53* mutation is characteristic of HGSOC. The molecular genetic profiling and the behaviour of intermediate grade serous ovarian cancer is almost

the same as HGSOC and for this reason intermediate grade serous ovarian cancer is often classified as HGSOC (33). HGSOC affects older women in the peri-menopausal age range while LGSOC is more common in pre-menopausal women (34). HGSOC is more sensitive to chemotherapy while LGSOC is less responsive (35). The response of HGSOC to chemotherapy and the relationship of response to DKI is explored further in Chapter 3.

High grade serous ovarian cancer (HGSOC) is the most clinically important type of ovarian cancer due to its high prevalence and poor prognosis. LGSOC has a better outcome and distinguishing between these grades is therefore clinically important in planning treatment. Reasons for the poor outcomes in HGSOC patients include the aggressive nature of the disease, the late stage at which the disease is typically diagnosed and the lack of highly effective therapies.

HGSOC originates in the secretory cells of the fallopian tubes and metastasizes to the ovaries and peritoneum early on in its course. The stage of the disease at which diagnosis is confirmed has a significant impact on survival (36, 37). Approximately 90% of women who are diagnosed at FIGO stage 1 survive for five years. With diagnosis at stage 2 the 5-year survival decreases to 40%, at stage 3 survival is 20% and less than 5% for those diagnosed in stage 4 are alive after 5 years (14, 38). Currently, 70% of women with HGSOC are diagnosed at stages 3 or 4 resulting in overall statistics of less than half of women with HGSOC surviving for 5 years and around 75% dying within 10 years of the discovery that they have the disease.

For HGSOC, debulking surgery is performed either before or after chemotherapy. Patients with advanced disease may have several episodes of interval debulking surgery during the course of their chemotherapy treatment. Even with an optimal treatment regimen however, the relapse rate at six months in HGSOC patients is still around 30% and overall recurrence rates following chemotherapy and negative “second look” laparotomy are around 50% at 10 years (39). First-line chemotherapy treatment for HGSOC has not changed in the last 30 years and remains a combination of a platinum-based drug and a taxane. However, in relapsed disease a wider variety of drugs is available. The most common treatment in the UK for relapsed HGSOC is gemcitabine plus carboplatin but clinical recommendations also suggest consideration of doxorubicin, topotecan and trabectedin for advanced recurrent

disease and etoposide and cyclophosphamide as options for platinum resistant cases. Other drugs that have shown efficacy in the treatment of ovarian cancer but are still currently undergoing clinical trial evaluations include the VEGF (vascular endothelial growth factor) inhibitor bevacizumab, PARP (poly ADP-ribose polymerase) inhibitors and immunotherapy-based treatments.

2.10 Post-diagnosis imaging in ovarian cancer management

Although ultrasound is the first line imaging modality for assessing an adnexal mass, after the diagnosis of ovarian cancer has been made, it is necessary to also investigate neighbouring organs and bones for disease spread. In this role, CT is more suitable than US, as US is unable to adequately image some abdominal regions such as deeply placed tissue. CT is also required to assess the lungs, as metastases to the lungs often indicate inoperable disease that should be treated with chemotherapy alone.

In those patients being considered for surgical management, the identification of peritoneal spread and of lesions in the vicinity of the liver and spleen as well as mesenteric and bowel involvement are all important for surgical planning as these can affect outcome and some aspects of the surgery such as the need for bowel resection and the creation of a stoma (40). CT is the most commonly used imaging modality in surgical planning with MRI and PET occasionally also used to provide complementary information in cases where CT findings are indeterminate.

In those patients undergoing NACT treatment CT scanning is performed again after the cycle of chemotherapy just before surgery. This is done to monitor the changes caused by the chemotherapy and to plan surgery accordingly.

After surgery, clinic appointments are used to monitor for relapse. Patients are assessed for symptoms, have serum CA 125 measured and sometimes imaging is performed. There is variation in follow-up strategies across cancer networks in the UK (41). The majority of centers report offering follow-up appointments every 3 months for the first 2 years after treatment followed by every 6 months for the next 2 years (42). In relapsed ovarian cancer where there are a greater number of chemotherapy and anti-cancer drug options available,

the monitoring of response with CA 125 and CT imaging can be used to inform therapeutic choices.

2.11 Magnetic resonance imaging in ovarian cancer

Magnetic resonance imaging is able to offer a range of different contrasts that reflect diverse tissue properties. HGSOC is a heterogenous disease and methods of non-invasively probing tissue structure and function can uncover details about tumours that it would not be possible to detect with point biopsy samples alone. Imaging also has the advantage over histology in tumour evaluation that it causes minimal disturbance to the tissue environment.

Ovarian cancer is a difficult disease to image due to the location of the lesions in the pelvis and abdomen and the generally poor performance status of women with the condition. These challenges have contributed to many promising imaging techniques not being fully evaluated in ovarian cancer and there is consequently still significant room for improvements in clinical imaging tests. This PhD has applied novel and emerging imaging techniques to the study of ovarian cancer, with a focus on identifying specific clinical applications for high grade serous ovarian cancer. The methods explored include diffusion kurtosis imaging to investigate tissue heterogenity, sodium MRI to measure tumour cellularity, magnetization transfer imaging to assess the extracellular matrix, metabolic imaging with hyperpolarized carbon-13 MRI and positron emission tomography (PET), and magnetic resonance fingerprinting to map tumour relaxation parameters. The remaining sections in this chapter introduce these imaging techniques and their use to investigate ovarian cancer while subsequent chapters describe in greater detail the human results obtained for each imaging technique.

2.12 Diffusion weighted imaging in cancer

Diffusion weighted imaging (DWI) applies magnetic-field gradient pulses to sensitize the imaging signal to the microscopic motion of water molecules. In areas where there is minimal movement or diffusion of water, the net effect of these gradient pulses is small and the final signal recorded has a high value. In areas of tissue where there is a large amount of

diffusion, the movement causes partial dephasing of magnetizations and leaves a smaller residual signal. The strength of the diffusion sensitization in DWI is quantified by the b-value. DWI enjoys widespread use in oncology. In cancers increased cellularity obstructs the free movement of water and causes the cancerous lesions to appear brighter than surrounding healthy tissue.

For clinical use, it is typical to calculate an apparent diffusion coefficient (ADC) map from diffusion weighted images under the assumption that the water molecules diffuse in a Gaussian fashion. The ADC values for each voxel are found by fitting the signal strengths and b-values of the diffusion weighted images to the mono-exponential equation given below.

$$S(b) = S_0 \cdot \exp(-b \cdot ADC) \quad (2.1)$$

where S_0 is the DWI signal in the voxel under consideration with no diffusion sensitization (at b-value = 0 s/mm^2) and S(b) is the signal strength at the voxel on the DWI image taken with a b-value of b.

Diffusion kurtosis imaging (DKI) is a new method of diffusion modelling that includes fitting of the diffusion weighted MRI signal to the second term in the Taylor expansion of the expression relating diffusion weighted signal intensity to b-value. Inclusion of the second term in this expansion gives information on kurtosis of the signal (43). The use of DKI in ovarian cancer patients is explored further in Chapter 3.

2.13 Sodium imaging and physiological alterations in cancer

Sodium concentrations in cancer can be affected by changes in ion transport, perfusion and cellularity among other biological properties of tissue (44). MRI has the ability to quantify total tissue sodium concentration and intracellular sodium concentration due to a difference in relaxation times of intracellular and extracellular sodium (45, 46). Quantification of sodium with MRI may therefore provide information on several physiological processes in cancer (47).

In healthy tissue, the concentration of sodium differs between the intracellular and extracellular spaces. The exact values of sodium concentration in each compartment depends on tissue type and the physiological state of the tissue, but in most cases intracellular sodium concentration is around 5 to 15 mM (48) and extracellular sodium concentration is 135 to 150 mM. Higher cellularity increases the proportion of intracellular space while vascularity and oedema increase the extracellular volume. Tissue sodium concentration (TSC) is an average of the intracellular and extracellular sodium concentrations weighted according to the volumes of these two spaces.

It is energetically very favourable for the extracellular sodium ions to move intracellularly down their concentration gradient. The difference between the intracellular and extracellular sodium environments must therefore be actively maintained. The phospholipid bilayer of the cell membrane is selectively permeable to sodium and only allows a small amount of sodium to enter the cell by passive diffusion, the majority of sodium that moves across the cell membrane does so in a regulated fashion through specialized transporters.

The accumulation of sodium intracellularly must be counteracted to maintain normal cellular homeostasis. For most tissues the Na^+/K^+-ATPase pump also known as the sodium-potassium pump is the dominant contributor to the removal of intracellular sodium and the maintenance of a steady-state intracellular sodium concentration (49). The sodium-potassium pump uses the hydrolysis ATP into ADP and inorganic phosphate (Pi) to provide the energy to drive 3 Na^+ ions out of the cell in exchange for every 2 K^+ ions that it brings into the cell. The sodium pump is extremely energy intensive as it must overcome the powerful intracellular driving forces acting on the sodium ions. This leads to the sodium-potassium pump's consuming of a large proportion of the energy available to tissue. Under normal circumstances the sodium-potassium pump activity is not limited by ATP availability but in anoxic conditions tissue ATP levels have been shown to be insufficient for the pump to function (50) and both the ion transport and hydrolytic activity of the sodium-potassium pump are suppressed when in hypoxic and hyperoxic states (51, 52). The sodium-potassium pump is therefore more oxygen sensitive than it is responsive to ATP concentration.

Cancer tissue is often hypoxic and energy resources are also diverted away from healthy physiological processes and towards growth, replication and expansion. The rate of

metabolism of glucose via pathways like oxidative phosphorylation which produce the maximum yield of ATP is reduced in cancer and glucose use is instead shifted towards other processes like the manufacture of nucleotides, lipids and amino acids (53, 54) needed for growth. The incomplete breakdown and trapping of glucose as other molecules within cancers has been demonstrated previously on ^{18}F-fluorodeoxyglucose positron emission tomography (^{18}F-FDG-PET) imaging (55, 56).

The growth of cancer fuelled by these metabolic changes may be so rapid that it can eventually outstrip the tumour's blood supply leading to poor perfusion and worsening hypoxia. Over time tumours can become oxygen and energy deficient to the point where necrosis occurs (57). VEGF (vascular endothelial growth factor) activity is usually increased in tumours that are hypoxic to help compensate for the reduced blood supply by stimulating blood vessel growth. The presence of VEGF is a poor prognostic marker in certain cancers (58-60). VEGF additionally contributes to blood vessel porosity and tissue oedema (61) which increases the relative amount of high sodium concentration extracellular fluid and therefore overall tissue sodium concentration even further.

In hypoxic tissue, the sodium-potassium pump activity decreases permitting the accumulation of sodium intracellularly. This sodium draws water with it by osmosis and contributes to cell swelling (62, 63). The accumulation of sodium intracellularly is one of the precursors to cell death (64) and measurement of intracellular sodium may therefore serve as an early biomarker for both hypoxia induced necrosis and cell death in response to treatments like chemotherapy.

The effect of cancer formation on the intracellular sodium concentration may be more pronounced in the areas of a tumour with the most hypoxia and the poorest perfusion. If this is the case, it would mean that quantification of the intracellular sodium concentration in cancer could provide information on the extent of the shift of a cancerous tissue towards growth and expansion and therefore relate to the aggressiveness of the tumour.

Apart from metabolism, changes to the integrity of the cell membrane and changes in cellularity with cancer formation may also affect the distribution of sodium. Porous or completely degenerated membranes in dying or necrotic cells increase the freedom of movement of sodium between the intracellular and extracellular compartments and may

lead to equilibration of concentrations. Changes in the ratio of intracellular to extracellular space also occur with the denser cell packing of tumours and with the accumulation of extracellular fluid from cancer induced inflammation and oedema.

The sodium nucleus is magnetic resonance active and endogenous nuclei can be imaged with MRI by applying radiofrequency radiation of the wavelength at which sodium resonates. This requires special transmit and receive hardware that can produce the appropriate RF pulse and detect the sodium MRI signal. For sodium MRI, the scanner being used must also be capable of multi-nuclear imaging. Multi-nuclear scanners and sodium transmit and receive coils are available commercially. In Chapter 4 of this PhD results from sodium imaging in ovarian cancer patients are presented.

2.14 Magnetization transfer imaging in cancer

Water molecules in biological systems can exist either as free molecules or bound to macromolecules like proteins and lipids. Bound water is also known as structured water and can form hydration layers of restricted water motion that extend around surfaces like cell membranes for several molecular diameters (65). The macromolecules to which bound water attaches cause a broadening in the range of frequencies at which water can absorb magnetization, whereas free water only responds over a much narrower range of magnetization frequencies.

In magnetization transfer (MT) imaging an “off-resonant” radiofrequency (RF) pulse is used to preferentially saturate bound water. Some of this saturation is transferred to the free water molecule pool either through magnetic coupling between free and bound water molecules or by direct molecular exchange (66). A magnetization transfer ratio (MTR) can then be derived that provides information on the macromolecules present in a tissue. MT imaging uses the large visible free water pool to report on the much smaller bound water pool and consequently, MT delivers an alternative form of contrast to T_1, T_2, and proton density weighted imaging. MT imaging reflects the degree to which saturation exchange occurs between the free and bound states which is a form of spin-lattice relaxation (67).

In cancer, there is remodelling of extracellular matrix macromolecules. MT imaging in cancer may provide information on these changes. Changes in tumour stroma relate to

invasiveness and prognosis and imaging of the matrix of cancers may thus have important implications for treatments and outcomes in oncology.

For some solid tumours such as prostate cancer, MTR has been found to be higher in cancer compared to normal tissue (68). In other tumours such as glioma, MTR decreases compared to normal brain, as the central nervous tissue macromolecular myelin concentration drops in several cerebral disease processes including cancer (69). In breast cancer both increases and decreases in MTR relative to benign tissue have been found which may relate to differences in the extracellular macromolecular tissue (70, 71) and in hepatic malignancies an MTR similar to that of normal liver has been noted in one study (72). Recently a small number of studies have also found use for magnetization transfer imaging in assessing the response of some cancers to therapy (73, 74).

Despite its extensive use in previous studies, the specific macromolecules responsible for changes in MTR with malignancy have never been identified. The high cellular proliferation of cancers may contribute to an increase in macromolecule content but the destruction of the surrounding tissue by cancer may simultaneously lead to a decrease in available water binding sites. The comparison of MTR with tissue macromolecule measurements could therefore provide valuable information on the tumour microenvironment that has not yet been identified. The relationship of tumour macromolecules to MT imaging is compared with ovarian cancer in Chapter 6 of this dissertation.

2.15 Hyperpolarized carbon-13 MRI

Hyperpolarized carbon-13 MRI (HP ^{13}C-MRI) is a new imaging technique that can provide unique metabolic information about cancer. HP ^{13}C-MRI involves the use of molecules labelled with ^{13}C that have undergone an alignment of their nuclear spins that significantly increases the MRI signal that can be detected: this allows an injected molecule and its biochemical reactions in tissue to be imaged *in vivo* to provide real time information on the metabolism of tissue and the activity of enzymes in the tumour environment (75).

Clinical HP ^{13}C-MRI is currently restricted to the imaging of hyperpolarized ^{13}C labelled pyruvate metabolism. This is due to the favourable physical and chemical properties of

pyruvate for hyperpolarization and the fact that pyruvate is central to a number of important cellular biochemical reactions in normal tissue and in tumours.

The term hyperpolarization refers to an array of techniques that increase the proportion of nuclei aligned with the main MR magnetic field. Historically, a variety of methods have been used to increase polarization for metabolic imaging. One of these is dynamic nuclear polarization (DNP). DNP involves the cooling of the carbon-13 labelled molecule close to absolute zero (~1 K) in magnetic field (3.35-5 T) which causes electrons to be almost fully polarized. The sample is then irradiated with microwave radiation to transfer the polarization from surrounding electrons to the carbon-13 nuclei. In 2003 a breakthrough occurred using this method when it was demonstrated that it could increase the MR signal-to-noise ratio of carbon-13 by more than 10,000-fold and the frozen sample could subsequently be dissoluted into the liquid form and warmed so that it could be injected into biological systems while maintaining polarization levels with a half-life of around 60 s *in vitro* (76). These discoveries have now led to the possibility of using molecules labelled with carbon-13 to quantify and image tumour metabolism *in vivo* in unprecedented detail.

For clinical hyperpolarized carbon-13 (HP C-13) imaging a special setup is required where the MRI scanner and hyperpolarizer are in separate rooms to minimize interference between their magnetic fields. After dissolution in the hyperpolarizer, the hyperpolarized sample must undergo quality control (QC) checks to ensure it is safe for injection into a human. This is done by spectrophotometry to measure parameters such as concentration and pH. After the QC check, the sample is rapidly moved into the room with the MRI scanner and loaded into a syringe pump to be injected into the patient. Like with sodium imaging, a dedicated coil sensitive to carbon-13 is required to detect the signal and the scanner must have multi-nuclear capabilities. Due to the low signal strength even after hyperpolarization, a 3T or more powerful field strength scanner is required to produce images of sufficient signal-to-noise ratio to create meaningful images. The rapid decay of the C-13 signal also requires that a fast acquisition pulse sequence is used to perform imaging before the majority of the signal disappears. This is explained further in Chapter 7 and a case report of a benign ovarian tumour is presented in Chapter 9.

2.16 ^{18}F-FDG-PET imaging

^{18}F-fluorodeoxyglucose positron emission tomography (^{18}F-FDG-PET) utilises 2-deoxy-2-(^{18}F)fluoro-D-glucose, also called ^{18}F-fluorodeoxyglucose (^{18}F-FDG) to image tissue metabolism. ^{18}F-FDG is an analogue of glucose that is taken up by cells where it is trapped in the intracellular space following phosphorylation by the enzyme hexokinase as ^{18}F-FDG-6-phosphate, which cannot be metabolised further by glycolysis due to the lack of a 2-hydroxyl group. Fluorine-18 (^{18}F) undergoes radioactive decay with a half-life of around 110 minutes mostly by positron emission but also by electron capture to produce oxygen-18 (^{18}O). ^{18}F decay by positron emission follows the reaction below:

$$^{18}F \longrightarrow {}^{18}O + e^{+} + \nu_e \qquad (2.2)$$

where e+ represents the positron – the positively charged anti-particle of an electron - and ν_e denotes the neutrino emitted during decay. The conversion of fluorine-18 into oxygen-18 generates the 2-hydroxyl group needed for glycolysis and allows the tracer to be metabolised in a manner similar to glucose.

Positron emission decay is also known as positive beta (β+) decay. The positron emitted on β+ decay travels through tissue until it encounters an electron (e^-) at which point both the positron and the electron undergo annihilation, producing two equivalent photons of approximately 511 keV energy that move in approximately opposite directions. The annihilation photons are detected by an array of scintillator detectors located on the scanner and the positions and times at which these are detected is used to identify the point of origin of the annihilation event. Tissues exhibiting higher ^{18}F-FDG transport and higher rates of ^{18}F-FDG phosphorylation by hexokinase display increased ^{18}F-FDG-PET signal. PET can provide a direct measurement of ^{18}F-FDG radioactivity concentration (Bq/mL) i*n vivo*, nevertheless it is the relative tissue uptake of ^{18}F-FDG that is utilised in clinical practice to facilitate comparisons between patients. The two most significant sources of variation that occur in ^{18}F-FDG uptake in patients are due to the amount of injected ^{18}F-FDG activity and the patient's size. To account for these the standardized uptake value (SUV) is used

clinically to provide a measure of the relative uptake of ^{18}F-FDG in tissues (77). The SUV of an area in an image is the ratio of the concentration of radioactivity in this area divided by the radioactivity injected into the patient normalised by body weight. Expressed as an equation:

$$\mathrm{SUV} = \frac{\text{Radioactivity concentration in region of interest (Bq/mL)}}{\text{Injected activity (Bq)} \;/\; \text{Body weight (g)}} \qquad (2.3)$$

SUV_{max} is the maximum SUV voxel value within a region of interest and is a routine clinical tool for interpreting PET images. Other metrics like SUL (Standardized Uptake normalised to lean body mass) may offer more accurate estimates of uptake but are not yet as widely used as SUV, reference data for the interpretation of SUL values are therefore not as readily available as SUV making SUV a more accessible and recognizable tool for scientific research and the implementation of findings among clinicians. The measured SUV on imaging is affected by serum glucose concentration, GLUT transporter expression, liver metabolism, blood flow, renal excretion of ^{18}F-FDG and the time point of imaging. To help address the time-point dependence and inaccurate normalisations of tracer availability with SUV, kinetic modelling approaches can be used on dynamic ^{18}F-FDG data (78).

SUV_{max} is higher in cancerous tissue because of an increase in metabolic activity, GLUT expression and greater activity of mitochondrial hexokinase enzyme. ^{18}F-FDG -PET in ovarian cancer is sometimes used clinically when lesions are difficult to evaluate on other types of imaging or when there is a need to detect metastatic disease for staging (79). SUV_{max} has also been used in the context of clinical trials for treatment response monitoring and the detection of ovarian cancer recurrence (80, 81). In this PhD, FDG-PET is used as a comparison with HP ^{13}C-MRI with the findings detailed in Chapter 9.

2.17 Magnetic resonance fingerprinting

Magnetic resonance fingerprinting (MRF) is an acquisition technique than can rapidly produce quantitative maps of multiple magnetic resonance parameters. Quantitative maps

of MRI parameters have higher repeatability and reproducibility than weighted images and their use could improve data comparisons across different centres and scanners and therefore improve diagnostic reader consistency. The T_1, T_2 and proton density maps of MRF can also be used to construct images of multiple weightings after the imaging session and provide varied forms of tissue contrast for diagnostic use without occupying the MRI scanners of a hospital radiology department.

Conventional acquisitions of T_1, T_2 and proton density maps are time consuming and impractical in routine clinical practice. MRF can generate quantitative parameter maps in shorter scan times using ultra-short TE (UTE) techniques (9) and only one signal acquisition which also makes MRF relatively insensitive to motion.

MRF uses a pseudorandom simulation of flip angle, repetition time (TR) and other imaging parameters to create a signal evolution pattern or “fingerprint” in each voxel that depends on the tissue types in that voxel and the intrinsic MR properties of those tissues such as the T_1, T_2 and proton density. The MR signal pattern that is detected can then be mapped to a dictionary to output synthetic maps of the MR parameters and to produce weighted images.

The first published data on MRF in ovarian cancer was acquired a part of this PhD with MISSION-ovary patients and is described in Chapter 10.

Chapter 3

Diffusion kurtosis imaging in ovarian cancer

3.1 Background

The best outcomes in high grade serous ovarian cancer (HGSOC) occur when treatment is with a combination of surgery and chemotherapy (82). The initiation of chemotherapy in ovarian cancer patients however usually requires a definite diagnosis of the epithelial subtype as chemotherapy is associated with significant side effects and its use would not be justified in cases of less malignant ovarian lesions.

Currently, there is no imaging or serum biomarker test that can reliably separate HGSOC from other ovarian cancers in patients who present with a suspicious pelvic mass. Diagnosis of HGSOC therefore relies on biopsy sampling and histopathological analysis of tissue including immunohistochemistry. Unfortunately, in some patients, the ovarian cancer presents in an anatomical location that is not amenable to any form of image guided percutaneous needle biopsy, either because the cancer deposits are too deep within the abdomen and pelvis or are in close proximity to high risk structures that could be damaged by the trauma of biopsy. Patients with these problems are often sent for a surgical procedure to extract diagnostic tissue samples which in some cases can include removal of additional organs like the uterus, omentum, fallopian tubes and ovaries to avoid the need for future operations.

Biopsy whether performed percutaneously or by an open procedure is invasive and carries with it risks of discomfort, bruising, bleeding, and infection. Needle biopsy samples may also extract inadequate amounts of tissue or sample the incorrect area, sometimes missing the cancerous lesion entirely. Even more concerning is the fact that biopsies do not represent the whole ovarian lesion as each sample is taken from only one point. In the most malignant tumours like HGSOC, tissue heterogeneity is a prominent feature meaning that different

areas of the tumour have a distinct biochemical, histological and genetic composition (83, 84). As a consequence, biopsy with histology although considered the gold-standard diagnostic test can still misclassify ovarian lesions and lead to incorrect or suboptimal treatment of HGSOC.

The first line chemotherapy choice for HGSOC is a platinum-based drug together with a taxane (85), both of which inhibit cell division. This combination however, has a complete remission rate of only around 50% (85, 86). Newer targeted therapies based around DNA damage repair inhibition (87, 88), vascular growth factor inhibition (88) and immune checkpoint inhibition (89) are now being developed that may provide alternative treatment options to HGSOC patients in the future. With the availability of new therapies, there is an increasing need for methods to both predict and detect the response to treatment in HGSOC at the earliest timepoints possible, so that the best personalized therapies can be selected for individual patients.

Diffusion weighted imaging (DWI) is a reproducible imaging method (90, 91) that uses Gaussian modelling and has previously been shown to identify early treatment response in HGSOC by reporting on the cytotoxic effect of platinum-based chemotherapy (92). This study evaluated an extended version of diffusion modelling in MRI, diffusion kurtosis imaging (DKI), as a predictor of response before the initiation of treatment.

The Gaussian or mono-exponential model of diffusion assumes that the main obstructions to diffusion are evenly distributed and restrict diffusion uniformly. In tissue it is the cells, organelles within cells, extracellular matrix structures and fibers such a myelin sheets in brain that are the main obstacles to diffusion. The complexity of microstructure and the complexity of the distribution of cells increases in cancer compared to healthy tissue and imparts a positive kurtosis to the Gaussian pattern of diffusion. High heterogeneity in the composition and spatial distribution of cancer cells means that the ADC maps currently used for clinical practice may inaccurately represent the diffusion of water molecules for cancers.

To create quantitative maps, DKI employs a bi-exponential model that makes use of the second term in the Taylor series expansion of the DWI signal to fit each voxel in an image (93). The additional exponential term relates to the kurtosis caused by the tissue to the diffusion signal. With imaging of higher diffusion weighting, the kurtosis effect on diffusion

becomes more apparent. DKI therefore requires the inclusion of DWI images of high b-value (94). DKI produces maps of two parameters, D_{app} (apparent diffusion) and K_{app} (apparent kurtosis). In DKI, the diffusion weighted images are fit to Equation (3.1) below.

$$S(b) = S_0 \cdot \exp\left(-b \cdot D_{app} + 1/6 \cdot b^2 \cdot D_{app}^2 \cdot K_{app}\right) \quad (3.1)$$

The nuclear protein Ki-67 is a marker of proliferation and tissue heterogeneity and has displayed a correlation with DKI in several malignancies, including ovarian cancer (95-97). Although Ki-67 is a marker of proliferation it may also serve as a marker of tissue heterogeneity as more proliferative tissues are likely to also be more heterogenous. Ki-67 has also been shown to identify cancers that are sensitive to chemotherapeutic agents that target proliferating cells (98, 99). These previous findings support the hypothesis that DKI could predict the response of HGSOC to chemotherapy agents that function by inhibiting cell division and there is already some evidence to support this in nasopharyngeal cancer (100). The work here assesses the ability of DKI to predict the response of HGSOC in patients undergoing three cycles of standard of care neoadjuvant chemotherapy (NACT) treatment for the first time. Results from this chapter have been published in the journal *Scientific Reports* (101).

3.2 Methods

Ethical approval for this study was obtained from a local Research Ethics Committee (South Cambridge REC) as part of the MISSION-ovary study and all study related procedures were performed with the written informed consent of participants. This study was carried out in accordance with the research ethics guidelines outlined in the 1965 Declaration of Helsinki.

Imaging

A 3T MRI scanner (Discovery MR750, GE Healthcare, Waukesha WI) and a 32-channel cardiac array coil were used to perform DWI and T_2-weighted imaging on participants

between one and seven days (median four days) before the start of chemotherapy treatment. A spectro-spatial excitation pulse was used to produce water selective excitation and 20mg of intravenous hyoscine butylbromide was given prior to imaging to reduce bowel motion. Full scan parameters are listed in Table 3.1.

Table of DKI study imaging parameters

Imaging parameter	**T_2-weighted**	**Diffusion weighted imaging**
TR	4000 ms	6000 ms
TE	91.1 ms	94 ms
flip angle	90°	90°
slice thickness	6 mm	6 mm
FoV	34.0 cm × 29.9 cm	34.0 cm × 29.9 cm
matrix	256 x 256	128 × 112
signal averages	8	4
parallel imaging	-	ASSET, factor 2
bandwidth	99.8 kHz	± 142 kHz
total scan time	1 min 54 sec	7 min 42 s
b-values	-	100, 500, 900, 1300 and 1700 s/mm^2

Table 3.1: T_2-weighted and diffusion imaging parameters. TR = repetition time, TE = echo time, FoV = field of view.

Apparent diffusion (D_{app}), in mm^2/s and apparent kurtosis (K_{app}), unitless maps were generated by Dr Andrew Priest from the Cambridge Department of Radiology with in-house software written in MATLAB R2018a (The MathWorks Inc., Natick, MA), by performing a pixel-wise non-linear fit to the bi-exponential diffusion kurtosis model described in equation 3.1. Apparent diffusion coefficient (ADC) values, in mm^2/s were also calculated with MATLAB using conventional mono-exponential Gaussian diffusion modelling from the images with b-values of 100, 500 and 900 s/mm^2. Regions of interest (ROIs) were drawn on

the D_{app} maps with OsiriX (version 3.8.1, Pixmeo, Geneva, Switzerland) around all solid cancerous lesion with care taken to exclude cystic and necrotic regions. ROIs were imported onto the ADC and K_{app} maps, which were assumed to be co-registered as they were derived from the same set of DWI images. ROIs were reviewed by a radiologist, with 8 years of attending experience in oncological imaging and who was kept blind to treatment response and tissue analysis results. For each patient all tumour ROIs present in the abdomen and pelvis were combined into a single volume of interest (VOI). Intraobserver and interobserver variability were also assessed with a second set of ROIs drawn by myself.

Response evaluation

Response to NACT was assessed according to Response Evaluation Criteria In Solid Tumours (RECIST) criteria version 1.1 (102), using contrast enhanced CT scans. These were a baseline CT scan before the initiation of chemotherapy and a second CT scan up to one week after the third cycle of chemotherapy. The team of attending gynaecologic radiologists performing evaluations of response were blinded to MRI and tissue analysis results. Participants with 30% or greater reduction in disease, i.e. a RECIST Complete Response (CR) or Partial Response (PR) were classified as responders and those with Stable Disease (SD) or Progressive Disease (PD) were classified as non-responders.

Tissue handling and immunohistochemistry

Tumor samples were collected before treatment either by ultrasound-guided needle biopsy or a surgical procedure in the cases of lesions that were not accessible through the percutaneous route. Tissue was fixed in formalin and embedded into paraffin blocks. 3µm sections were cut from the blocks and stained with H&E (haematoxylin and eosin) and Ki-67 (Dako Cat# M7240, Research Resource Identifier (RRID) AB_2142367). Staining was carried out using Leica's Polymer Refine Detection System (DS9800) automated Bond platform. This platform included a primary rabbit anti-mouse IgG (<10 µg/mL) in 10% (v/v) animal serum plus tris-buffered saline/0.09% (ProClin™ 950) and a polymer of anti-rabbit poly-HRP-IgG (<25 µg/mL) in 10% (v/v) animal serum plus tris-buffered saline/0.09% (ProClin™ 950).

Bright-field scanning was performed on an Aperio AT2 scanner (Leica) to digitize slides for automated analysis. Quantification of Ki-67 staining and of the number of cells per unit area, as an estimate of cellularity (cells/μm^2), were performed using the multiplex IHC V1.2 module of Halo histology image analysis software (Indica labs v2.1.1637.11). Cells with Ki-67 staining greater than an optical density of 0.31 were considered positive. The operator of the analytic software was blinded to MRI and treatment response results.

Statistical methods

All statistical analysis was performed in R (version 2.15.3, R Foundation for Statistical Computing, Vienna, Austria) and a *P* value of 0.05 was used as the cut-off to indicate significance.

Intraobserver and interobserver agreement were assessed using the intraclass correlation coefficient (ICC). When testing for differences in means between groups, the Shapiro–Wilk test was used to assess for normality of data. Student's t-test or the Mann-Whitney *U* test was then applied for evaluations on normally and non-normally distributed data respectively. Immunohistochemistry results were compared to diffusion parameters using Spearman's correlation.

3.3 Results

Study population

Seventeen patients were successfully recruited to this study. Mean age, 66.6 ± 9.4 (mean ± S.D.) and range, 43 to 81 years old. Population demographics are summarized in Table 3.2. After MRI imaging, 15 of the 17 participants went on to have NACT treatment with a combination of carboplatin and paclitaxel. The remaining 2 patients were treated with primary surgery and adjuvant chemotherapy. The tumours included ranged in size from 33.8 ml to 699.9 ml and the mean tumour size was 142.9 ml.

Feature	Value
Number of patients	17
Age at diagnosis, mean (range) (years)	66.6 (43 to 81)
ECOG performance status (number of patients)	
0-2	13
3-4	4
FIGO stage (number of patients)	
I	0
II	1
III	12
IV	4
Serum CA 125 at diagnosis (IU/ml) (number of patients)	
0-100	4
100-500	5
>500	8
Volume of ROIs analysed (number of patients)	
0 to 25 ml	0
>25 to 50 ml	3
>50 to 100 ml	8
>100 ml	6
Treatment pathway	
Neoadjuvant treatment	15
Adjuvant treatment	2
RECIST response on CT	
Complete response (CR)	0
Partial response (PR)	5
Stable disease (SD)	8
Progressive disease (PD)	2

Table 3.2: Population demographics of patients recruited. ECOG = Eastern Cooperative Oncology Group, FIGO = Fédération Internationale de Gynécologie et d'Obstétrique, ROI = region of interest, RECIST = Response Evaluation Criteria In Solid Tumors, CA 125 = cancer antigen 125, NACT = neoadjuvant chemotherapy, S.D. = standard deviation.

Imaging

There was a good fit of DWI images to the DKI model for the volumes of interest (VOIs) analyzed. Fig. 3.1 shows an example of a typical DWI image and the diffusion parameter maps for a 63-year old HGSOC patient who responded well to NACT. For comparison, Fig. 3.2 displays a DWI image and the diffusion parameter maps of a 76-year old patient who was classified as a non-responder. The CT scans before and after therapy for both patients are also shown.

Intraobserver and interobserver variability

There was good intraobserver and interobserver agreement for all diffusion metrics measured. Results are summarized in Table 3.3.

Diffusion metric	Intraobserver ICC	Interobserver ICC
ADC	0.971 (0.967 to 0.972)	0.977 (0.975 to 0.978)
D_{app}	0.968 (0.965 to 0.971)	0.974 (0.971 to 0.976)
K_{app}	0.989 (0.986 to 0.981)	0.989 (0.986 to 0.982)

Table 3.3: Intraobserver and interobserver variability for diffusion imaging metrics. ICC = intraclass coefficient correlation, ADC = apparent diffusion coefficient, D_{app} = apparent diffusion, K_{app} = apparent kurtosis. Values in brackets represent the 95% confidence interval.

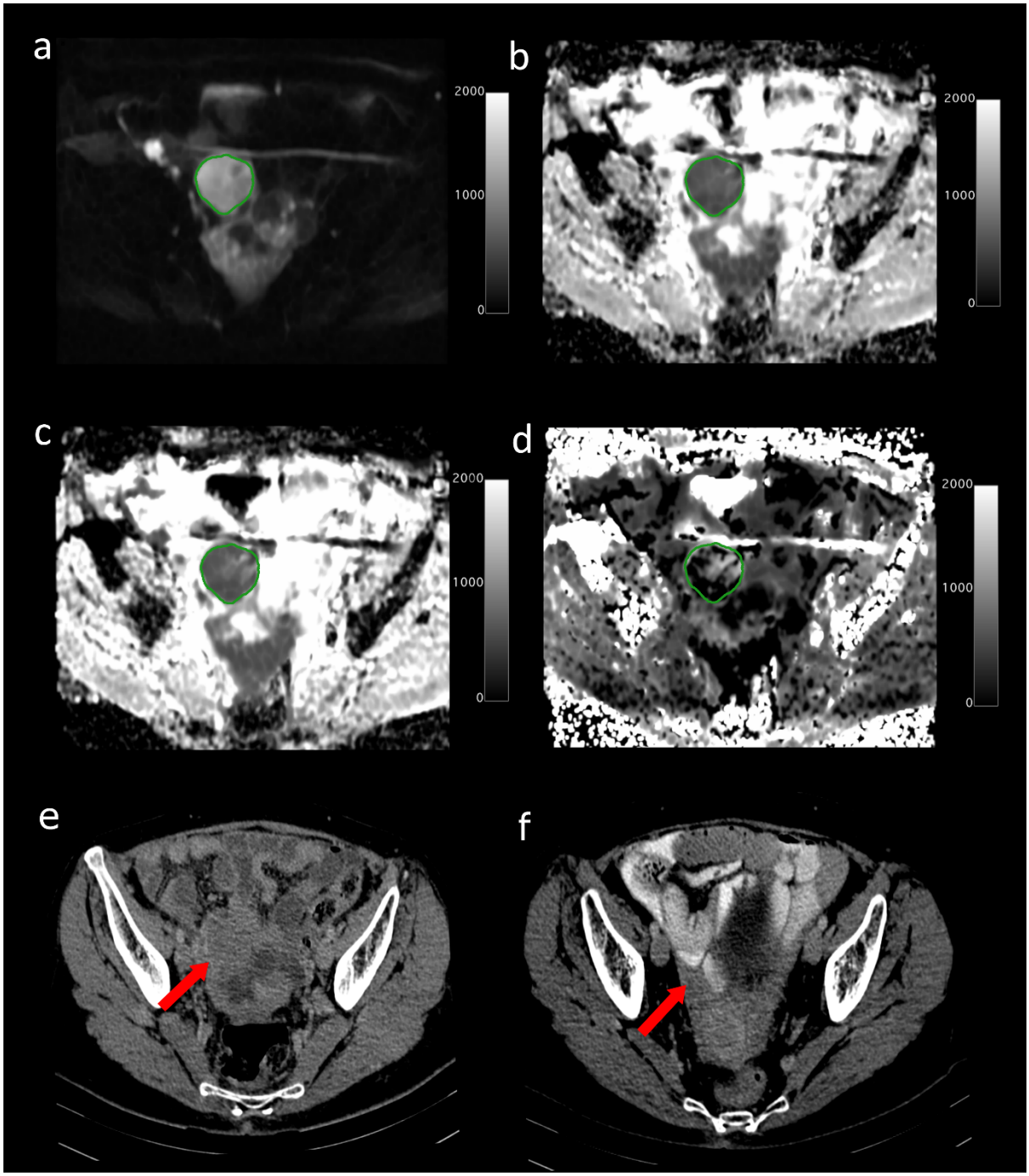

Figure 3.1: Axial MRI images from a 63-year old high grade serous ovarian cancer patient who had a good response to neo-adjuvant chemotherapy. Images (a) to (e) were taken before treatment and (f) was taken after 3 cycles of chemotherapy. (a) DWI at b=1300 s/mm^2. Scale bar represents signal intensity; (b) ADC map with tumour ROI shown. Scale bar represents ADC x 1000 in s/mm^2; (c) D_{app} map. Scale bar represents D_{app} x 1000; (d) K_{app} map. Scale bar represents K_{app} x 1000; Axial CT scans following intravenous contrast medium (e) before treatment; (f) after treatment, depicting a RECIST Partial Response (PR).

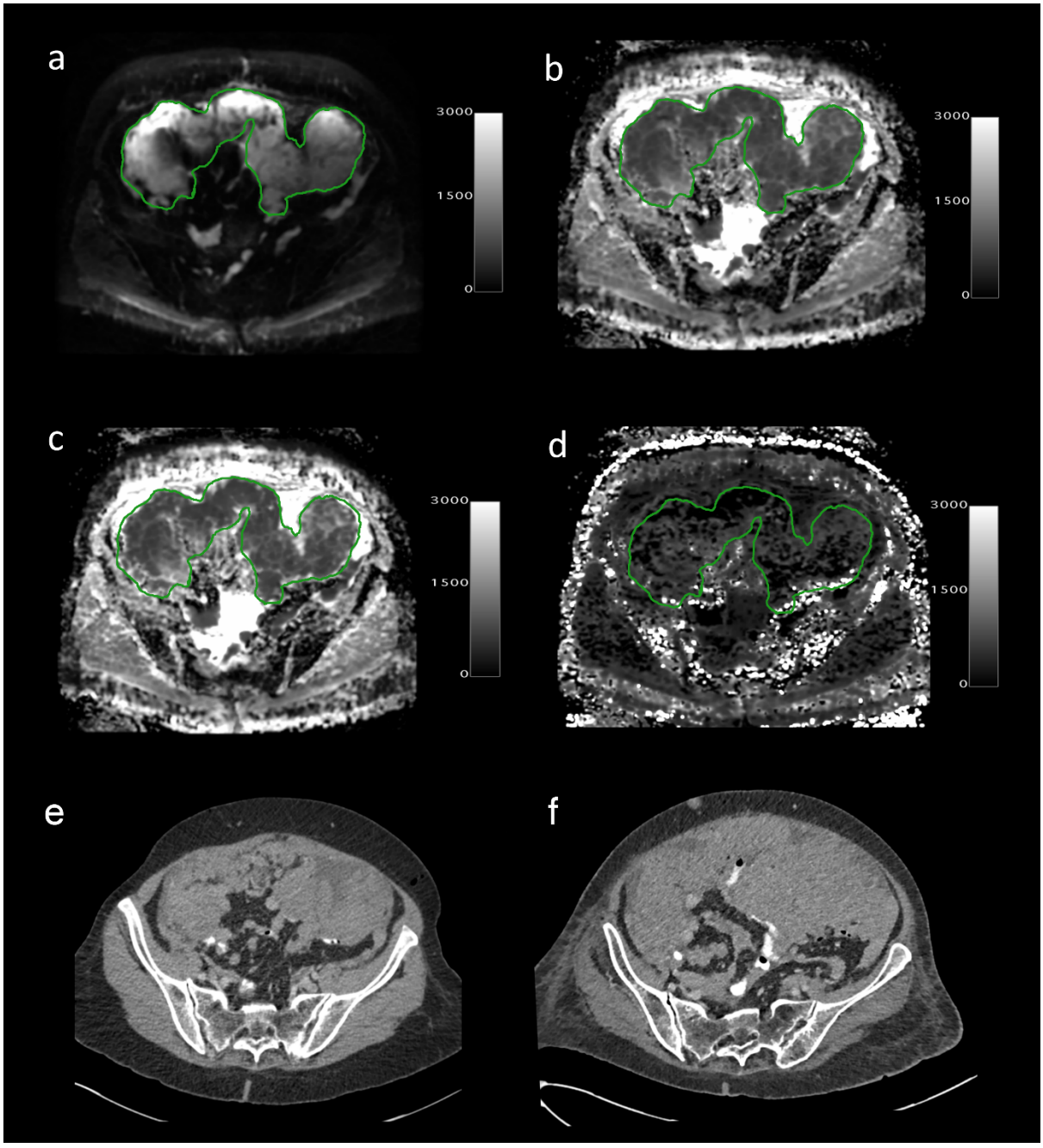

Figure 3.2: Axial MRI images from a 76-year old high grade serous ovarian cancer patient who did not respond well to neo-adjuvant chemotherapy. Images (a) to (e) were taken before treatment and (f) was taken after 3 cycles of chemotherapy. (a) DWI at b=1300 s/mm^2. Scale bar represents signal intensity; (b) ADC map with tumour ROI shown. Scale bar represents D_{app} x 1000; (c) D_{app} map. Scale bar represents D_{app} x 1000; (d) K_{app} map. Scale bar represents K_{app} x 1000; Axial CT scans following intravenous contrast medium (e) before treatment; (f) after treatment, depicting RECIST Progressive Disease (PD).

Predicting treatment response

Of the 15 patients to undergo NACT, there were 10 responders and 5 non-responders. A significant difference was found in the pre-treatment mean K_{app} between the responders and non-responders: 0.69 ± 0.13 versus 0.51 ± 0.11 (mean $\pm$ S.D.) respectively; Mann-Whitney *U* test, *P* = 0.02 for a difference between these two groups. D_{app} was not found to be significantly different between responders and non-responders: 1.44 ± 0.30 versus $1.51 \pm 0.32 \times 10^{-3}$ mm^2/s respectively; *P* = 0.68 and the difference in ADC between the groups was similarly non-significant: $1.22 \pm 0.24 \times 10^{-3}$ mm^2/s versus $1.30 \pm 0.27 \times 10^{-3}$ mm^2/s respectively, *P* = 0.77. Boxplots of the median ADC, D_{app} and K_{app} values for the responders and non-responders are shown in Fig. 3.3.

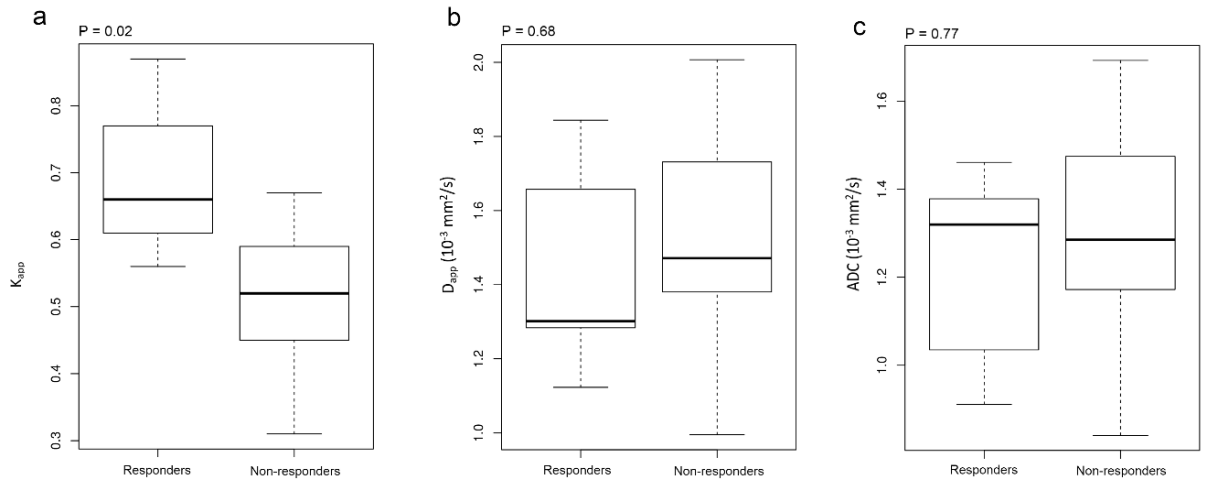

Figure 3.3: Box plots showing median and inter-quartile ranges of diffusion parameters for responders and non-responders to neoadjuvant chemotherapy. (a) ADC; (b) D_{app}; (c) K_{app}.

Correlation with cellularity and Ki-67 expression

Localization of the Ki-67 stain in all cases was to the nucleus of cells, where the Ki-67 protein is expected to be found (103). Ki-67 staining was also subjectively observed to be greater in tissue that was confirmed as cancerous on H&E, which is consistent with the expression pattern of this protein that is known to be upregulated in ovarian cancer (104).

Figure 3.4 shows the typical appearances of the H&E and Ki-67 staining for a responder (Figure 3.4 a) and a non-responder (Figure 3.4 b) to therapy. An example of the automated segmentation of Ki-67 positive cells in Halo, is shown in Figure 3.4 c, illustrating the accuracy of the cell classification by the software.

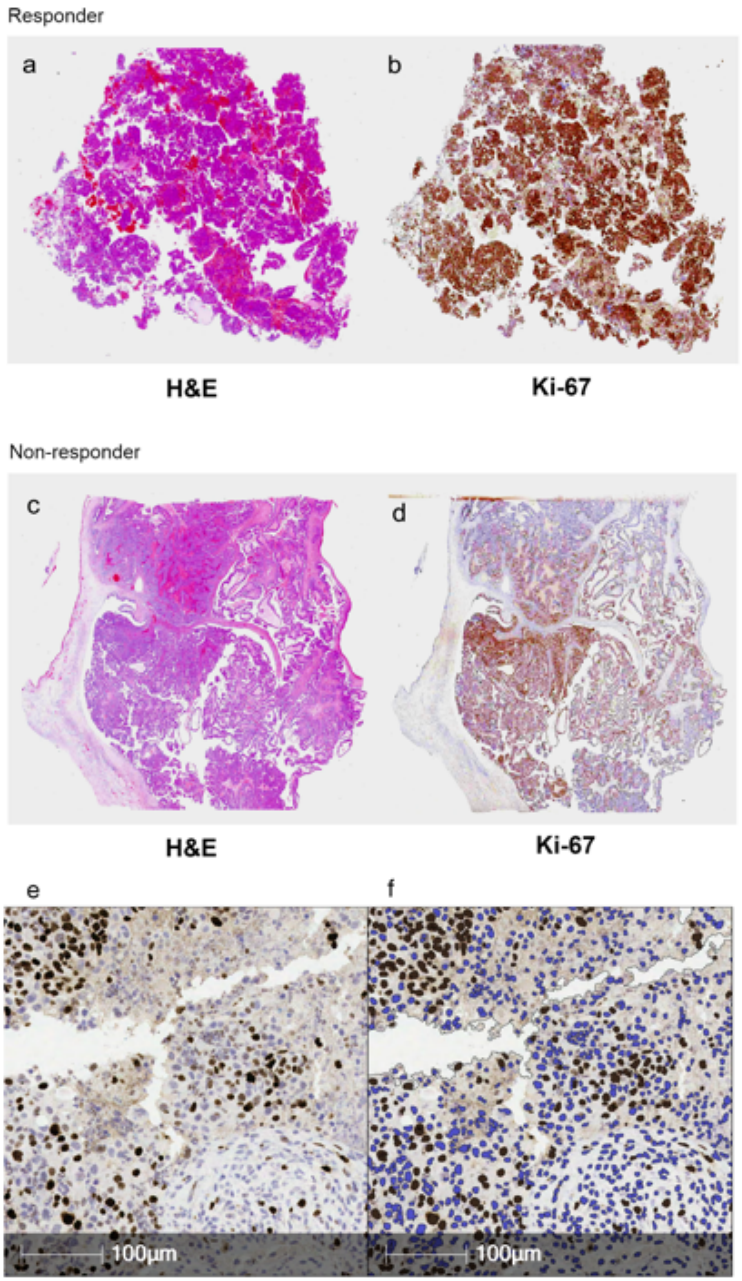

Figure 3.4: Examples of histology from two patients with HGSOC: a responder and a non-responder. (a) 1x magnification H&E slide of a patient who subsequently responded well to chemotherapy; (b) 1x magnification Ki-67 staining from the same patient (positive tissue shown in brown and negative tissue shown in blue); (c) 1x magnification H&E slide from a patient who subsequently did not respond well to chemotherapy ; (d) 1x magnification Ki-67 staining from the same patient (positive tissue shown in brown and negative tissue shown in blue); (e) 20x magnification of Ki-67 staining in a HGSOC patient, with positive cells in dark brown and background counter staining in blue; (f) automated image segmentation in Halo for quantification of Ki-67 staining. Positive cells colored dark brown by software and negative cells colored blue by software.

Cellularity exhibited a positive correlation with K_{app}, (Spearman rho (r_s) = 0.49, *P* = 0.04) and negative correlations with both ADC (r_s = -0.77, *P* = 0.02) and D_{app} (r_s = -0.73, *P* = 0.03). K_{app} correlated positively with the percentage of cells expressing Ki-67 (r_s = 0.53, *P* = 0.03), but ADC and D_{app} did not correlate with Ki-67, *P* = 0.55 and *P* = 0.15 respectively. A scatterplot of mean tumor K_{app} against Ki-67 quantification is shown in Figure 3.5.

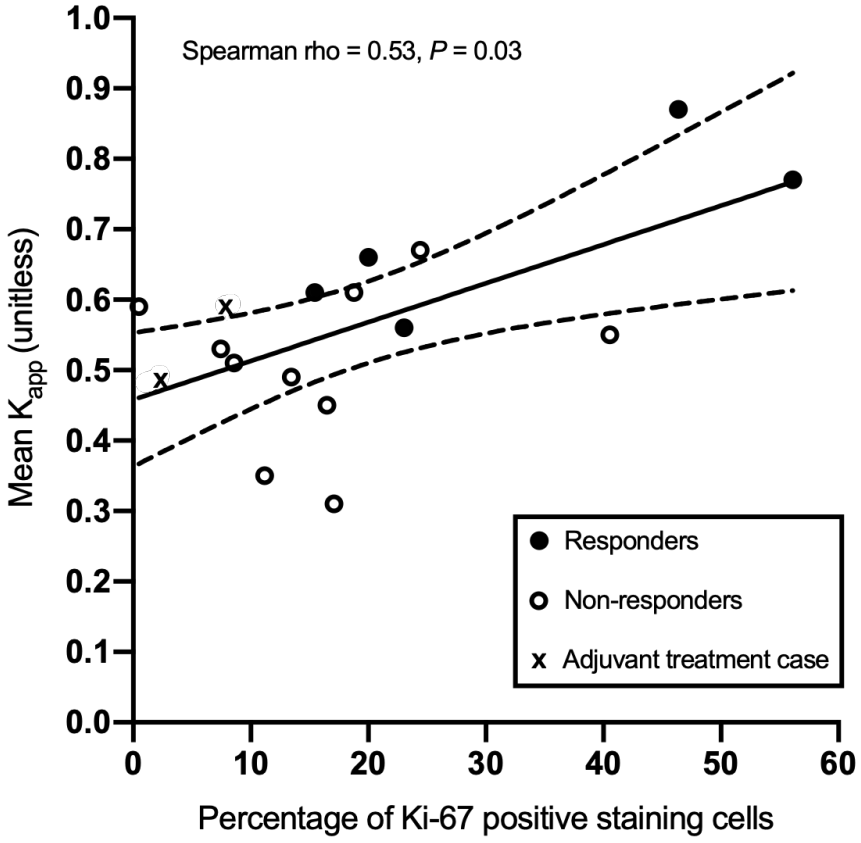

Figure 3.5: scatterplot of mean tissue K_{app} against percentage of cells positive for Ki-67 staining (optical density >31). White circles indicate responders to neo-adjuvant chemotherapy, black circles indicate non-responders and crosses indicate the two patients treated with primary surgery before starting adjuvant chemotherapy.

3.4 Discussion

This study demonstrated a significant difference in the value of the DKI metric, K_{app} before treatment in responders and non-responders to neo-adjuvant chemotherapy in HGSOC. This suggests that it may be possible for K_{app} to predict the response to neoadjuvant chemotherapy in treatment naïve HGSOC patients. Tumours with a higher mean K_{app} before the start of chemotherapy were found to respond better to treatment whereas, neither ADC nor D_{app} could differentiate future responders from non-responders. All three diffusion metrics correlated with cellularity, which was an expected finding as cells form the major barrier to the diffusion of water in tissue (105-107). Immunohistochemistry results also confirmed that the previously reported relationship between K_{app} and Ki-67 also apply to the patient cohort recruited here (95, 96).

The magnitude of the K_{app} term in DKI reflects the degree of kurtosis applied to the Gaussian diffusion model by the tissue structure and consequently relates to tissue heterogeneity (108). Heterogeneity in turn is used to help determine tumour grade on histopathology. In some tumours, DKI may therefore be of diagnostic value for grading. Studies have already demonstrated that DKI can differentiate grade II and III gliomas (97, 109) as well low grade and high grade prostate cancer (110, 111) and borderline from malignant epithelial ovarian tumours. However, in the case of ovarian cancer, K_{app} has not been shown to be superior to conventional ADC measurements at diagnosing specific epithelial tumour subtypes (95).

From a biological perspective, the treatment response findings presented here may be explained by the higher cellular density and microstructural heterogeneity that is present in rapidly proliferating tissue, which can be probed histologically with Ki-67 and non-invasively by K_{app}. Rapidly dividing and heterogeneous tumours may be more sensitive to therapies that target cellular replication, such as carboplatin which inhibits DNA synthesis required for new cell development (112) and paclitaxel which disrupts the microtubule formation necessary for mitosis (113). In additional to this, more proliferative epithelial ovarian cancer subtypes like HGSOC are known to respond better to chemotherapy than low grade serous ovarian cancer (114). Low proliferation in epithelial ovarian cancer was also previously found to relate to chemoresistance (115) and a number of other high Ki-67 expressing cancers have been shown to be more sensitive to chemotherapy (98, 99). These past studies

all support the possibility of a true relationship between HGSOC proliferation measured by K_{app} and response to NACT treatment.

A further application of DKI, could be to investigate tumour microstructure and growth alongside Ki-67 and other immunohistochemistry or histological markers. Unlike Ki-67 tissue measurements that are taken from a small section of tumour, DKI could be used to study proliferation across a larger lesion or to assess multiple cancer deposits simultaneously. HGSOC tumours are known to be heterogeneous (116, 117) and therefore a biopsy sample may not be representative of the Ki-67 expression and cellularity across the entire tumour volume. DKI measurements from the full tumour burden may therefore provide complementary information to that gained from biopsy specimens alone.

This study's limitations include the possibility of sampling error in the tissue that was used to quantify Ki-67 expression and cellularity, as only small areas of tumour were represented on histology while the diffusion imaging parameters that these specimens were compared to originated from larger volumes of tissue. Other confounding factors that may have influenced treatment response but were not considered include the initial tumour burden of patients, the stage of the disease at recruitment, patient co-morbidities and genetic factors such as the presence of *BRCA* and *TP53* mutations that can influence the effectiveness of chemotherapy (118-120).

In conclusion, this study provide evidence of a potentially clinically-relevant relationship between DKI-derived diffusion metrics and the response to neo-adjuvant chemotherapy in HGSOC, particularly with regards to those treatments involving drugs that target cellular proliferation. These findings have the potential to be applied to stratify treatment in ovarian cancer and to rapidly escalate patients to alternative targeted or combinational therapeutic approaches, while reducing morbidity from the side effects of less efficacious drugs. DKI may also offer clinical value as an adjunct to histopathology for the measurement of ovarian cancer proliferation. There is now a need for larger trials to further explore the applications of DKI in HGSOC patients and other tumour types. A larger dataset would also enable a receiver operating characteristic (ROC) analysis of K_{app} value and response to treatment that could be used to look for a cut-off of K_{app} value that may predict response to NACT.

Chapter 4

Sodium MRI in ovarian cancer

4.1 Background

In a simple two compartment model of tissue, the tissue sodium concentration (TSC) is a weighted average of the intracellular and extracellular sodium concentrations that can be expressed as:

$$\mathrm{TSC} = [\mathrm{Na^+}_{\mathrm{EC}}] \,.\, \mathrm{EV_f} + [\mathrm{Na^+}_{\mathrm{IC}}] \,.\, \mathrm{IV_f}, \tag{4.1}$$

Where $\mathrm{EV_f}$ is the extracellular volume fraction, $\mathrm{IV_f}$ is the intracellular volume fraction, $[\mathrm{Na^+}_{\mathrm{EC}}]$ is the extracellular sodium concentration and $[\mathrm{Na^+}_{\mathrm{IC}}]$ is the intracellular sodium concentration. However, because

$$\mathrm{EV_f} = 1 - \mathrm{IV_f} \tag{4.2}$$

and cellular density, ρ_c is proportional to $\mathrm{IV_f}$, equation (4.1) can be rewritten as

$$\mathrm{TSC} = [\mathrm{Na^+}_{\mathrm{EC}}] - \mathrm{k} \,.\, ([\mathrm{Na^+}_{\mathrm{EC}}] - [\mathrm{Na^+}_{\mathrm{IC}}]) \,.\, \rho_c \tag{4.3}$$

Where k is a scaling factor for the conversion of $\mathrm{IV_f}$ to cellular density. Assuming, $[\mathrm{Na^+}_{\mathrm{EC}}] \geq [\mathrm{Na^+}_{\mathrm{IC}}]$, it can be inferred from the above expression that TSC measured by MRI would have approximately a negative linear relationship with ρ_c.

In cancer treatment the aim is to reduce the cellular density of tumours by destroying cancerous cells. If TSC from sodium MRI (^{23}Na-MRI) is able to measure ρ_c then ^{23}Na-MRI may also be of clinical value for monitoring cell death after cancer treatment.

Body imaging using sodium MRI is technically challenging. The signal from sodium MRI is significantly smaller than the signal in proton MRI. This is because of the lower abundance of sodium in the human body compared to ^{1}H, the spin on the sodium nucleus of 3/2 compared with 1/2 for hydrogen and the gyromagnetic ratio of sodium, 70.8×10^{6} $radT^{-1}s^{-1}$ (11.26 MHz/T) which is 4 times smaller than that of ^{1}H. When all effects are considered, the total sodium signal available on MRI in human tissue is only about 1/22,000th the size of the proton signal (121). High static magnetic (B_0) fields must therefore be used with sodium MRI to compensate for the low signal and to improve the signal to noise ratio. A further challenge in sodium imaging is that after radiofrequency (RF) excitation, there is a rapid bi-exponential decay of the sodium signal that drastically limits the timeframe during which an image can be recorded. As a result of this, very fast filling of *k*-space must always be employed in sodium imaging.

Because of a difference in the T_1 relaxation times of free and bound sodium it is possible to separate the intracellular and extracellular signal on sodium MRI to create tissue sodium concentration (TSC) and intracellular weighted sodium (IWS) maps. Extracellular sodium is in free aqueous solution and has a T_1 of ~47ms whereas intracellular sodium is weakly bound to other intracellular charges and has a much shorter T_1 decay time of only ~22ms. An inversion recovery pulse is therefore able to suppress the longer T_1 signal from extracellular sodium and create images that display only the more physiologically important intracellular sodium concentration.

The peritoneal deposits of HGSOC are more superficially located and more accessible to percutaneous biopsy. For this reason, peritoneal HGSOC tissue is often sampled clinically and studied in research. Multi-regional sampling of tissue and repeat sampling during therapy however is often not practical due the invasive nature of the biopsy procedure. Imaging provides an alternative means to biopsy of investigating entire heterogeneous tumour volumes and of following cancer progress over time and sodium MRI may assist in the non-invasive investigation of peritoneal HGSOC. This study looks at the application of

^{23}Na-MRI using 3D-cones in the imaging of peritoneal cancer deposits in HGSOC and explores the relationship of histologically measured tumour cellularity with the imaging. Results from this chapter have been published in the European Journal of Radiology Open (122).

4.2 Methods

Study design and patient recruitment

This was a single centre imaging feasibility study with an exploratory element to investigate the biological factors responsible for the sodium MRI signal. Patients were recruited under the MISSION-ovary research protocol with the only alteration to the inclusion and exclusion criteria being that the patients were required to have superficial peritoneal deposits of cancer detectable on CT.

Differences in the sodium MRI, DKI and MT patient groups which were all recruited from MISSION-ovary also emerged due to limitations on patient tolerance of long scan times that led to omission of one or more type of imaging for some patients and because of the requirement for specialist physics support for sodium imaging that was not always available.

MRI technique

^{23}Na-MRI and ^{1}H-MRI were carried out on patients using a 3T MR system (MR750 GE Healthcare, Waukesha WI). The ^{23}Na-MRI was performed with a custom made single-channel transmit/receive surface coil using a 3D-cones readout (123) which has been shown to provide better contrast and more reproducible results than other k-space sampling trajectories such as cylindrical stack-of-stars (SOS) and 3D-spokes kooshball (124). An adiabatic pulse was used for inversion in IWS imaging and an isotropic resolution of 5.6 mm was prescribed for both TSC and IWS imaging. Sodium calibration phantoms were included in the imaging field of view (FoV) for use in generating sodium concentration maps. The repeatability of this imaging method was demonstrated in an earlier study performed by a group at the University of Cambridge Department of Radiology and Manchester University (125). Phantoms consisted of 50 mL tubes of diameter 6 cm containing sodium chloride

(NaCl) with 4% agar at two sodium concentrations: 20 mM and 80 mM. T_2-weighted ^{1}H-MRI was performed with a fast spin echo pulse sequence and a 32-channel cardiac array. Patients were not moved or repositioned during the coil change. The radiofrequency (RF) power used for the ^{23}Na-MRI was adjusted for each patient to achieve penetration up to a maximum depth of 12 cm which was sufficient to image the peritoneal lesions in all cases. Detailed scan parameters for sodium and proton imaging are given in Table 4.1.

Imaging parameter	**^{23}Na-MRI TSC and B_1 mapping**	**^{23}Na-MRI IWS**	**^{1}H T_2-weighted**
TR	*100 ms*	*250 ms*	*4000 ms*
TE	*0.5 ms*	*0.5 ms*	*91.1 ms*
TI	*n/a*	*30 ms*	*n/a*
Flip angle	*90° for TSC,* *30° and 60° for B_1 mapping*	*90°*	*90°*
Slice thickness	*5.6 mm*	*5.6 mm*	*6 mm*
In plane resolution	*5.6 mm x 5.6 mm*	*5.6 mm x 5.6 mm*	*1.33 mm x 1.33 mm*
FoV	*30 cm*	*30cm*	*34.0 cm x 29.9 cm*
Matrix	*50 x 50 (reconstructed to 120 x 120)*	*50 x 50 (reconstructed to 120 x 120)*	*256 x 256*
NEX	*6*	*6*	*8*
ETL	*n/a*	*n/a*	*16*
Total scan time	*1 min 58 sec*	*4 min 56 sec*	*1 min 54 sec*
Pulse sequence	*GE with 3D-Cones readout*	*IR- GE with 3D-Cones readout*	*Single shot fast spin echo (SSFSE)*

Table 4.1: Imaging parameters for TSC (total sodium concentration), IWS (intracellular weighted sodium) and T_2-weighted imaging. TR = repetition time, TE = echo time, TI = inversion time, FoV = field of view, NEX = number of excitations, ETL = echo train length, GE = gradient echo.

Post processing

Processing of sodium images was carried out with in-house software written in MATLAB (The MathWorks Inc., Natick, MA, 2000). The method described by Miller (1993) was used to remove noise from the images (126). This correction is suitable for use in low SNR images. Briefly, the correction involves squaring the image, selecting an ROI in a background region with noise only and no true signal, measuring the mean pixel value in this background region and subtracting this value from all pixels in the squared image.

Radiofrequency field inhomogeneity correction

Because of a loss of signal intensity due to reduced RF penetration deep into tissues a B1 artefact (transmit and receive) correction had to be performed on images. A B1 map was created using the dual angle method for gradient echo (127, 128) with images collected at flip angles of 30° and 60°. Using this method for 2 images formed with nominative flip angles α_{nom} and $2\alpha_{nom}$ the ratio, rI, of the image intensities was,

$$\mathrm{rI} = \sin(\alpha_{nom}) / \sin(2\alpha_{nom}) = 1 / 2\cos(\alpha_{nom}) \tag{4.4}$$

which gave a relative flip-angle (or equivalently B1 field) correction factor (rB1) of,

$$\mathrm{rB1} = [\cos^{-1}(1 / 2\mathrm{rI})] / \alpha_{nom} \tag{4.5}$$

True flip angles (α_{true}) were then calculated by multiplying the nominative flip-angle by the rB1 value calculated at each pixel.

After calculating the true flip angle maps for the images, a signal correction formula was derived as follows to compensate for the non-uniformities of both the transmit and the receive fields.

For the transmit B1 the gradient echo signal, S, was given by the formula,

$$S \propto [\mathrm{Na}] \frac{\sin(\alpha_{true})\left(1 - e^{-TR/T1}\right)}{(1 - (\cos(\alpha_{true}))e^{-TR/T1})} \tag{4.6}$$

This equation can be simplified because for the sodium pulse sequence used in this study TR >> T_1, causing $e^{-TR/T1}$ to approach zero, resulting in the approximation of,

$$S \propto [Na].\sin(\alpha_{true}) \quad (4.7)$$

When compensating for the receive-only B1 for a surface coil, the signal, S is also directly proportional to the receive B1 so that,

$$S \propto \alpha_{true} \quad (4.8)$$

The overall relationship of the combined receive and transmit signal to the flip angle coul therefore be reduced to:

$$S \propto [Na].\alpha_{true}.\sin(\alpha_{true}) \quad (4.9)$$

or,

$$[Na] \propto S/[\alpha_{true}.\sin(\alpha_{true})] \quad (4.10)$$

Signal from the B1 maps was masked to exclude from the image analysis areas with very low flip angle and areas with flip angles that would create unwanted inversion. This was because in such regions the signal was considered too small in comparison to image noise to give reliable quantitative information on sodium concentration. Areas with flip angle 5% greater than or less than 180° and 360° were removed.

Sodium maps (TSC and IWS) were calculated from a calibration curve created with phantoms included in the field of view of the patient scans. ROIs were selected from inside the tubes and used to derive the linear relationship between Na^+ concentration and MR signal based on the method described by Christensen JD et al (129). This involved solving simultaneous equations of the form (4.11) and (4.12) for a and b where C_1 and C_2 were the known sodium concentrations of the calibration phantoms and S_1 and S_2 were the corresponding imaging signal intensities for these phantoms. Leading to a linear calibration equation of the form shown in (4.13).

$$C_1 = aS_1 + b \quad (4.11)$$

$$C_2 = aS_2 + b \quad (4.12)$$

$$C = a + bS \quad (4.13)$$

where, $a = \frac{C_1 - C_2}{S_1 - S_2}$ and $b = \frac{C_2 S_1 - S_2}{S_1 - S_2}$

ROIs were drawn on the T_2-weighted images by a single observer using OsiriX (version 3.8.1, Pixmeo, Geneva, Switzerland) around all slices encompassing complete peritoneal deposits and around the adjacent areas of right gluteal muscle as a normal reference tissue for comparison with the tumour. Only solid areas of cancer on the T_2-weighted images were included. ROIs were restricted to superficial areas where the signal was not masked and care was taken to avoid areas with artefact. The ROIs were reviewed by a radiologist with eight years of experience as an attending physician and co-registered with the sodium maps to which the ROIs were imported for analysis. For patients with multiple peritoneal deposits, ROIs were combined into a single tumour volume.

Tissue samples were collected from the peritoneal deposits of patients 1-14 days (median 7 days) after imaging either by ultrasound guided biopsy or at surgery. Samples were fixed in paraffin blocks for storage and cut into 3 µm sections that were retrieved with sodium citrate. Sections were stained with haematoxylin and a cell count and tissue area quantification were performed on the sections using automated histology image analysis software (Halo, v2.1.1637.11, Indica labs). Cellularity (cell density), ρ_c was estimated from the cell count (N) and tissue area (A) in μm^2 as follows:

$$\rho_c = N / A * 1000 \quad (4.14)$$

Statistics

All statistical analysis was performed in R (v2.15.3, R Foundation for Statistical Computing, Vienna, Austria). For comparison of means, the Shapiro-Wilk test was used to assess data for normality and the Student's *t*-test or Wilcoxon test was then applied to evaluate significance. Cellularity was compared to sodium concentrations from MRI (TSC and IWS) using Spearman's correlation.

4.3 Results

Patients

Twelve high grade serous ovarian cancer patients were recruited: median age 69 (range 52-81) years. The majority of patients (10/12) had FIGO (Fédération Internationale de Gynécologie et d'Obstétrique) stage III or IV disease. Table 4.2 gives detailed sample population characteristics.

Feature	Value
Number of patients	12
Age, median (range, years)	69 (52-81)
ECOG performance status (number of patients)	
0-2	9
3-4	3
FIGO stage (number of patients)	
I	0
II	2
III	8
IV	2
Serum CA 125 (IU/ml, number of patients)	
0-100	4
100-500	3
>500	5

Table 4.2: Population demographics of patients recruited. ECOG = Eastern Cooperative Oncology Group, FIGO = Fédération Internationale de Gynécologie et d'Obstétrique, CA 125 = cancer antigen 125.

Imaging

Signal-to-noise ratios of 82.2 **±** 15.3 and 15.1 **±** 7.1 were achieved for tumour TSC and IWS imaging respectively. The total sodium imaging time for each patient was under 11 minutes (TSC imaging = 1 min 58 sec, IWS imaging = 4 mins 56 sec, images for dual flip angle mapping = 3 min 56 sec). When the time for positioning and localisation with proton imaging is added the average time for a sodium imaging session increases to around 20 minutes. High signal intensity artefacts appeared at the edges of images after RF field inhomogeneity corrections because of small mismatches in alignment between B_1 maps and sodium signal images at the interfaces of high sodium signal changes such as between air and tissue. These

mismatches were primarily due to patient movement and were found exclusively at imaging borders and therefore were not present on ROIs derived from peritoneal deposits or muscle. Examples of the ^{23}Na-MRI images and changes with post-processing are shown in Figure 4.1.

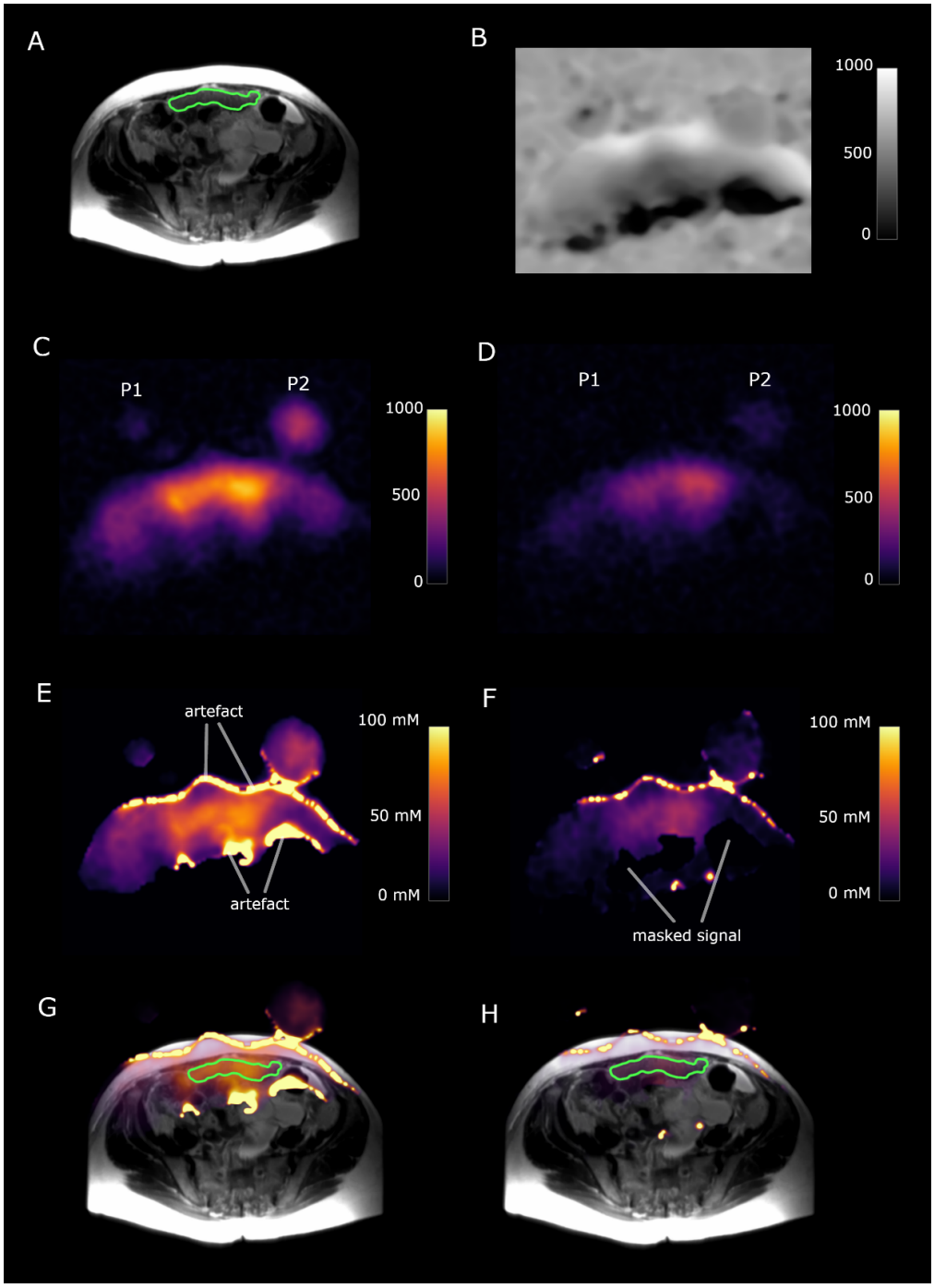

Figure 4.1: 73-year old high grade serous ovarian cancer patient. P1 and P2 represent slices through the two sodium phantoms. The green outline shows a peritoneal cancer deposit. (A) T_2-weighted image. (B) Sodium B_1 map, scale bar represents arbitrary units. (C) Total sodium image; scale bar represents image intensity. (D) Intracellular weighted sodium image; scale bar represents image intensity. (E) Masked total sodium concentration map; scale bar represents sodium concentration in mM. (F) Masked intracellular weighted sodium concentration map, scale bar represents sodium concentration in mM. (G) Fused T_2W image and total sodium concentration map. (H) Fused T_2W image and intracellular weighted sodium concentration map.

Sodium quantification and tumour cellularity

The mean tumour volume analysed from the regions where the sodium maps were successfully constructed was 45 ± 24 mL. The TSC concentrations for peritoneal cancer deposits and gluteal skeletal muscle were 56.8 ± 19.1 mM and 33.2 ± 16.3 mM respectively (mean ± standard deviation); Wilcoxon signed-rank test for difference between groups, $P < 0.001$. IWS values for peritoneal cancer and muscle were 30.8 ± 9.2 mM and 20.5 ± 9.9 mM respectively; Wilcoxon signed-rank test for a difference between these two groups, $P = 0.01$. These results are summarised in the boxplots shown in Figure 4.2.

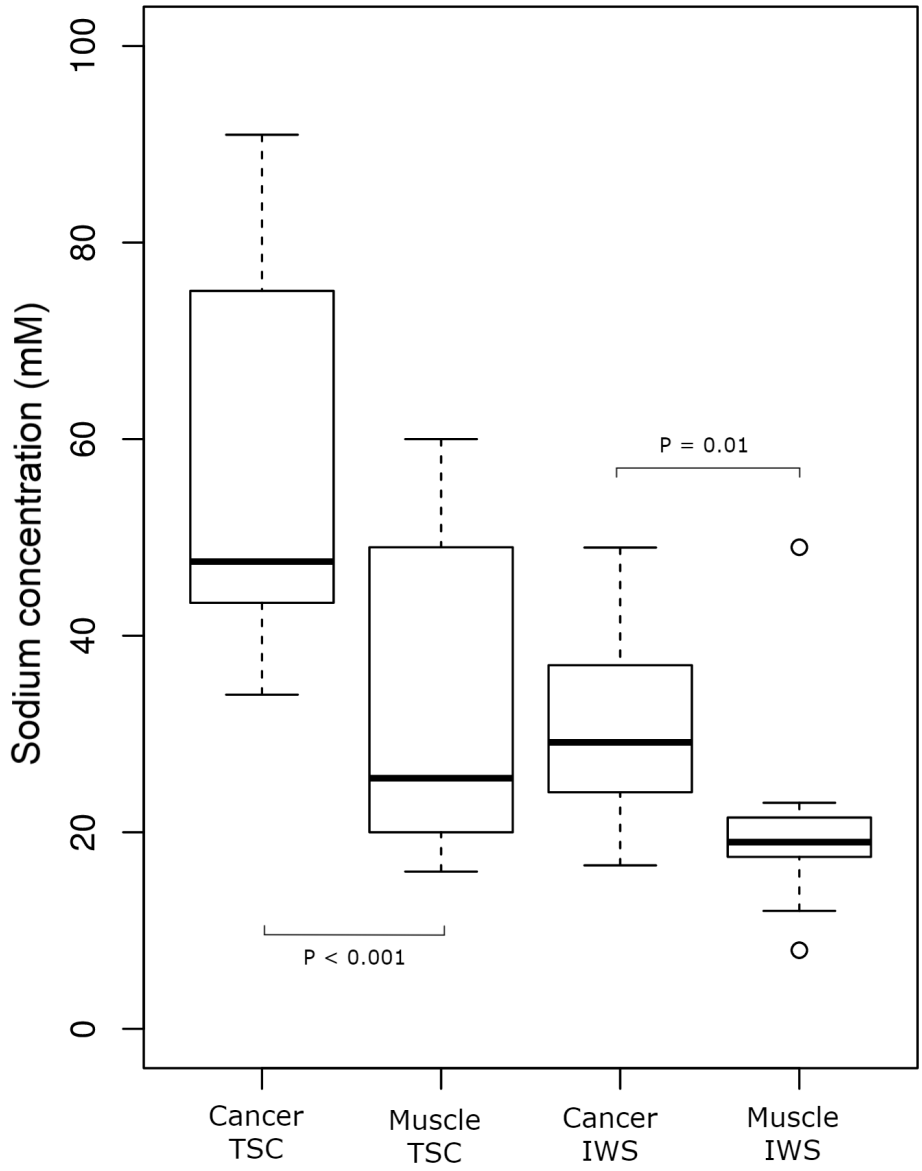

Figure 4.2: Box plots showing TSC (total sodium concentration) and IWS (intracellular weighted sodium) values for cancer and muscle.

An example of the typical histological appearances for a 73-year old HGSOC patient are shown in Fig. 4.3 together with the automated cell counting segmentation. Scatterplots of tumour cellularity (ρ_c) compared with sodium concentrations as measured on imaging are shown in Fig. 4.3 (C) and 4.3 (D). TSC displayed a strong negative correlation with cellularity, Spearman's rho = -0.92 and $P < 0.001$. There was no significant Spearman correlation found between IWS concentration and cellularity, $P = 0.44$.

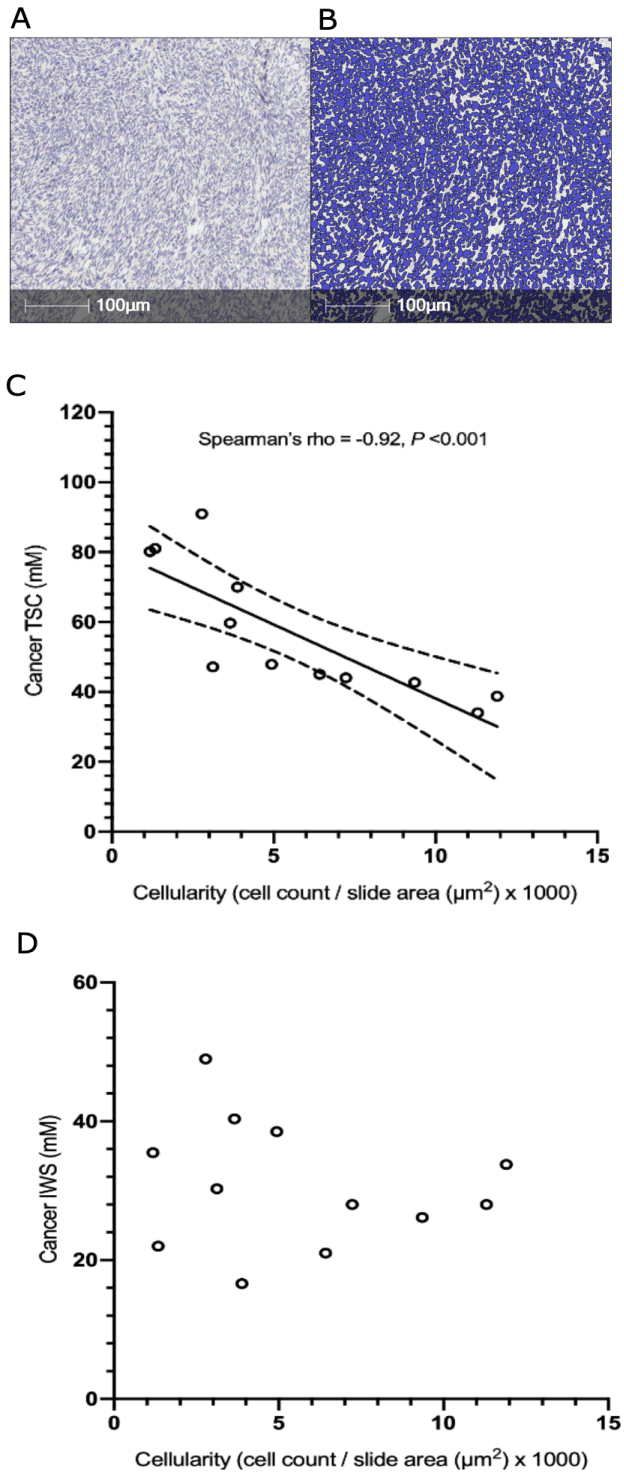

Figure 4.3: Tumour tissue from a 73-year old high grade serous ovarian cancer patient; (A) 1x magnification haematoxylin stained slide of tumour tissue; (B) automated cell segmentation used for cell counting. Scatterplots of; (C) tissue sodium concentration against cellularity, (D) intracellular weighted sodium concentration against cellularity.

4.4 Discussion

This study demonstrated the feasibility of using ^{23}Na-MRI to image peritoneal lesions in high grade serous ovarian cancer patients for the first time. The completion of sodium imaging in approximately eleven minutes was enabled using a 3D-cones readout, a surface transmit/receive coil and a post-processing analysis method to correct for RF field non-uniformity. Short acquisition times are important for the clinical translation of ^{23}Na-MRI and these results represent a moderate improvement to previously reported scan times in the abdomen. The comparison of tumour sodium quantification to histology preformed here also provided validation that TSC measured by ^{23}Na-MRI is an effective biomarker of tumour cellularity.

Sodium MRI has been used in the past to demonstrate the higher sodium concentration of cancers compared to healthy tissue. One study demonstrated a 63% higher TSC in malignant breast lesions compared to glandular tissue (130). Other studies in glioma have found increases in both the IWS and TSC of glioma compared to normal appearing white matter (NAWM) (131). These results are in agreement with the higher sodium concentrations found here for ovarian cancer compared to healthy tissue. The higher standard deviation of TSC also agrees with previous evidence that IWS is more tightly regulated than TSC and the fact that HGSOC is known to be heterogeneous in nature.

Cellularity has already been shown to relate to the outcome of cytoreduction in HGSOC (132) and to be predictive of the response of breast cancer to neoadjuvant chemotherapy (133). In breast cancer cellularity is also used more directly in the Miller-Payne method for the histological assessment of treatment response (134). For HGSOC treatment, the first line chemotherapy regimen of a combination of a platinum-based drug and a taxane has not changed for the past 30 years despite poor patient outcomes (116). There is now ongoing research to develop more targeted HGSOC therapies like PARP (poly ADP-ribose polymerase) inhibitors (135), VEGF (vascular endothelial growth factor) inhibitors (136) and immune checkpoint inhibitors (137) in an attempt to improve the outlook for the disease.

With the emergence of new therapies in heterogeneous cancers like HGSOC, there is an associated need for imaging to provide greater detail on tumour structure and function so that patients can be better stratified to the optimal treatment option for their particular

subtype of disease. The availability of alternative therapies also provides the opportunity for non-responsive patients to switch to more effective drugs and increases the urgency for the development of reliable early response detection methods. The measurement of cellularity with ^{23}Na-MRI demonstrated here provides information on tumour composition and can potentially be employed to monitor the evolution of tumour cellular content over time and following treatment. This could have implications for patient management in HGSOC and other malignancies where the detection of cell death and the monitoring of cellularity changes are of clinical relevance. Unlike other imaging methods like diffusion MRI that may also measure cellularity, ^{23}Na-MRI has the advantage that it is unlikely to be as affected by the presence of physical structures like membranes or fibrous tissues that alter diffusion.

Despite the strong significance of the relationship between TSC and cellularity found here, no correlation between cellularity and IWS could be detected. IWS concentration in cancer is influenced by a large number of biological processes that may have a greater effect on the IWS concentration than cellularity. For example, the IWS ^{23}Na-MRI signal may be affected by the energy status of tumours due to the ATP and oxygen requirements of the sodium pump (138, 139). In cancer there is mitochondrial dysfunction (140) as well as metabolic reprogramming that shifts glucose away from the production of ATP by oxidative phosphorylation and towards the manufacture of new nucleotides, lipids and amino acids needed for cell replication and unregulated tumour growth (141, 142). Voltage gated sodium channel expression is also upregulated in many cancers (143-145) and although the purpose of these channels in cancer is not yet clear they may represent a further mechanism by which the intracellular sodium concentration is altered in malignancy. Furthermore, aggressive tumours such as HGSOC have higher Na^+/H^+ antiporter activity which allows sodium to enter the cell in exchange for a H^+ efflux, that is used to create an acidic extracellular environment to stimulate enzymes that breakdown of surrounding extracellular matrix structures and facilitate cancer invasion (146). TSC signal in comparison to IWS is more dominated by the high concentration of sodium in the extracellular space and is less affected by the movement of sodium in and out of cells. This is because TSC is a measure of total tissue sodium that includes both the intracellular and extracellular environments.

The findings of this study are limited by the possibility of errors introduced by patient movement during the sodium/proton coil change and the creation of edge artefacts in post-processing. The optimisation of RF power to image superficial peritoneal lesions also meant that gluteal sodium measurements could not include some deeper muscle regions. Reasonable measures were taken to minimise the effects of these limitations however through the exclusion via masking of possible inaccurate sodium map areas and the application of an RF inhomogeneity correction.

In conclusion, rapid ^{23}Na-MRI using 3D-cones was successfully performed in a technically challenging area of the body. This study shows for the first time that ^{23}Na-MRI can assess peritoneal deposits in HGSOC patients and that TSC measured by ^{23}Na-MRI correlates strongly with tumour cellularity. The non-invasive quantification of sodium using MRI has the potential to provide information on cell viability, sodium transporters, metabolic activity, cell membrane integrity and tumour response to therapy. The rapid scanning method shown here demonstrates that larger human studies to evaluate ^{23}Na-MRI in the abdomen are feasible. Further work is now needed to investigate other clinical applications of sodium MRI and to explore the utility of TSC in monitoring cellularity changes in response to cancer treatment.

Chapter 5

The repeatability of magnetization transfer imaging in the female pelvis

---

5.1 Background

Before addressing the use of MT imaging in ovarian cancer a study on the repeatability of the technique was performed in the healthy female pelvis. The aim of this work was to determine whether the pelvic imaging was sufficiently repeatable and could subsequently be applied to the study of ovarian cancer. This data was collected at the University of Cambridge Department of Radiology prior to the start of this PhD but was analysed by me during the PhD.

Magnetization transfer ratio (MTR) is defined as the percentage change in signal with the "off –resonance" pulse off and on. Mean MTR values have been reported for MT performed on a diverse set of body structures and tissues in health and disease. Work on the post-mortem brains of multiple sclerosis (MS) patients found mean MTRs of 30.0% ± 2.9 in remyelinated white matter lesions and 23.8% ± 4.3 in demyelinated lesions (147). Other brain studies generated MTR 30.77% ± 0.29; *P* = 0.037 for grey matter in patients with mild cognitive impairment and 29.37% ± 0.41; *P* = 0.000) in those with Alzheimer's dementia (148). A study on whole body MT imaging produced MTR results for white matter of 51.1% ± 1.0, for gray matter of 42.2% ± 1.3, for skeletal muscle 50.3% ± 2.1, liver 39.4% ± 3.2, spleen 31.8% ± 2.6, renal cortex 30.4% ± 1.9 and renal medulla 25.6% ± 1.3 (149). In another published study, MTR was 34.4%-54.9% for muscle, 10.3%-12.6% for subcutaneous fat and 22.8% - 46.9% (P < 0.001) for liver at frequency offsets greater than 400Hz (150). Similar research on prostate generated MTRs in the range of 6.18% ± 1.63 for healthy controls (151). Imaging of fibrotic bowel wall using two different mouse models of Crohn's disease, produced mean normalized MTRs of 0.45 ± 0.05 and 0.58 ± 0.08 (P = 0.0003) for the two

models using a 10 kHz off-resonance pulse and mean normalized MTRs of 0.53 ± 0.08 and 0.64 ± 0.07 (P = 0.003) for the two models using a 5 kHz off-resonance pulse (152). Previous pelvic MT work produced MTR values of (23.8% ± 6.7, P < .01) for normal cervical stroma and (24.3% ± 3.6, P < .01) for normal endometrium (153).

There are very few repeatability studies involving MT. One such study undertaken in the brain explored areas of white matter and resulted in an MTR value averaged over time for five participants of 30.1% but did not use coefficient of variation (COV) to estimate repeatability. Instead this study used the test/retest reliability coefficient although it did recommend COV calculations as an alternative method of performing a repeatability analysis (154). This chapter presents an example of the measurement of MTR in major pelvic tissues and their repeatability. MTR results of repeatability experiments from the female pelvis have never previously been published.

5.2 Methods

Six healthy female volunteers aged 23 to 54 were recruited for pelvic imaging. They were scanned at 1.5T on two separate sessions approximately one week apart. Imaging was performed with body coil excitation and a 12-channel receiver array (Discovery MR450, GE Healthcare, Waukesha WI). For premenopausal women, both sets of scans were completed between days 6 and 14 of the menstrual cycle. MT images were acquired via a 3D fast spoiled gradient echo (FSPGR) sequence (TR 15 ms, TE 1.1 ms, FOV 38 cm, matrix 192x192, 32 or 64 slices, thickness 5 mm) applied with and without an additional 8ms Fermi pulse (offset 2200Hz, nominal flip angle 360°). Fractional MTR maps were calculated as;

$$(MT_{off} - MT_{on}) / MT_{off} \times 100 \qquad (5.1)$$

ROIs were drawn directly onto MTR maps to sample signal from different tissue types. Matched regions of interest (ROIs) from the two examinations that each volunteer underwent were selected and analyzed with ImageJ (155). The mean pixel intensity and standard deviation for the ROIs was calculated from the ImageJ measurements.

The mean MTR across all participants was found for selected pelvic tissue types. MTR values were reported with and without normalization to gluteal muscle. Normalization was performed by dividing the mean ROI MTR by the mean gluteal muscle MTR of individual images. This normalization would be expected to be necessary if there were variations in MTR due to hardware performance or other inter-subject factors. The change in MTR with repeat imaging for each tissue type was assessed via the test-retest coefficient of variation (COV). The COV was found by dividing the standard deviation, σ_i for each pair of MTR values by its mean, μ_i according to equation (5.2) below (156) .

$$\mathrm{COV} = \frac{\sigma_i}{\mu_i} \tag{5.2}$$

The root mean square coefficient of variation (RMS COV) for each tissue type from the volunteers was then calculated as:

$$\mathrm{RMS\ COV} = \sqrt{\frac{\sum_{i=1}^{i=n}\left(\frac{\sigma_i}{\mu_i}\right)^2}{n}} \tag{5.3}$$

where n is the number of tissue sample pairs identified.

RMS COV represents an estimate of the variability in signal between repeat images. Not all tissue types explored in this study were identifiable in every volunteer. Only samples where the tissue could be convincingly identified were included. Samples were also removed from the analysis if the co-registration between scans could not be accurately performed. As a result, the sample sizes for the pelvic tissues analysed in this study varies slightly.

No formal hypothesis testing was performed in this repeatability study but a RMS COV of less than 20% was taken as an indicator of good repeatability.

5.3 Results

Tissue MTR values

It was possible to identify nine different tissue types in the images we collected. Mean first visit MTR values from fat and bone were low with a value of 2.39 ± 0.91 for subcutaneous fat and 3.35 ± 1.16 for bone from the femoral head. Conversely, the gluteus maximus muscle displayed a first visit MTR almost twenty times greater than fat at 41.85 ± 3.87. Myometrial MTR was slightly lower than skeletal muscle MTR at 32.66 ± 3.94.

Figure 5.1 shows the repeat MT images and region of interest (ROI) selections from the femoral heads 5.1 a and b and the gluteal muscle 5.1 c and d for a pair of scans from one participant.

The mean MTR values before and after normalization for each tissue type are shown in Table 5.1 and Table 5.2 respectively. The magnitude of the percentage change in normalized and non-normalized MTRs with repetition are also given.

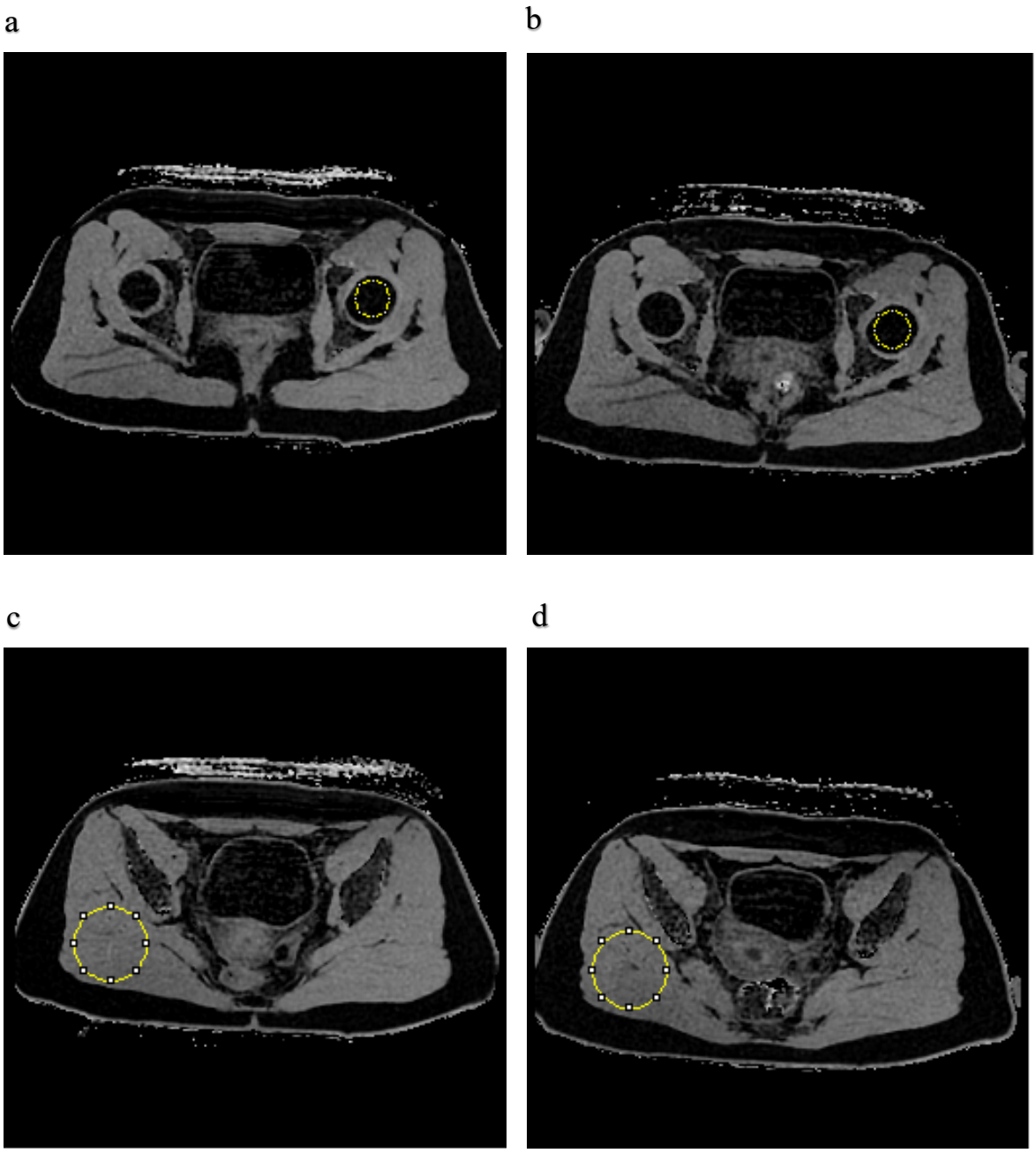

Figure 5.1: ROI from the left femoral heads on (a) test and (b) re-test scans: images are from the same patient and were analyzed using ImageJ. (c) Test and (d) re-test ROI selection for gluteal muscle.

Coefficients of variation (COV)

Coefficients of variation for different tissue types ranged from 3.7% for muscle to 49.0% in bone before normalization. Myometrial MTR showed good repeatability (RMS COV 6.8%), Normalized and non-normalized RMS COV values for all the tested tissues are displayed in Table 5.1 and Table 5.2 respectively and graphically in Figure 5.2.

Tissue type	Visit 1 MTR (Mean ± SD)	Visit 2 MTR (Mean ± SD)	Mag. of % change in MTR (Mean ± SD)	RMS COV (%)
Subcutaneous fat (n=5)	2.39 ± 0.91	2.15 ± 0.54	23.6 ± 7.1	17.7
Right femoral head (n=4)	3.35 ± 1.16	2.51 ± 1.05	45.8 ± 31.1	49.0
Bladder contents (n=4)	4.03 ± 1.80	3.27 ± 1.48	18.9 ± 10.4	17.0
Vertebral body (n=4)	13.09 ± 6.82	13.37 ± 7.39	31.8 ± 26.5	22.3
Bowel (n=5)	20.09 ± 3.14	18.96 ± 2.68	16.8 ± 14.3	15.2
Myometrium (n=4)	32.66 ± 3.94	33.06 ± 3.17	8.9 ± 4.7	6.8
Intervertebral disc (n=4)	37.33 ± 3.34	38.40 ± 2.03	8.3 ± 1.6	5.9
Psoas (n=5)	41.42 ± 4.47	42.33 ± 1.80	9.9 ± 9.8	8.6
Gluteus maximus (n=5)	41.85 ± 3.87	42.46 ± 2.43	4.6 ± 2.9	3.7

Table 5.1: Table of non-normalized mean percentage MTR and RMS COV values for the selected pelvic tissues.

Tissue type	Visit 1 MTR (Mean ± SD)	Visit 2 MTR (Mean ± SD)	Mag. of % change in MTR (Mean ± SD)	RMS COV (%)
Subcutaneous fat (n=5)	0.06 ± 0.03	0.05 ± 0.01	23.0 ± 9.5	18.6
Right femoral head (n=4)	0.08 ± 0.03	0.06 ± 0.02	43.5 ± 32.9	49.5
Bladder contents (n=4)	0.09 ± 0.04	0.08 ± 0.03	20.3 ± 8.6	17.4
Vertebral body (n=4)	0.31 ± 0.16	0.30 ± 0.16	35.5 ± 32.6	24.7
Bowel (n=5)	0.49 ± 0.10	0.45 ± 0.05	19.3 ± 11.5	16.3
Myometrium (n=4)	0.78 ± 0.02	0.78 ± 0.03	5.3 ± 0.8	3.8
Intervertebral disc (n=4)	0.86 ± 0.04	0.89 ± 0.02	4.6 ± 1.3	3.3
Psoas (n=5)	1.00 ± 0.13	1.00 ± 0.04	8.0 ± 9.1	7.4
Gluteus maximus (n=5)	1.00 ± 0.00	1.00 ± 0.00	0.0 ± 0.0	0.0

Table 5.2: Table of mean MTR and RMS COV values for the selected pelvic tissues normalized to gluteal muscle

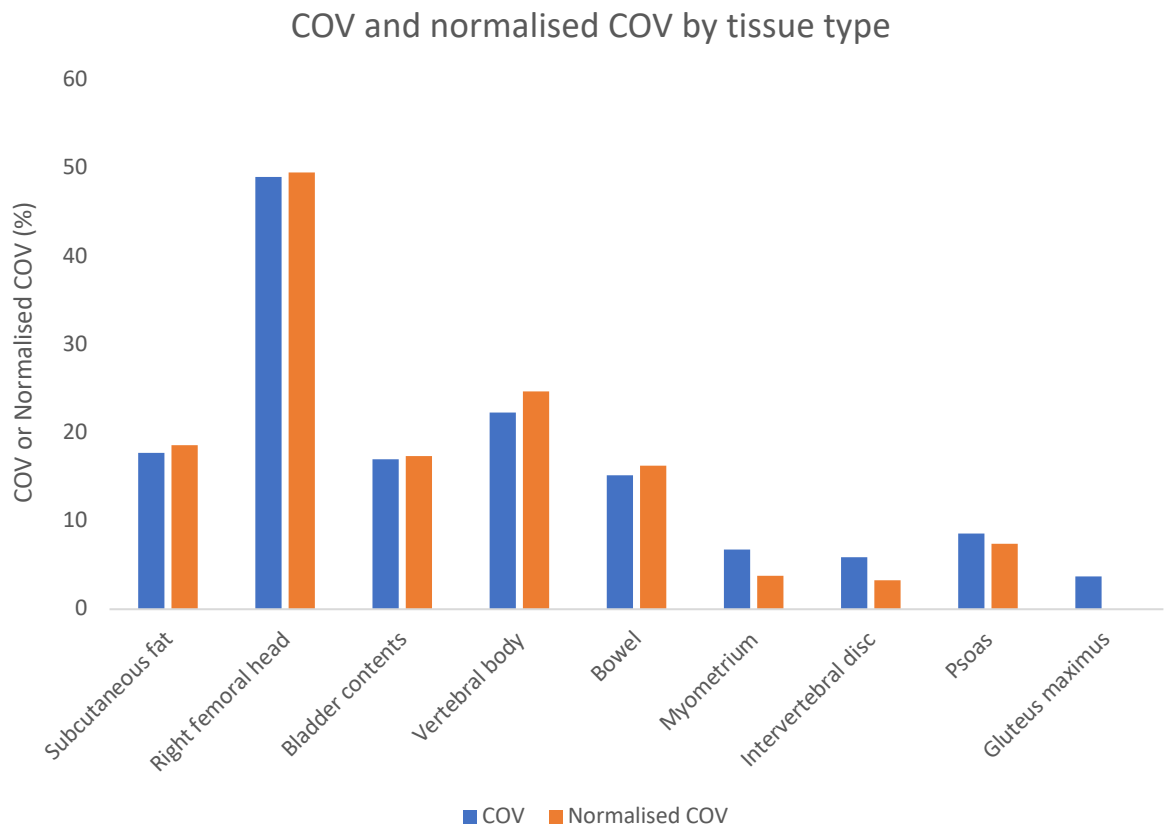

Figure 5.2: COV and normalized COV for the selected pelvic tissues.

5.4 Discussion

In this study, pelvic MT ratios were similar to those previously reported and imaging maps were highly reproducible for most structures in the female pelvis. Repeatability improved only slightly by normalization to gluteal muscle, indicating good hardware performance between imaging sessions. It should be noted however that normalization as performed here has the disadvantage of decreasing the RMS COV for tissues with similar MTR to the tissue used as the standard for normalization (in this case skeletal muscle) as the tissue used as the standard is assigned a base value of 1.00 for each case leading to no variability in the normalized gluteal muscle measurements between samples. For the non-normalized data, myometrium and gluteal muscle showed the greatest levels of consistency between repeat images with RMS COV values of 6.8% and 3.7% respectively. Most other soft tissue types such as subcutaneous fat and fluid displayed RMS COV <20% which is generally considered

to indicate good repeatability for MRI although there is no definite consensus among researcher on his value. At the other end of the spectrum, femoral head and vertebral body had the highest RMS COV values at 49.0% and 22.3%. The MT maps of tissues like muscle and fat had superior repeatability compared to the imaging of cartilage or bone. This may have been influenced by the lower signal in tissues like cartilage and bone being affected to a greater relative degree by constant components of image noise than tissues like muscle with higher signal. The higher consistency measured by RMS COV suggested that MT imaging of the pelvis would be more reliable when used to investigate soft tissue pathology. This would suggest that MT may best be applied to studying lesions within soft tissue organs in the female pelvis and would therefore be viable for ovarian cancer imaging.

Some tissues like fat demonstrated low RMS COV but had low MTR values suggesting that fat demonstrates low MT signal despite good repeatability. Clinical usefulness of the MT imaging of such tissues may however be limited by signal. Another limitation of this study was the difficulty in reliably identifying some anatomy on the MT maps that resulted in some tissues being analysed with fewer than six samples.

This work provides evidence of the consistency that can be achieved from MTR maps in pelvic tissues. Pelvic MT is not yet widely used clinically despite the success of MT in neuroimaging. The demonstration of good repeatability is an important criterion in judging the potential for application of an imaging method to the clinical setting. Based on the results here, MT was subsequently applied at Cambridge to the imaging of macromolecules within ovarian cancer as part of MISSION-ovary and findings from this are presented in the next chapter.

Chapter 6

Magnetization transfer imaging of tumour macromolecules in ovarian cancer

---

6.1 Background

Collagen is the most abundant protein in the human body and the major structural component of the extracellular matrix (ECM). Bound water plays an important part in maintaining the triple helix conformation of collagen and the association of collagen into assemblies of sheets or fibres (157). *In vitro* and animal experiments have demonstrated that the denaturation of collagen can be detected with MT imaging (158, 159). Changes in ECM collagen cross-linking are known to occur in most cancers (160, 161) and in some areas of tumour, the collagen microenvironment is destroyed and rebuilt in a remodelling process to support the changing structural requirements of the tumour (162, 163). Enzymes like metalloproteinases that are overexpressed in cancer degrade collagen while increased activity of immune cells like fibroblasts simultaneously lay down new collagen fibres to support tissue growth and provide attachment sites for tumour cells (164). In epithelial ovarian cancer, remodelling of the ECM is known to occur (165) and in high grade serous ovarian cancer (HGSOC) a collagen-remodelling gene signature has been shown to be associated with poor outcome (166). Both increases and decreases in overall collagen deposition are associated with malignancy (167) and the measurement of total collagen in cancer is consequently difficult to interpret clinically.

The basement membrane (BM) is a component of the ECM that is comprised of a specific type of collagen, type IV collagen or collagen IV. Unlike other parts of the ECM which are remodelled in cancer progression, the BM must be degraded for cancer to spread (168-171). Collagen IV and the protein laminin are major components of the basal lamina layer of the BM. The basal lamina helps to maintain cell polarity, tissue structure and restrict cell

movement (172). Cytoskeletal binding to the basal lamina must be lost in the epithelial-mesenchymal transition (EMT) process through which cancer cells lose their polarity and cell-to-cell adhesion properties and become invasive (173). Collagen IV and laminin expression have both been shown to be of prognostic significance in cancers such as colorectal adenocarcinoma (174) and oral mucosa squamous cell carcinoma (175), where decreased collagen IV and laminin were associated with disease progression.

Tumours that are growing and proliferative produce larger quantities of macromolecular proteins and lipids and are likely to have higher MTRs. MTR could therefore be able to provide information on increases in cell density and tumour expansion and invasion through the BM. In this study the ability of MT imaging to measure tumour cell density and the loss of collagen IV and laminin from the BM is assessed using a cohort of patients with HGSOC.

6.2 Methods

Patient recruitment

Patients were recruited under the protocol of the MISSION-ovary study to undergo MT imaging. The inclusion and exclusion criteria for these patients was therefore the same as previously mentioned for MISSION-ovary and detailed in Section 1.3 of Chapter 1 of this thesis.

Imaging and region of interest analysis

MR imaging was performed on a 3T Discovery MR750 (GE Healthcare, Waukesha WI), with a frequency offset of 2200 Hz for MT imaging. 20 mg of intravenous hyoscine butylbromide was given to participants 10 minutes before scanning to reduce bowel motion. Detailed scan parameters are provided in Table 6.1. Magnetization transfer ratio (MTR) was calculated from MT_{off} and MT_{on} images (Equation (5.1)).

Table of imaging parameters

Imaging parameter	T_2 weighted	MT_{off}	MT_{on}
TR	4000 ms	24ms	24ms
TE	91.1 ms	2.8ms	2.8ms
Flip angle	90°	5°	5°
Slice thickness	6mm	5mm	5mm
FoV	34.0 cm x 29.9 cm	34.0 cm x 34.0 cm	34.0 cm x 34.0 cm
Matrix	256 x 256	256 x 192	256 x 192
NEX	8	1	1
Total scan time	1 min 54 sec	2 min 23 sec	2 min 23 sec

Table 6.1: Scan parameters for T_2 weighted, MT_{off} (magnetization transfer off) and MT_{on} (magnetization transfer on) imaging. TR = repetition time, TE = echo time, TI = inversion time, FoV = field of view, NEX = number of excitations.

Regions of interest (ROIs) were drawn on T_2-weighted images in OsiriX (version 3.8.1, Pixmeo, Geneva, Switzerland) around all ovarian cancer volumes. ROIs were reviewed by a radiologist, with 8 years of experience as a consultant in oncological radiology and who was kept blind to image analysis and subsequent tissue immunohistochemistry results. ROIs were imported from the T_2-weighted images onto MTR maps that were co-registered in Osirix and mean MTRs were calculated for the cancer volumes. For patients with multiple tumour deposits, ROIs were combined to produce one mean tumour MTR value for each patient.

Tissue analysis

Tumor tissue samples were collected from patients 1 to 10 days after imaging (median 7 days). Tissue was fixed in formalin and embedded into paraffin blocks. 3 µm sections were cut from the blocks and slides were stained using Leica's Polymer Refine Detection System

(DS9800) automated Bond platform with haematoxylin, collagen IV antibody (Dako, M0785. Dilution 1:50. Retrieval Proteinase K, 20') and laminin antibody (Sigma, L9393. Dilution 1:1000. Retrieval Sodium Citrate, 5' and Proteinase K, 5'). Bright-field scanning with an Aperio AT2 scanner (Leica) was carried out to digitize slides and a cell count and an area quantification of collagen IV and laminin staining were performed on the digital slides using the multiplex IHC V1.2 module of Halo histology image analysis software (Indica labs v2.1.1637.11). For both collagen IV and laminin, tissue areas with a staining optical density (OD) greater than 0.355 were considered positive. The operator of the analytic software was blinded to MTR imaging results.

Statistics

All statistical analysis was performed in R (version 2.15.3, R Foundation for Statistical Computing, Vienna, Austria) and a *P* value of 0.05 was used as the cut-off to indicate significance. Immunohistochemistry quantification results were compared to the imaging using Pearson's product-moment correlation.

6.3 Results

Seventeen HGSOC patients were recruited. Median participant age was 69 years, range 43 to 81 years. Patient characteristics are summarized in Table 6.2. An example of the typical MT imaging appearances from a 63-year old patient is shown in Figure 6.1. The MTR for the HGSOC lesions of participants was 24.6 ± 3.9% (mean ± S.D.).

Table of population characteristics

Feature	Value
Number of patients	17
Age, median (range) / years	69 (43 to 81)
ECOG performance status (number of patients)	
0-2	13
3-4	4
FIGO stage (number of patients)	
I	0
II	1
III	12
IV	4
Serum CA 125 (IU/ml) (number of patients)	
0-100	4
100-500	5
>500	8

Table 6.2: Population demographics of patients recruited. ECOG = Eastern Cooperative Oncology Group, FIGO = Fédération Internationale de Gynécologie et d'Obstétrique, CA 125 = cancer antigen 125.

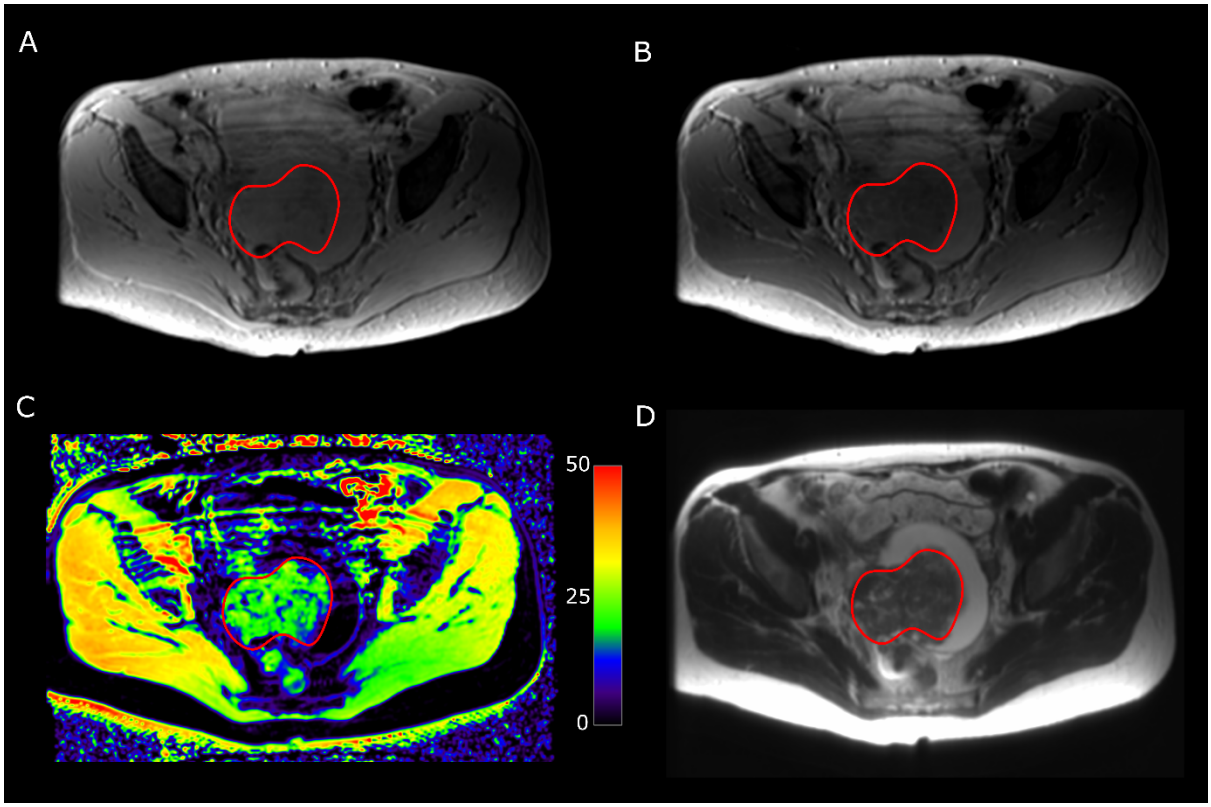

Figure 6.1: Example of typical images from a 63 year old HGSOC participant. Tumour is outlined in red. (A) MT_{off}; (B) MT_{on}; (C) MTR map, scale bar represents MTR in percent; (D) T_2- weighted image.

Examples of haematoxylin, collagen IV and laminin staining for a patient are shown in Fig. 6.2 (a), (b) and (c) respectively. Localization of collagen IV and laminin was primarily in the extracellular space where both of these proteins are expected to be found and haematoxylin localization was to the cytoplasm. Figure 6.2 (d), (e) and (f) show the segmentation of tissue immunohistochemistry slides for quantification by Halo, demonstrating the accuracy of the segmentation algorithm at detecting positive staining. For the HGSOC tissue samples, cellular density, defined as number of cells per unit slide area was 65.6 ± 28.8 (mean ± S.D.) x 10^3 cells/mm^2, the collagen IV positive tissue area was 15.8 ± 5.4% and the laminin positive tissue area was 20.9 ± 6.7%.

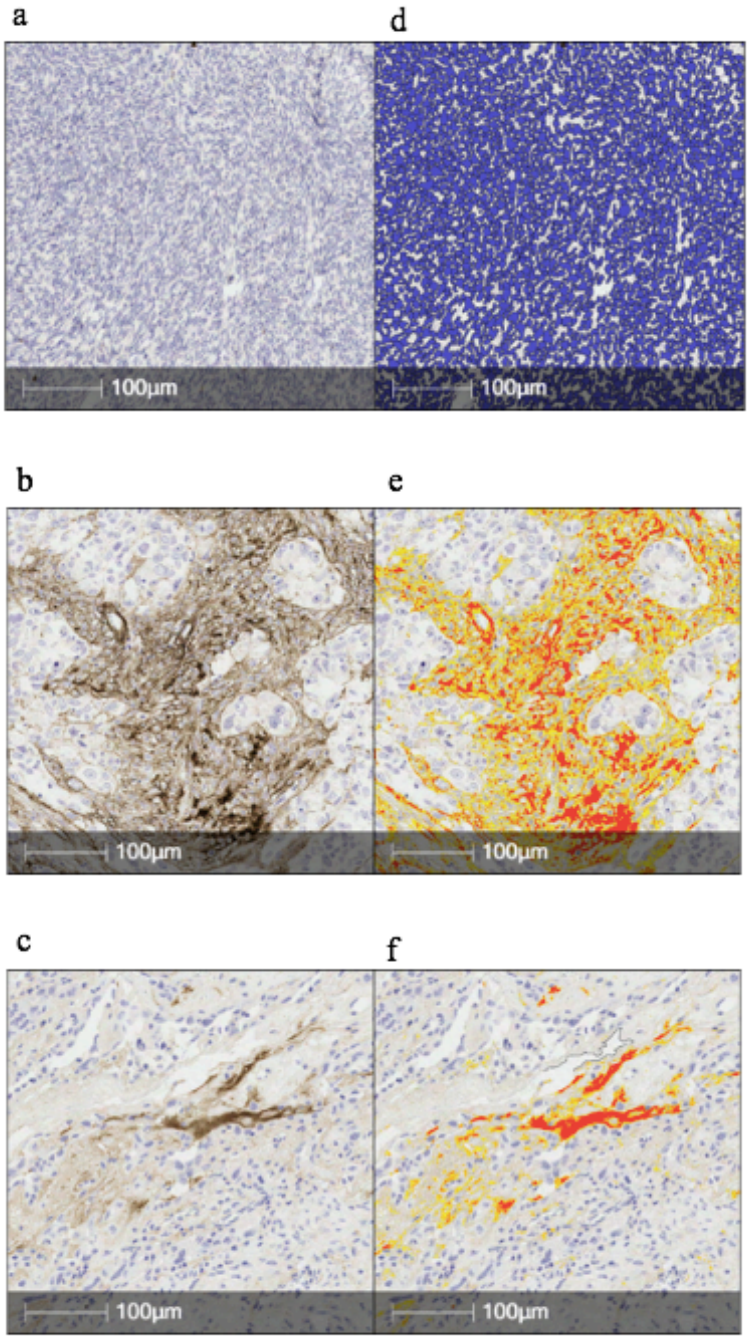

Figure 6.2: 20x magnification of high grade serous ovarian cancer immunohistochemistry from a 63-year old study participant; (a) haematoxylin stain, (b) collagen IV stain, brown = positive tissue, blue = negative tissue, (c) laminin stain, brown = positive tissue, blue = negative tissue, (d) segmentation of haematoxylin stain for cell density measurement, (e) segmentation of collagen IV stain for area quantification. Yellow colour represents staining with optical density (OD) 0.270 to < 0.355. Red colour represents staining with OD >= 0.355. (f) segmentation of laminin stain for area quantification. Yellow color represents staining with optical density (OD) 0.270 to < 0.355. Red colour represents staining with OD >= 0.355.

There was a weak but statistically significant correlation between mean MTR and cell density, r = 0.48, *P* = 0.049. MTR correlated negatively with both collagen IV and laminin, r = -0.56, *P* = 0.02 and r = -0.61, *P* = 0.01 respectively. Tumour cell density did not correlate with collagen or laminin levels, r = -0.48, *P* = 0.053 and r = -0.34, *P* = 0.18. Collagen IV and laminin however correlated with each other, r = 0.61, *P* = 0.01. Figure 6.3 shows scatterplots of the correlations between: (A) cell density and MTR, (B) collagen IV and MTR, (C) laminin and MTR, (D) collagen IV and cell density, (E) laminin and cell density, (F) collagen IV and laminin.

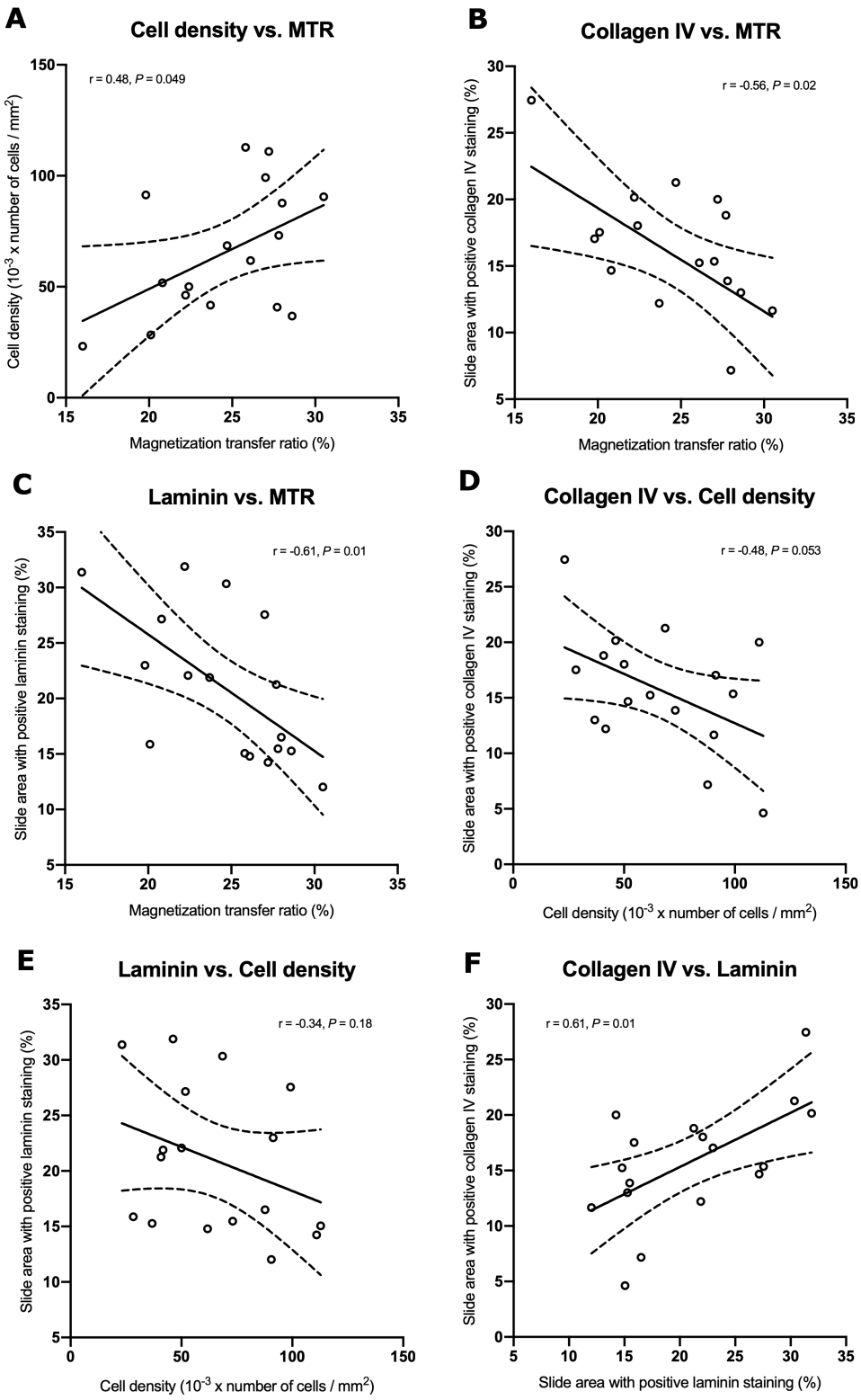

Figure 6.3: Plots of (A) tumour cell density vs. tumour MTR, (B) percentage of collagen IV tissue area vs. tumour MTR, (C) percentage of laminin tissue area vs. tumour MTR, (D) percentage of collagen IV tissue area vs. tumour cell density, (E) percentage of laminin tissue area vs. tumour cell density, (F) percentage of collagen IV tissue area vs. percentage of laminin tissue area.

6.4 Discussion

In this study, MTR was found to have a weak positive correlation with tumour cell density and negative correlations with the levels of the BM proteins, collagen IV and laminin in HGSOC. Tumour cell density did not correlate with collagen IV or laminin, indicating that cell density and BM integrity may be independently related to MTR. Collagen IV and laminin levels also correlated with each other, which was expected as they are both markers of BM integrity.

The higher MTR of tumours with higher cell density may signify that there is a greater abundance of cellular macromolecules binding water and generating MTR signal in more cellular tumours. This suggests that intracellular macromolecules, rather than extracellular macromolecules, are playing a dominant role in generating the MTR signal in ovarian cancer. This is further supported by the fact that there was a negative correlation with the major macromolecular components of the BM and MTR.

MTR as a non-invasive measure of tumour cell density and intracellular macromolecular concentration could be a useful biomarker for stratifying tumours, identifying aggressive disease and treatment response monitoring. It could be complementary to other methods to image cellularity such as DWI. The data presented here also suggests that future MTR studies in other organs should consider the influence of cellular density on the results obtained and that the MTR may not simply be a function of extracellular protein concentration but may also be influenced by other biological and physical factors.

The inverse relationship found between MTR and collagen IV/laminin in the BM could reflect the breakdown of the BM by invasive cancers that are growing, replicating and producing more cells. The results of this study suggest that as macromolecules that bind water (either intracellular or extracellular or both) increase in tissue, the BM is broken down. The increase in macromolecules with BM membrane breakdown also appears larger than can be accounted for by an increase in cell density alone as the relationship of BM protein loss to MTR is stronger than the relationship of tumour cell density to MTR. These additional macromolecules may be extracellular molecules from new ECM structures or secreted peptides.

The measurement of BM integrity through MTR could potentially provide early information on changes to the tumour microenvironment and stroma that may be of prognostic and therapeutic significance in HGSOC. BM breakdown could indicate early metastatic processes and therefore give an indication of patient prognosis. The limitations of this study include the time delay between tissue sampling and imaging, during which cell density changes, BM changes and cancer progression could have occurred. Multiple hypothesis testing was also performed which if corrected for using the Bonferonni correction would cause the loss of all statistically significant ($P < 0.05$) correlations detected here. In addition the repeatability of MT imaging for ovarian cancer has not yet been shown in any published work that it has been possible to find. The repeatability of MT imaging however has been shown for other tissue such as in healthy breast (176) and brain (177). A study on the repeatability of MT imaging in ovarian cancer performed in the future could be used to help interpret the results found here.

In conclusion, this work shows that MTR measurements in HGSOC may correlate positively with tumour cell density, and inversely with collagen IV levels and laminin levels. MT imaging could therefore be of clinical use in oncological imaging to measure cellularity and to detect the breakdown of the BM. These findings have the potential to be applied in predicting invasion and metastases in HGSOC lesions. Further work is now needed with larger patient samples to verify these results and to explore the longer-term relationship of MTR with HGSOC including the association with outcome, relapse, survival and distant cancer spread in patients.

Chapter 7

Hyperpolarized carbon-13 magnetic resonance imaging in cancer

---

7.1 Cancer metabolism

As healthy cells undergo the malignant transformation into cancer there is a change in the way they metabolise glucose. Pyruvate is generated from glucose in normal tissue by glycolysis and this process of glycolysis is increased in most cancers: tumours have increased glucose uptake compared to normal cells (178). Glycolysis is an irreversible chemical process involving ten enzyme-catalyzed reactions. The overall reaction is:

$$C_6H_{12}O_6 + 2[NAD]^+ + 2[ADP] + 2[P]_I \longrightarrow 2CH_3COCOOH + 2H^+ + 2[NADH] + 2[ATP]$$

After glycolysis, the pyruvate produced from glucose can enter one of three major metabolic pathways that can be imaged with hyperpolarized carbon-13 MRI (HP ^{13}C-MRI).

In healthy normoxic cells the majority of pyruvate is converted by the pyruvate dehydrogenase enzyme complex (PDH) into acetyl-CoA which joins the tricarboxylic acid (TCA) cycle where it is used primarily for the manufacture of carbon dioxide, water, ATP, GTP and NADH. The NADH produced from the TCA is further metabolised in the electron transport chain (ETC) within mitochondria to produce more ATP and carbon dioxide. Some of the carbon dioxide produced in the TCA cycle and ECT dissolves in tissue water to produce ionic bicarbonate. This bicarbonate if produced by the tissue in large enough concentrations can be imaged and quantified with HP ^{13}C-MRI. The Henderson-Hasselbach equation can be applied to tissue bicarbonate quantification using HP ^{13}C-MRI to create maps of tissue pH.

In cancer cells compared to healthy cells, larger amounts of the pyruvate from glycolysis are converted by the lactate dehydrogenase (LDH) enzyme into lactate. The reaction catalysed by LDH is reversible and uses NADH or NAD^+ as a cofactor, depending on the direction in which it flows. The reaction is:

$$\text{pyruvate} + \text{NADH} \longleftrightarrow \text{L-lactate} + NAD^+$$

In healthy cells the diversion of pyruvate metabolism towards lactate production usually occurs only when there is a shortage of oxygen because of impairment of oxidative phosphorylation in hypoxic tissue. Cancer cells however generate large amounts of lactate even in the presence of oxygen, termed aerobic glycolysis or the Warburg effect, which is partly driven by the anabolic demands of the rapid cellular proliferation that they undergo (179) and by overexpression of LDH.

Lactate levels build up within cancers (180) and this lactate is preferentially diverted towards cell growth and proliferation rather further metabolic breakdown to produce energy via molecules like ATP and NADH (181). Lactic acid production in cancer may also aid tumour invasion through acidification of the extracellular environment, which helps to break down and remodel extracellular matrix structures that would otherwise impair tumour growth. Lactate levels in tumours have a strong correlation with aggressiveness, metastatic potential and overall prognosis (182-184). HP ^{13}C-MRI can measure lactate and LDH activity in tissue which can aid diagnosis of cancers and can be used for monitoring changes in cancer metabolic activity over time such as in response to treatment.

The third major pathway of pyruvate metabolism that can be studied with HP ^{13}C-MRI is the conversion of pyruvate to the amino acid alanine, catalyzed by the enzyme alanine transaminase (ALT). ALT activity is highest in hepatocytes and muscle cells.

HP ^{13}C-MRI of pyruvate labelled in the first carbon position can be used to image injected pyruvate and the lactate, bicarbonate and alanine produced from this pyruvate. The lactate measurement can investigate the extent of the metabolic shift of pyruvate metabolism in cancers towards lactate production. The biochemical changes that occur in tissue with malignant transformation are also likely to occur earlier than the structural changes that are detected by other forms of imaging such as CT or proton MRI. HP ^{13}C-MRI may therefore offer an earlier and more sensitive means of identifying cancer formation. In addition,

biochemical changes occur more rapidly following successful response to therapy than conventionally imaged anatomical changes. The major metabolic pathways relevant to HP ^{13}C-MRI of pyruvate metabolism are summarized in Figure 7.1 below.

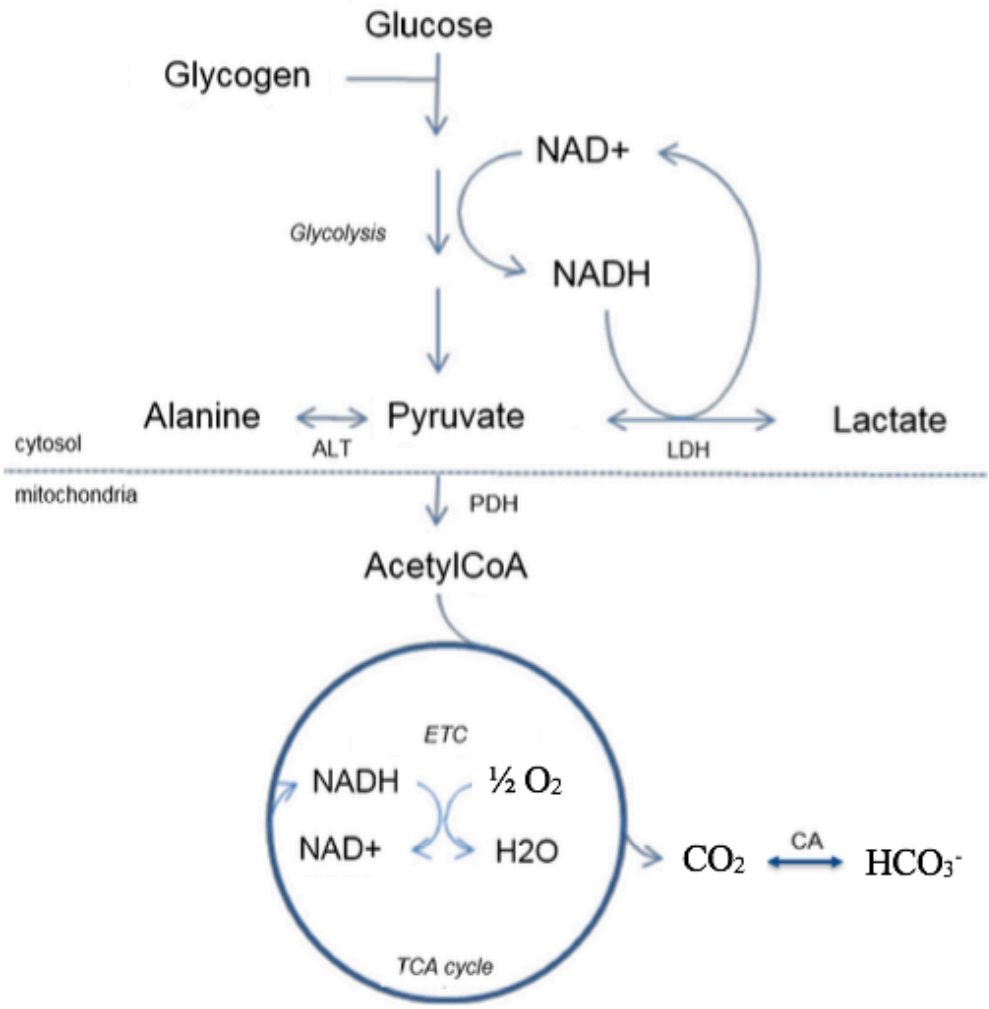

Figure 7.1: Schematic representation of the metabolism of pyruvate.

7.2 Biological factors that can affect the HP ^{13}C-MRI signal

There are a number of biological factors that may contribute to the overall HP ^{13}C-MRI signal in pyruvate and lactate imaging. Tumor vascularity and perfusion for example could affect the delivery of pyruvate to the tissue, as HP ^{13}C-pyruvate is injected into a peripheral vein during imaging and must be transported through the circulatory system to the tumour

location. Tumour activity of the enzyme LDH may then influence the rate of conversion of pyruvate into lactate. Transport of pyruvate into the cell is also likely to be a determinant of metabolism into lactate as LDH is a cytoplasmic enzyme. The transmembrane transporter for pyruvate is the monocarboxylate transporter (MCT) and expression of MCT by cancer cells may thus also influence the HP ^{13}C-MRI signal.

7.3 Lactate dehydrogenase in cancer

LDH activity and expression is higher in most types of cancerous tissue. The increase in LDH activity facilitates more rapid exchange between pyruvate and lactate (185-187). In healthy tissue LDH normally experiences negative feedback from the reaction it catalyzes so that increased levels of lactate and an acidic environment inhibit the production of more lactate. In cancer however, the high expression of LDH along with the switching off of other key regulatory mechanisms overcomes this feedback inhibition and lactate levels can increase to very high amounts (180).

The LDH enzyme is comprised of 4 subunits. Each of these subunits is one of two types: M (muscle) or H (heart). LDH-M and LDH-H are also called LDH-A and LDH-B respectively. The subunits of LDH combine into the four-unit LDH enzyme in different ways to produce five main isoforms (188). These isoforms each predominate in different types of tissue and it is the LDH-A subunit of LDH that is overexpressed in cancers (185, 186, 189, 190), including HGSOC. Table 7.1 below lists the LDH isoforms and the tissues in which they are primarily found.

LDH isoform	Subunits	Distribution
LDH-1	4H + 0M	Heart, red blood cells and brain
LDH-2	3H + 1M	White blood cells and the reticuloendothelial system
LDH-3	2H + 2M	Lungs
LDH-4	1H + 3M	Kidney and pancreas
LDH-5	4M + 0H	Skeletal muscle and liver

Table 7.1: The main human LDH isoforms and their locations in the human body.

Although LDH is a cytoplasmic enzyme, serum levels may rise in certain forms of cancer where there is a leakage of intracellular contents into the extracellular space, for example from necrosis or where there is high tissue turnover such as in lymphomas. Serum LDH also increases when there is tissue damage or breakdown after chemotherapy treatment, and in conditions with cell lysis not related to cancer, including myocardial infarction, haemolytic states and after heavy exercise. A rise in serum LDH levels is sometimes used as a clinical biomarker in oncology along with electrolyte changes for tumour lysis syndrome.

7.4 Monocarboxylate transporter expression in cancer

The changes in metabolism that occur in cancer cells cause a high production of lactic acid in the intracellular space. Unless excreted or metabolised, lactic acid can build-up to such an extent that it could lower intracellular pH which could adversely affect the activity of enzymes that are sensitive to pH and the equilibrium of chemical reactions necessary for vital cellular processes. To prevent this happening, cancer cells have adapted to remove excess lactate by up-regulation of the expression of the monocarboxylate transporter (MCT). The efflux of lactate is essential to prevent a build-up of toxic levels inside cancer cells and the expression of MCT is believed to be higher in cancer partly for this reason (191).

The MCT transmembrane protein can also transport pyruvate in addition to lactate across the cell membrane (192, 193) and the expression of MCT has previously been shown to be the rate limiting step in the conversion of extracellular pyruvate to lactate in breast cancer cells (194).

Each of the four subtypes of the MCT transporter 1-4 exhibits different kinetics and substrate specificity. All MCT transporters facilitate the proton-linked movement of monocarboxylates such as L-lactate, pyruvate and ketone bodies in both directions across the plasma membrane. MCT1 is distributed widely across many different types of tissues and is best adapted for the transport of lactate into cells. MCT4 is more common in white skeletal muscle and works best at lactate export from cells. Both MCT1 and MCT4 are more prevalent in cancer.

7.5 Clinical hyperpolarized carbon-13 cancer imaging

Pyruvate is transported rapidly into cancer cells because of MCT upregulation and is used more avidly by cancer cells because of changes in metabolism due to increased LDH levels and the Warburg effect. During the development of hyperpolarized imaging, ^{13}C-labelled pyruvate emerged as the leading candidate molecule for cancer imaging (195, 196). The fast rate of production of lactate from pyruvate by high LDH activity in tumours and physical properties of the pyruvate molecule which help it to retain polarization during the lifetime of an *in vivo* experiment allow for sufficient hyperpolarized ^{13}C-lactate signal to be retained upon injection of ^{13}C-pyruvate to permit imaging before the hyperpolarized state decays.

Genetic risk factors for ovarian cancer are of special interest in hyperpolarized imaging. This is because it is known that certain mutations affect the biochemistry of cancer cells through changes in the expression of proteins that influence key chemical reactions of metabolism such as those in the TCA cycle and electron transport chain (197-200). Proteins that are upregulated in cancer include the transporters (201, 202) and enzymes (185, 203) that transport and catalyze pyruvate and lactate. Comparing the presence of common mutations with hyperpolarized ^{13}C-MRI could therefore potentially uncover correlations between the genetic composition of cancer tissue and imaging.

Key proof-of-principle studies carried out at Cambridge have demonstrated that hyperpolarized ^{13}C-pyruvate, hyperpolarized ^{13}C-lactate and their exchange could be imaged *in vivo* in murine models and that early tumour biochemical responses to chemotherapy drugs could be detected in mice with implanted lymphomas (204). Hyperpolarized imaging is capable of detecting tumours and the changes that occur to the metabolism of pyruvate in some animal cancers as early as 24 hours after chemotherapy treatment (205).

The first human trial to use hyperpolarized ^{13}C-pyruvate was completed in 2013 by a group at the University of California San Francisco (UCSF) with a prototype clinical hyperpolarizer device. This group successfully imaged the metabolism of pyruvate in patients with prostate cancer. Areas with lactate accumulation were detected on hyperpolarized imaging that were not visible with proton MRI and some of these areas were shown by biopsy to contain tumour (206). These results provided initial evidence that hyperpolarized imaging could be more sensitive at detecting human cancers than traditional proton MRI. One of the next

steps in clinical hyperpolarised imaging with carbon-13 is to apply the technique to a disease where current detection and screening methods are inadequate such as ovarian cancer so that the imaging can be used to help improve patient outcomes.

Higher grades of cancer are related to higher hyperpolarized lactate signal (207). HGSOC may therefore produce a larger and more easily detectable hyperpolarized ^{13}C imaging signal than other cancers, that can be used to more accurately model enzyme kinetics. High grade serous ovarian malignancies also respond differently to chemotherapy in different patients (208) and no reliable method currently exists for detecting a response before several weeks of treatment have passed HP ^{13}C-MRI could help address these clinical problems in HGSOC.

The procedure involved in clinical carbon-13 hyperpolarization has been refined since its inception and General Electric (GE) Healthcare have developed commercial equipment termed SPINlab® to more efficiently carry out the process in a routine radiology enviroment. The SPINlab® includes quality control checks to ensure the safety of samples for human use and performs automated dissolution into an injectable form.

A special sterile fluid path has been designed by GE Healthcare for use with the SPINLab®. The path is a single use, disposable unit and contains multiple components required to hyperpolarize a sample for human. The path must be assembled and filled in a sterile environment such as in a pharmacy facility under a laminar flow hood. The sample vial contains a mixture of the ^{13}C molecule to be hyperpolarized and EPA (electron paramagnetic agent or radical). After filling the sample vial is sealed with a laser welder and the setup is placed in the SPINLab® for hyperpolarization. A picture of the GE Healthcare SPINlab at Cambridge is shown below in Figure 7.2 (a) and a picture of a clinical fluid path is shown in Figure 7.2 (b). A dedicated pharmacy unit was also built at Addenbrooke's Hospital in Cambridge to assemble clinical fluid paths.

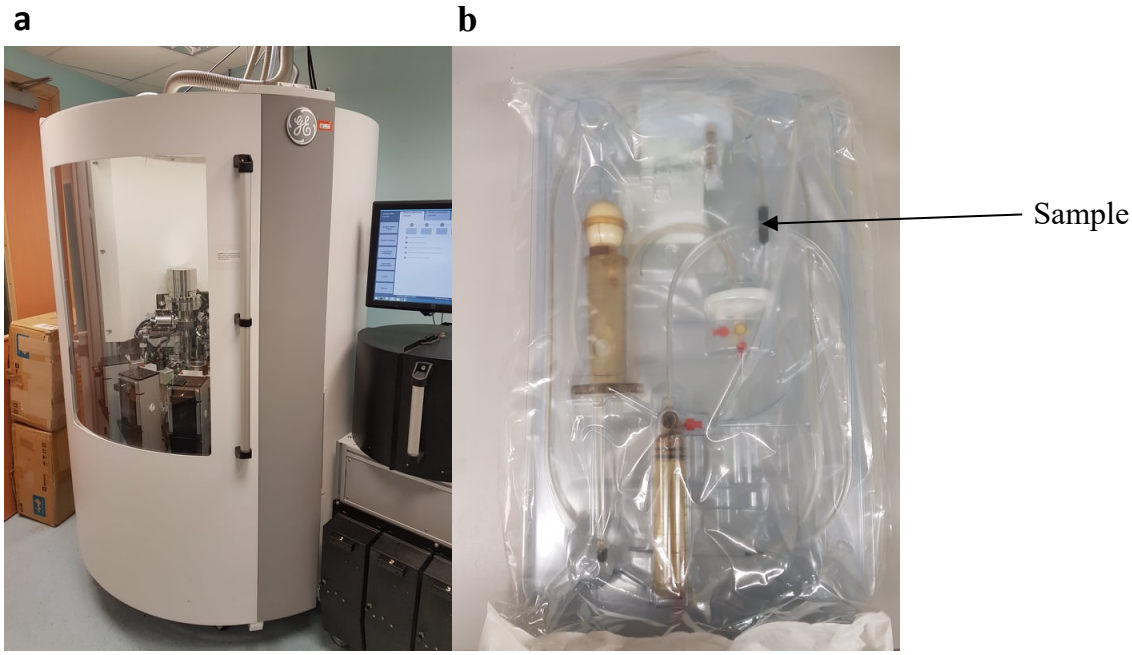

Figure 7.2: (a) GE Healthcare SPINlab, (b) sterile clinical fluid path

The time available for imaging an injected hyperpolarized ^{13}C molecule is limited because the half-life of the hyperpolarized state once dissolution has occurred is around 60 seconds and sufficient signal for imaging is only present for around 5 half-lives. During this short timeframe in addition to completing the imaging acquisition, the dissoluted solution must be transferred to the patient, injected into a peripheral vein, be transported by the circulatory system of the patient to the area being imaged and undergo metabolism in that tissue. In its current form hyperpolarized ^{13}C-MRI is therefore only suited to imaging rapid chemical reactions. Reproducibility and repeatability of the technique in a clinical setting has not yet been demonstrated and because there is a lack of understanding of the underlying biological mechanism of signal generation, the interpretation of imaging results is also difficult. Current research is therefore still concentrated around proof-of-principle of the hyperpolarized ^{13}C-MRI for humans in a clinical setting.

Hyperpolarised ^{13}C-MRI is thought to have the potential to detect changes in cancer earlier than more conventional forms of proton MRI used in clinical practice that image tumour structure, as biochemical changes in the transformation of healthy tissue into cancer and in the response of cancer to treatment occur earlier than structural alterations such as tumour

size that might be measured by criteria like RECIST on CT or MRI (209-213). Despite its clinical potential the quantification of pyruvate and its metabolites in tissue using hyperpolarised ^{13}C-MRI is challenging due to the low concentrations of these metabolites, the larger number of biological covariates that can affect imaging signal and the difficlty of validation with tissue measurements due to the complexity of halting chemical reactions in biological systems for ex-vivo metabolite measurement.

7.6 Imaging sequences, kinetic modelling and repeatability

For clinical imaging, an IDEAL spiral or an echo planar imaging (EPI) pulse sequence may be used to rapidly image hyperpolarized ^{13}C molecules. IDEAL uses spectral-spatial encoding based on single shot spiral encoding and was one of the first pulse sequences to be applied clinically for chemical shift imaging of hyperpolarized carbon-13 molecules. Both spiral imaging and EPI accelerate chemical shift imaging by performing spatial encoding between spectral sampling (214). A simplified depiction of the difference in *k*-space filling between a spiral acquisition and the more conventional EPI is shown in Figure 7.3 below. IDEAL has the advantage over EPI that it more uniformly samples data and provides less of a strain of hardware to produce gradients that rapidly switch in direction for the filling of *k*-space. One disadvantage of IDEAL is that is slightly slower than EPI and as spiral sequences are less frequently used than EPI, software that uses the IDEAL spiral is not as readily available, or easy to produce and implement at sites with low levels of physics support (215).

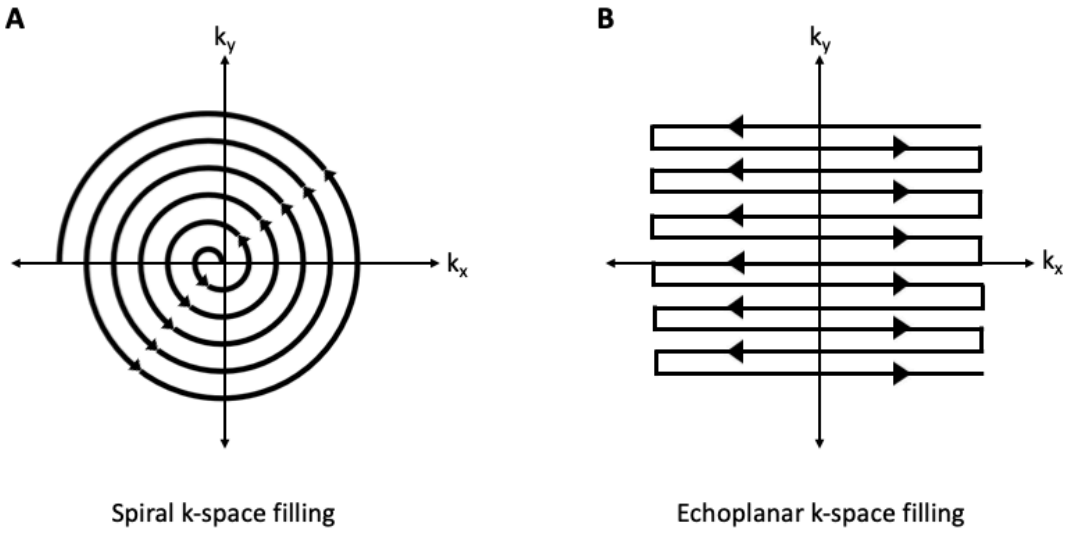

Figure 7.3: *k*-space filling using (A) spiral trajectory, (B) echo planar imaging.

Pyruvate-lactate exchange in HP ^{13}C-MRI may be modelled by fitting kinetic parameters to two-site exchange models or more simply with measurement of area under the curve (AUC) of the pyruvate-to-lactate ratio. Two-site exchange models assumes that the backward flux of lactate into pyruvate is zero and may be sensitive to the initial value of parameters in the model (216) and AUC models have the advantage of being independent of the shape of pyruvate inflow (217). Until there is a better understanding of the biological origin of the HP ^{13}C-MRI signal and larger human datasets however it will be difficult to determine which type of modelling is best for clinical use as the kinetics in the much larger human biological system is unlikely to be accurately represented by comparison studies performed on small animal models.

At the time of writing this thesis there have been no published results on the repeatability or reproducibility of hyperpolarized carbon-13 MRI in humans using a clinical hyperpolarizer and a clinical imaging set-up. In preclinical experiments on mice implanted with lymphoma, the repeatability of hyperpolarized ^{13}C-lactate to hyperpolarized ^{13}C-pyruvate ratio calculated using fitting to the modified Bloch equation for two-site exchange no significant difference in the hyperpolarized ^{13}C-lactate to hyperpolarized ^{13}C-pyruvate ratio with repeat imaging was found (218).

Chapter 8

Changes to ovarian cancer lactate dehydrogenase enzyme activity in response to treatment

---

8.1 Introduction

In vitro tissue culture experiments are a valuable method for studying cancer by providing an opportunity to assess the effect of interventions on a genetically and phenotypically similar cell population, compared to *in vivo* experiments which include a mixture of cancer, stroma and other cell types and tissue structures.

There are several well-established lines of ovarian cancer cells. Those commonly used to model ovarian cancer include OV, OVCAR and PEO. The suitability of a cell line for modelling the HGSOC subtype of ovarian cancer can be quantified by measuring properties such as the fraction of altered genome and the presence of gene changes that are specific to HGSOC. Such calculations have shown that OV is a poor representative of HGSOC while PEO and OVCAR are among the best (219).

Animal experiments have shown that there is a decrease in the exchange between pyruvate and lactate in cancers after treatment (12, 212). Anticancer treatments target cancerous cells and reduce the proportion of cells in a tumour with high LDH activity. The detection of treatment response with HP ^{13}C-MRI however has never been shown to be possible for ovarian cancer either pre-clinically or in a human. In ovarian cancer there are new drug treatments currently being introduced clinically that may have a greater effect on LDH activity than traditional cancer treatments. Some ovarian cancers also carry the *BRCA* mutation which may further affect LDH activity. In this experiment the effect of different anti-cancer treatments on LDH expression in the PEO4 cell line was investigated.

8.2 PARP inhibitors in ovarian cancer

PARP (Poly ADP-ribose polymerase) inhibitors are a class of ovarian anti-cancer drug that are of interest for hyperpolarized ^{13}C imaging. PARP is an enzyme involved in the repair of single stranded DNA breaks. In cancer there is a higher rate of DNA replication errors and activity of PARP is important for repairing these errors. PARP activation leads to the cytosolic depletion of NAD^+, as NAD^+ is consumed to generate ADP-ribose monomers for the DNA repair process by base excision repair. NAD^+ depletion causes NADH loss, as NADH is converted to NAD^+ in response to low NAD^+ levels. Significant PARP activation leads to cell death and glycolytic inhibition due to lack of NAD^+/NADH and it has been shown that this cell death can be prevented when exogenous NAD^+ is added to PARP (220, 221). In preclinical experiments on mouse lymphoma cells the chemotherapy drug etoposide was shown to deplete the NADH pool and reduce pyruvate-lactate exchange as measured with dynamic hyperpolarized carbon-13 magnetic resonance spectra. In the same set of experiments, it was demonstrated that the administration of the PARP inhibitor nicotinamide inhibited the etoposide induced NADH depletion. Nicotinamide along with another PARP inhibitor, 3-amino-benzamide, have also both been shown to inhibit etoposide-induced loss of pyruvate-lactate exchange (204). Neither of these drugs are clinically used PARP inhibitors however.

PARP inhibitors (PARPi) cause cancer death by blocking the PARP enzyme from repairing DNA, leading to the accumulation and buildup of DNA damage to fatal levels in cancer cells. PARP inhibitors also lessen the depletion of NAD^+/NADH in cancer tissue that would otherwise occur with PARP activation. When PARP inhibitors are used, there is more NAD^+/NADH available in cancers to act as a co-factor in other chemical reactions such as the LDH catalyzed redox reaction that interconverts pyruvate and lactate. It was therefore hypothesized in this study that HP ^{13}C-MRI may be able to image the biochemical effect of PARPi on cancer cells.

PARP inhibitors are most effective for the treatment of ovarian cancers with BRCA mutations and their efficacy is being explored in on-going clinical trials (222, 223). Cancers with the BRCA mutation are unable to perform homologous recombination to repair double stranded DNA damage. When BRCA mutant cancers have the PARP enzyme inhibited they

are also unable to repair single stranded DNA breaks. The inability to repair single stranded DNA breaks provides the opportunity for the single breaks to progress into double stranded breaks which BRCA-mutant cells are unable to repair. Double stranded DNA breaks contribute to the threshold of fatal DNA errors that are required for cell death. A schematic showing the action of PARP and PARPi is shown below in Figure 8.1.

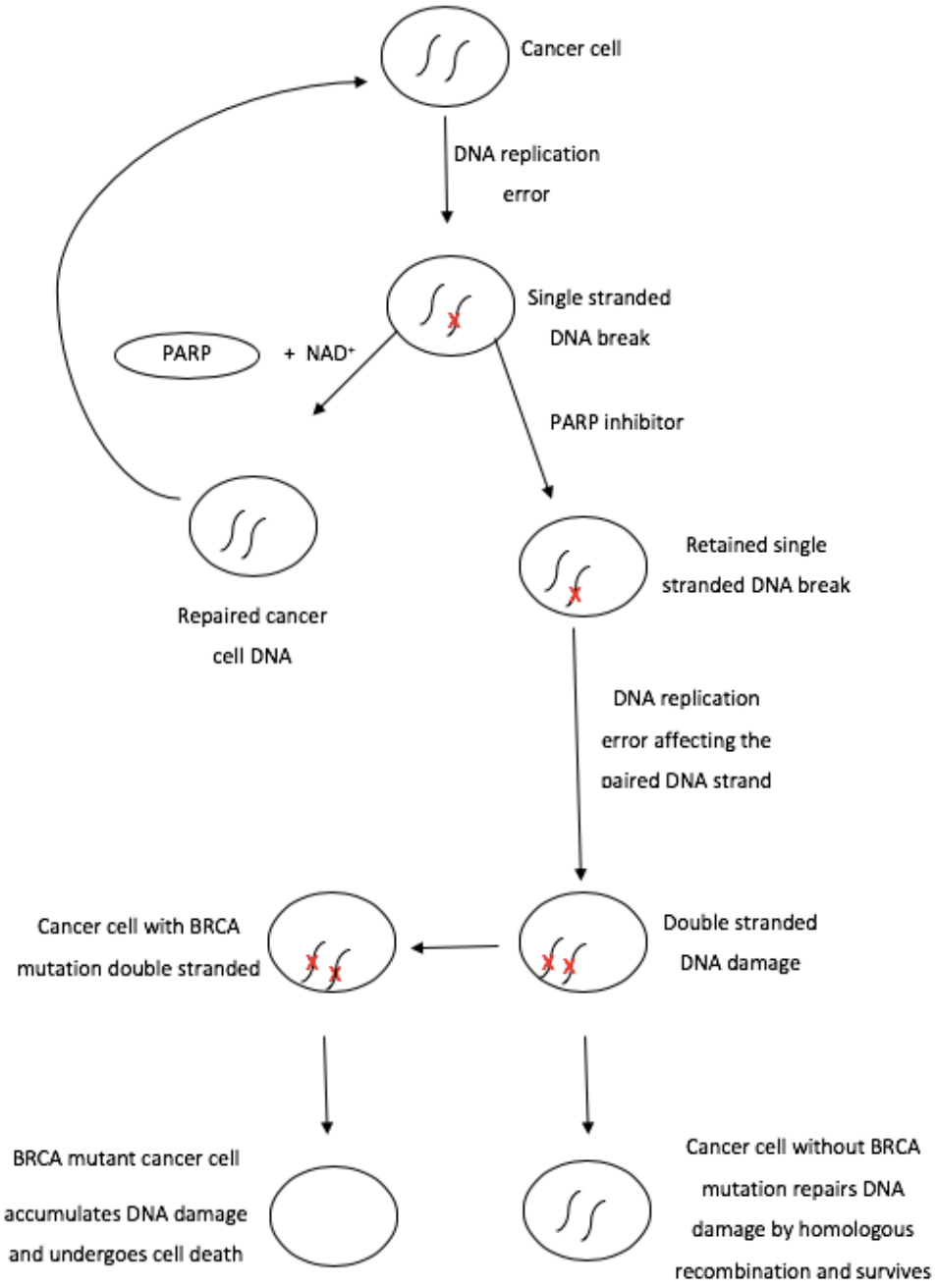

Figure 8.1: Schematic showing the role of PARP and PARP inhibitor function in cancer cells

The use of PARP inhibitors is being studied in many tumours. Significant tumour responses and clinical benefit have been demonstrated with the PARP inhibitor olaparib in phase 1 trials (223). Olaparib given to patients with recurrent disease, after platinum-based treatment resulted in an improvement in progression-free-survival (PFS), and few toxic effects after prolonged administration (224).

BRCA1 and BRCA2 are mutated in 6% and 9% of HGSOC cell lines respectively (225). Similar to PARP, BRCA uses NAD^+/NADH in DNA repair. The depletion of NAD^+/NADH with BRCA activity is not as extreme as with PARP activity. It is possible however that if HP ^{13}C-MRI can detect the NAD^+/NADH caused by PARP then it may be able to detect similar changes related to BRCA.

To investigate whether HP ^{13}C-MRI could image the effect of PARP inhibitors in ovarian cancer, cell experiments were performed where ovarian cancer cells were treated with olaparib and LDH activity was measured. The long-term goal was to understand the metabolic changes that occur in ovarian cancer following treatment including PARPi and how this can be applied to human imaging in the future.

8.3 Cell experiment: Methods and materials

Cell Growth and Treatment

The PEO1 cell line was selected for this experiment because the BRCA1 mutation is universally present in PEO1 cells making this cell line responsive to PARP inhibitors. PEO1 is an adherent cell line. It was derived in 1988 from the malignant peritoneal effusion of a patient with ascites from a poorly differentiated serous adenocarcinoma of the ovaries. The patient the cells were extracted from had received treatment with cisplatin, 5-fluorouracil and chlorambucil before the cell extraction (226). PEO1 cells are very sensitive to oestrogen and the line has been used for many years in ovarian cancer research as a model to investigate the action of oestrogen on ovarian tumour cells.

The PEO1 cells used in this study were obtained from frozen storage at -80 °C at the Cancer Research UK, Cambridge Institute. They were defrosted and grown using DMEM (Dulbecco's Modified Eagle Medium) containing L-glutamine that was mixed with foetal calf bovine

serum and penicillin + streptomycin antibiotic. The cells were placed in an incubator at 37°C until there were four confluent T-160 cell culture flasks. At confluence the cells were counted and a viability check was carried out on a small aliquot with Trypan blue. Counting was performed manually using a haemocytometer and light microscope as well as by electronic cytometry. Each flask was found to contain between 17.9 and 18.2 million cells with an average viability of 93.9%. The cells were re-suspended in media and 50,000 cells placed into each of the wells of 16 six-well plates. The 16 plates were divided into 4 sets of 4 plates and each set was treated with different ovarian cancer chemotherapy drug to produce 4 sets of 24 identically treated wells. The four treatments were carboplatin, paclitaxel, olaparib and no chemotherapy. See Figure 8.2 for a schematic of the experimental design.

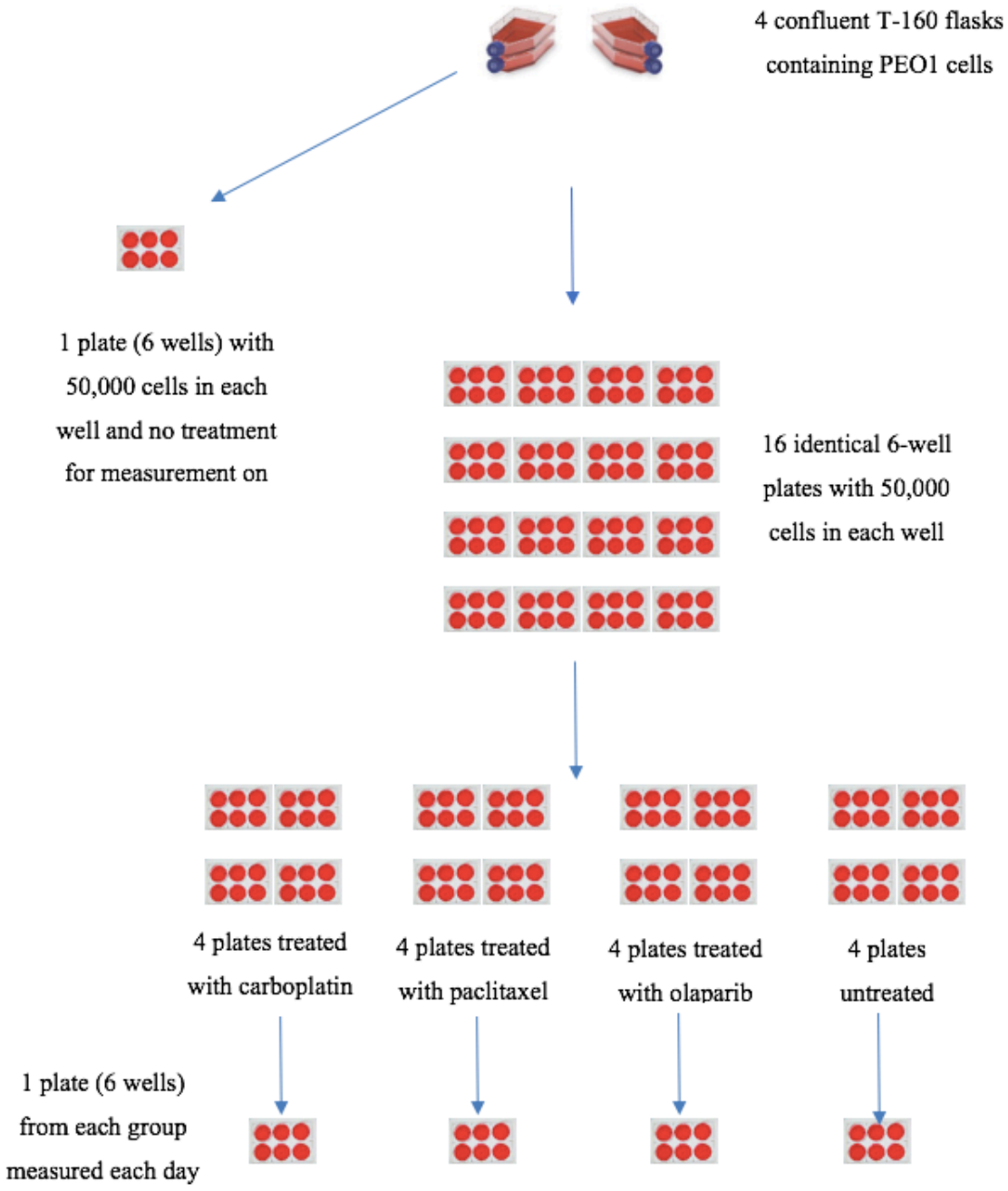

Figure 8.2: Schematic of ovarian cell experiment design.

Drugs were added in amounts that would result in a concentration in the wells equal to the inhibitory dose 50 (ID50) of each drug for PEO1 cells. Carboplatin was dissolved in distilled water and paclitaxel and olaparib were both dissolved in DMSO. The doses used were;

- ID50 Carboplatin for PEO1 = 4 µM
- ID50 Paclitaxel for PEO1 = 10 nM
- ID50 Olaparib for PEO1 = 5 µM

Drugs were obtained from the sources lister in Table 8.1 below.

Drug	**Manufacturer**	**Product Number**
Carboplatin	Sigma-Aldrich	C2538
Paclitaxel	Sigma-Aldrich	T1912
Olaparib	BioVision	1952-5

Table 8.1: Chemotherapy drugs used in cell experiments

The volume of drug containing solution added to the wells to produce the desired treatment concentration was very small in comparison to the volume of media already in the wells (4 ml). It was therefore assumed that the drug solutions did not significantly change the concentration of any other substances present in the wells. Volumes of drugs added to the wells are summarized in Table 8.2.

Volume of media in wells	4.00 mL
Volume of carboplatin solution added	0.355 µL
Volume of paclitaxel solution added	4.44 µL
Volume of olaparib solution added	2.22 µL

Table 8.2: Volumes of drug solution added to wells.

Measurements were made of the intracellular and extracellular lactate concentrations and LDH activities using 6 wells from each set of 24 every day for 4 days.

Lactate and LDH extraction

Extracellular lactate and LDH measurements were acquired using media taken from the wells. For each well, approximately 2 mL of media was removed using a pipette and placed in a 15 mL falcon tube. The samples were rapidly frozen in dry ice to stop any further chemical reactions and transferred to a -80°C freezer for storage.

To obtain intracellular samples, the cells were detached from the well with 1 mL of 0.25% trypsin. The trypsin was neutralised in 3 mL of media and the cells centrifuged in a 15 mL falcon tube at 1300 rpm for 4 minutes. The supernatant was discarded and the cell pellet lysed in 500 µL of ice cold LDH lysis buffer obtained from the Sigma-Aldrich LDH enzyme activity measurement kit (MAK066), according to manufacturer instructions. The resulting mixture was centrifuged at 3000 rpm for 15 min to remove the cell fragments and 350 µL of the supernatant was moved to a 15 mL falcon tube and rapidly frozen at -80°C.

Measurement of lactate and LDH

The frozen extracellular and intracellular samples were transported on dry ice to the CBAL (Core Biochemical Assay Laboratory) at Addenbrooke's hospital for measurement of lactate and LDH. CBAL uses spectrophotometry of NADH at 340 nm to calculate lactate. LDH levels are found through biochromatic measurement of the rate of NADH production at 340 nm and 700 nm. The specifications for the assays and equipment provided by CBAL are given below in Table 8.3 and Table 8.4.

Assay	**Lactate**
Reagent Manufacturer	Siemens Healthcare Diagnostics
Assay Description	Colorimetric assay using lactate dehydrogenase to catalyse the oxidation of lactate to pyruvate with the simultaneous reduction of NAD+ to yield NADH which absorbs at 340nm. Hydrazine is used to trap the pyruvate produced thus driving the reaction to completion. Lactate concentration is measured bichromatically as an end point at 340 and 383nm. The assay is automated on the Siemens Dimension® RxL analyser. The assay uses 4µl of sample.
Calibration	A series of BSA-based lyophilised assay calibrators are supplied by Siemens.
Units Of Measurement	mmol/L
Lower limit of detection	0.3 mmol/L (manufacturer's data)
Imprecision Data	Between batch imprecision; 3.2% at 3.2 mmol/L , 1.9% at 10.4 mmol/L, (manufacturers data).
Reference	Siemens Dimension Lactate kit insert, product DF16, issued 2015-01-03

Table 8.3: Lactate assay specifications

Assay	Lactate Dehydrogenase (LDH)
Reagent Manufacturer	Siemens Healthcare Diagnostics
Assay Description	Colorimetric assay using the substrate L-lactate buffered at a pH of 9.4 which is cleaved by lactate dehydrogenase in the presence of NAD^+ to yield pyruvate and NADH which absorbs at 340nm. LDH activity concentration is measured bichromatically as a rate reaction at 340 and 700nm. The method is standardized against the International Federation of Clinical Chemistry (IFCC) LDH primary reference method procedure at 37^{o}C adapted to the Dimension® clinical chemistry system. The assay is automated on the Siemens Dimension® RxL analyser. The assay uses 8µl of sample.
Calibration	A series of serum-based lyophilised assay calibrators are supplied by Siemens.
Units of Measurement	U/L
Lower limit of detection	6 U/L (manufacturer's data)
Imprecision Data	Between batch imprecision; 2.8% at 113U/L, 1.1% at 376U/L, (manufacturers data).
Reference	Siemens Dimension LDI kit insert, product DF54, issued 2012-11-07

Table 8.4. Lactate dehydrogenase enzyme assay specifications

8.4 Results

Cell Number

50,000 cells were used to seed each well so cell number started at 50,000 at Day 0 in all wells. The untreated wells went on to have the highest mean cell numbers at all subsequent time-points compared to the chemotherapy treated wells. Numbers in the carboplatin and olaparib wells went up with time and the numbers in the paclitaxel wells went down. Figure 8.3 depicts the pattern of cell growth.

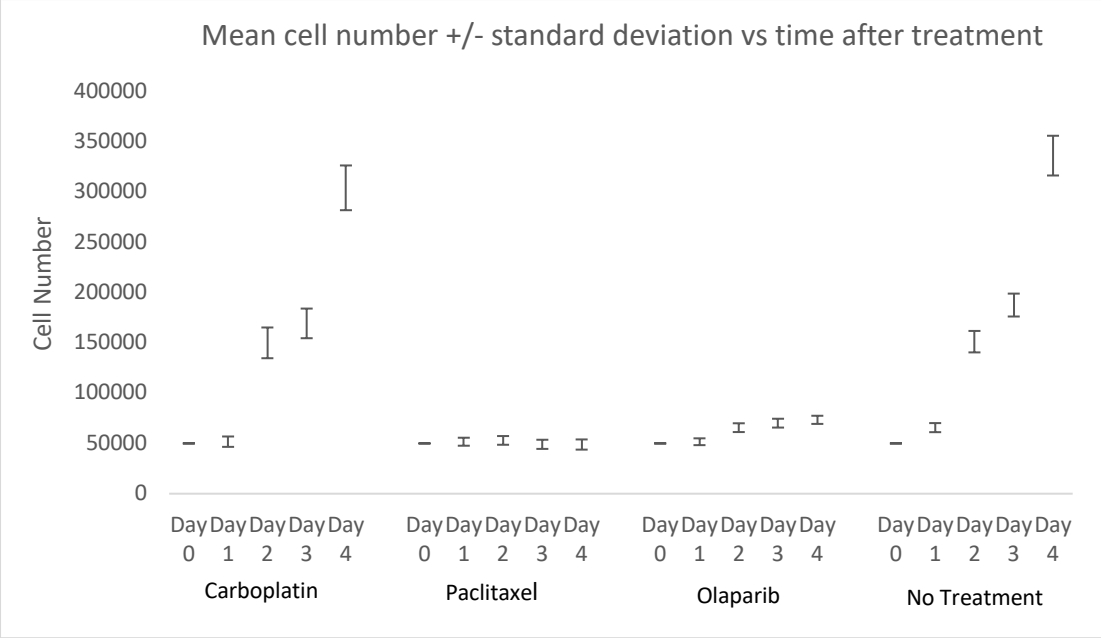

Figure 8.3: The mean number of cells in six wells +/- standard deviation vs. time in days after treatment

Total extracellular lactate

Extracellular lactate was measured as a surrogate of overall metabolic activity as lactate is a waste product of normal metabolism. The lactate rose with time in all treatment groups and at the end of 4 days, the olaparib group had the highest extracellular lactate levels even greater than the control cells. Figure 8.4 shows the mean extracellular lactate at each timepoint in each group.

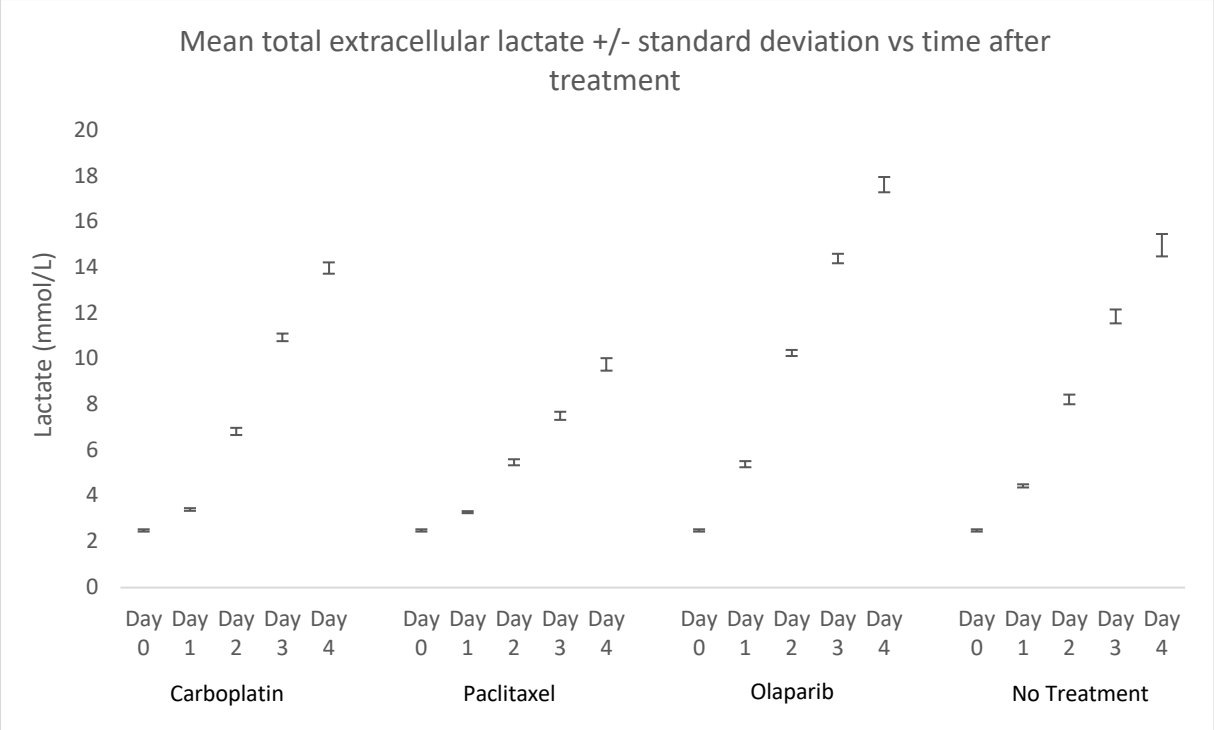

Figure 8.4. Plot of the mean extracellular lactate levels against time after treatment

Total extracellular lactate per cell

Given that lactate levels are a function of cell number in addition to their relationship with metabolic activity, the extracellular lactate levels were corrected for cell number, this is shown in Figure 8.5. In the carboplatin and control groups, extracellular lactate levels were stable suggesting that lactate may be a function of cell number in the presence of no treatment or of treatments which did not alter cell number significantly.

Other factors besides cell number which may be influencing extracellular lactate values in these groups include cell death or a change in LDH activity due to drug action.

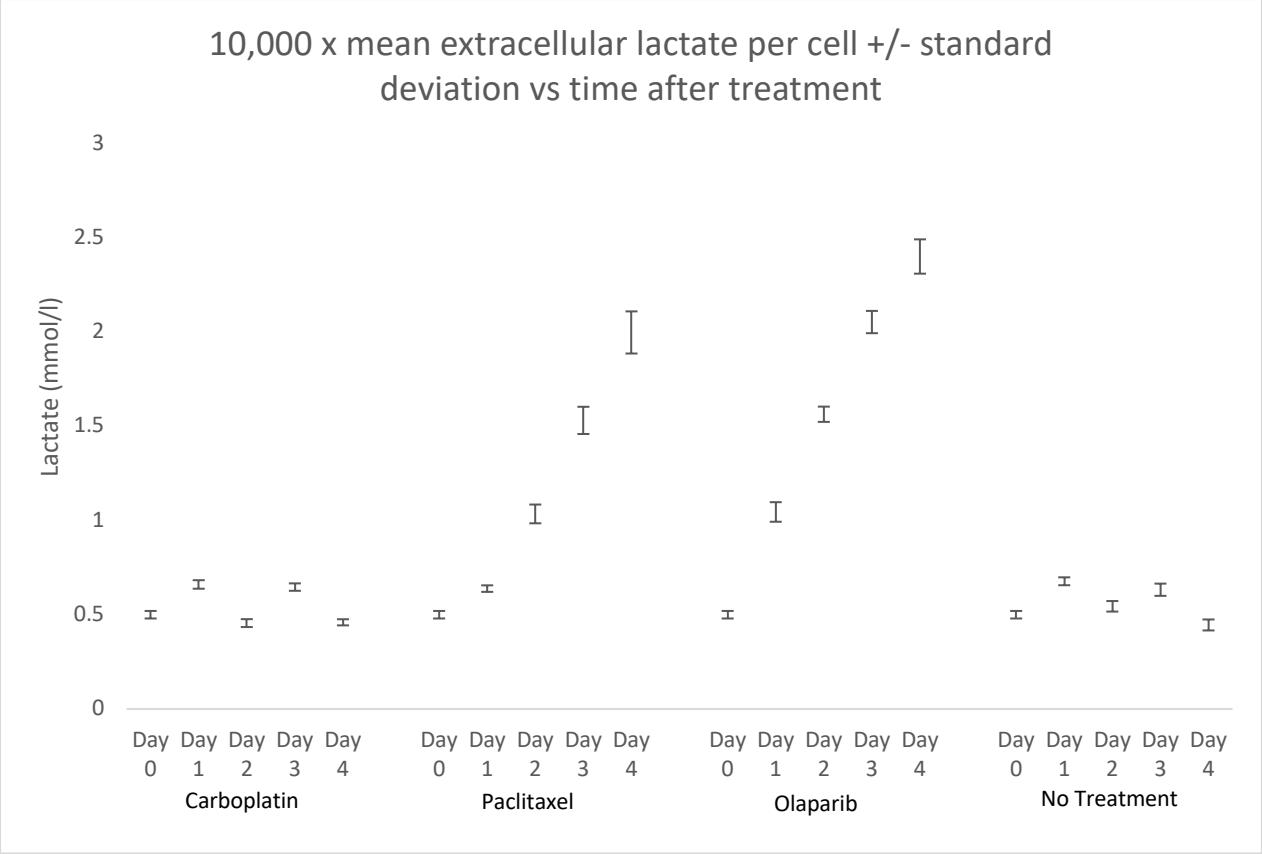

Figure 8.5: Extracellular lactate levels per cell vs time after treatment.

Intracellular LDH

Mean intracellular LDH activities corrected for cell number are shown in Figure 8.6. The olaparib group was the only group to show a consistent rise in LDH over time (Student's t-test, $P < 0.0001$ for a difference between day 0 and day 4). The LDH activity rose in the olaparib to much higher levels than in the other treatment groups or the control group by Days 3 and 4 (Student's t-test for Day 3: olaparib vs. carboplatin, $P = 0.0002$. Day 3: olaparib vs. paclitaxel, $P = 0.0025$. Day 4: olaparib vs. carboplatin, $P = 0.0008$. Day 4: olaparib vs. paclitaxel, $P < 0.0001$). LDH activity measurements were also made from the supernatant of these cell lines but these measurements did not show any significant changes over time with different chemotherapy drugs.

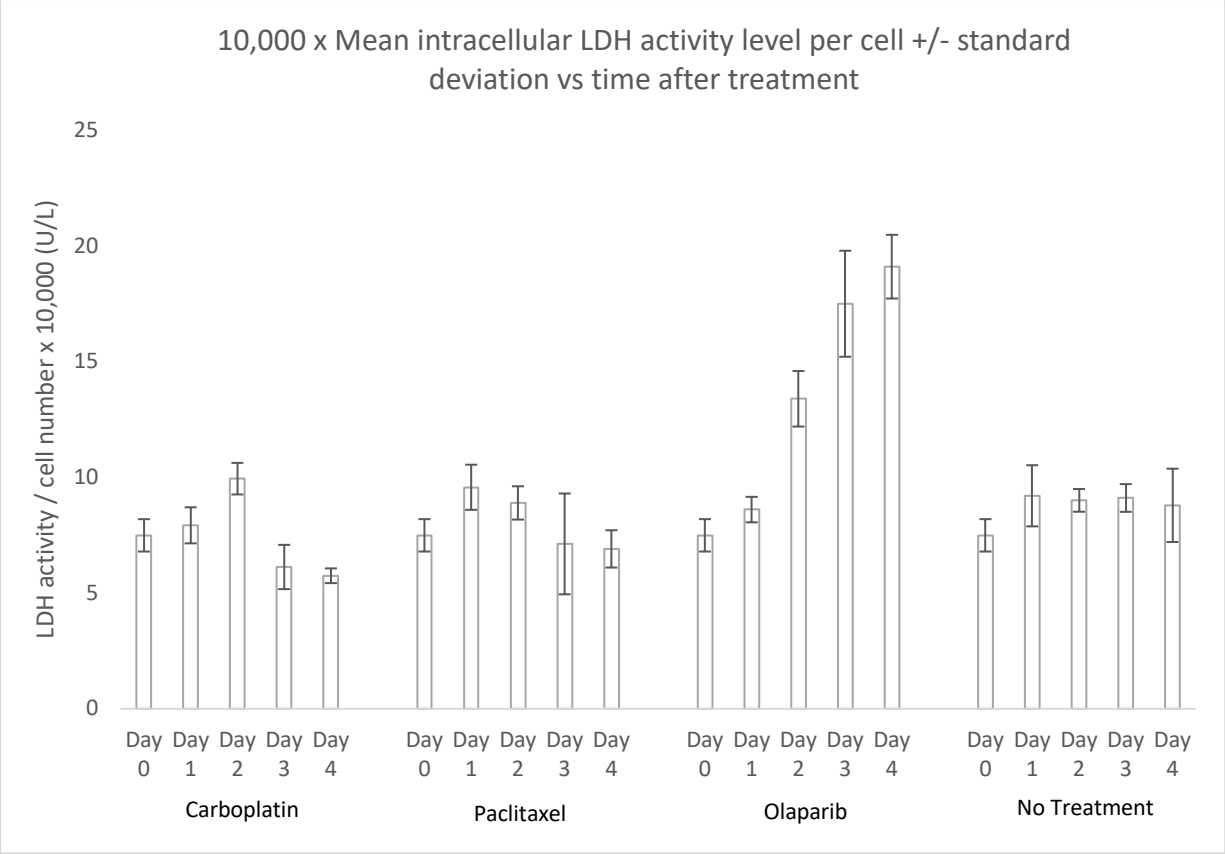

Figure 8.6: Plot of mean intracellular LDH activity per cell against time after treatment

8.5 Discussion

These preliminary *in vitro* results show that olaparib and paclitaxel at the doses used here are effective in preventing cell growth in PEO1 cells. In both treatments this inhibition is associated with a rise in extracellular lactate when corrected for cell number which may be driven by oxidative stress or cell death. In the case of olaparib the inhibition of cell number progression is also associated with an increase in LDH activity compared to the other ovarian cancer therapies. The raised LDH activity in the olaparib group may partially explain the elevated extracellular lactate demonstrated in this group of cells however, as LDH was not elevated in the paclitaxel group, other mechanisms are likely to also contribute to the elevated extracellular lactate. Other factors that may contribute to elevated extracellular lactate include; elevated intracellular lactate, alterations in the concentration of NAD(H),

changes in MCT expression, rapid cellular proliferation and cell death with release of intracellular contents into the extracellular environment. In this study, the intracellular lactate levels were low after cell processing for accurate measurement using the spectroscopic methods employed here so the effect of intracellular lactate on extracellular lactate concentration could not be assessed.

Except for the olaparib group, intracellular LDH activity remained stable over time when corrected for cell number. The response of LDH to olaparib in these experiments appears to occur by Day 2. By Day 4 the activity rose in the olaparib group to almost double that of the untreated cell group. PARP inhibitors may increase LDH activity and lactate concentration by increasing NAD^+/NADH levels. This is contrary to the effect seen with conventional chemotherapy drugs and cell lines where successful therapy response is almost universally associated with a reduction in LDH activity as measured by a reduction in the exchange rate constant of hyperpolarized ^{13}C-pyruvate to ^{13}C-lactate or k_{PL} (227). This finding could represent a potentially novel method of measuring response to targeted therapy. LDH activity measurements made from the supernatant did not show any significant changes over time of between chemotherapy treatments and this may reflect the low levels of extracellular LDH in comparison to the intracellular fraction or could be due to enzyme degradation or inactivation during extraction.

8.6 Conclusions and future work

This data has shown that changes in extracellular lactate occur in ovarian cancer cell lines over time following treatment and that these may be used for monitoring therapy response. They also show that PARP inhibitors may cause alterations to LDH related to their mode of action in preventing depletion of NAD(H), which as a co-factor for the enzyme LDH can be probed with hyperpolarized carbon-13.

Hyperpolarized imaging of lactate formation in patients undergoing PARP inhibitor treatment could help improve our understanding of the mechanism of action of PARP inhibitors *in vivo* and may be able to detect an early response to PARPi treatment because of the increase in LDH activity. The LDH response in cells seems to occur at 2-3 days post-treatment and this finding agrees with previous studies using other cell lines and tumour

models although that have shown a decrease in hyperpolarized ^{13}C-lactate signal around this time period following treatment (228) . The precise timing of the response in patients in the clinical setting would be expected to vary from the timing in cells experiments on pure cell lines, given the complex tumour microenvironment of cancers but future experiments with further cell lines, later time points, additional chemotherapy drugs and alternative doses may help improve understanding of the initial results found here.

The findings of these experiments support the translation of HP ^{13}C-MRI into ovarian cancers, particularly in the context of ovarian cancer and the potential for HP ^{13}C-MRI to non-invasively detect BRCA mutation could lead to further clinical applications in genetics and therapeutics for this imaging technique.

Chapter 9

Case report on hyperpolarized carbon-13 MRI and combination ^{18}F-FDG-PET/MRI in an ovarian tumour

---

9.1 Background

^{18}F-FDG-PET and hyperpolarized carbon-13 MRI (HP ^{13}C-MRI) both image tissue metabolism but they do so in different ways and provide different information on tissue function. ^{18}F-FDG-PET probes the spatial distribution of ^{18}F labelled compounds in tissue and cannot distinguish between the chemical compositions of the different molecules that carry the radioactive ^{18}F label. By comparison HP ^{13}C-MRI uses chemical shift information from spectroscopy to identify different metabolites of the ^{13}C tracer and is sensitive to the carrier molecule to which the ^{13}C is attached. HP ^{13}C-MRI and ^{18}F-FDG-PET also look at different steps in the metabolism of glucose, different enzyme activities and different transporters. Figure 9.1 summarises some of the differences in the metabolic pathways probed by ^{18}F-FDG-PET and HP ^{13}C-MRI.

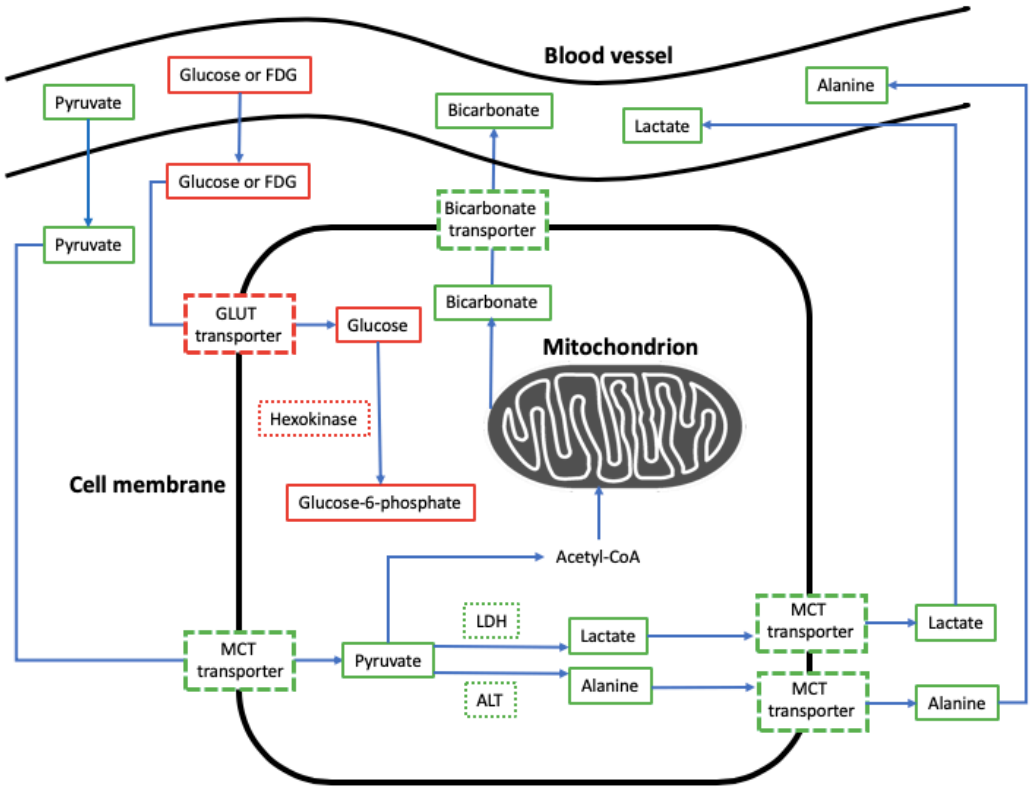

Figure 9.1: Metabolic pathways that can be studied with ^{18}FDG-PET (red) and HP ^{13}C-MRI (green)

When used together, ^{18}F-FDG-PET and HP ^{13}C-MRI provide complementary information to each other and give a more complete picture of the metabolism of glucose *in vivo* than either form of imaging on its own. Simultaneous ^{18}F-FDG-PET and HP ^{13}C-MRI, termed hyperPET, has been performed in a canine cancer model and has shown that HP ^{13}C-MRI is more specific for the Warburg effect, while ^{18}F-FDG-PET could not differentiate between increased glucose uptake from the processes of oxidative phosphorylation and glycolysis (229).

^{18}F-FDG-PET imaging has a low spatial resolution and must be combined with anatomical imaging from CT or MRI to give meaningful clinical information. Clinical ^{18}F-FDG-PET imaging is most often combined with CT as this provides adequate anatomical information, simple and accurate attenuation correction and is cheaper, faster and more accessible than MRI. MRI has the advantages over CT when combined with ^{18}F-FDG-PET however that it does not

add to the radiation exposure of the patient and provides multiple additional forms of tissue contrast. When used with HP ^{13}C-MRI, the combination of ^{18}F-FDG-PET/MRI can be more accurately co-registered and compared to the HP ^{13}C-MRI images than co-registration with ^{18}F-FDG-PET/CT. Furthermore, HP ^{13}C-MRI has great potential to provide novel and complementary information on metabolism when combined with ^{18}F-FDG-PET.

There are no published examples of the combination of a HP ^{13}C-MRI and ^{18}F-FDG-PET/MRI scan in a human. To investigate the feasibility of this combination of imaging and the differences that can be detected between HP ^{13}C-MRI and ^{18}F-FDG-PET in a human, a patient with an ovarian mass was imaged with both HP ^{13}C-MRI and ^{18}F-FDG-PET/MRI as part of this PhD for the first time. HP ^{13}C-MRI derived metabolite maps and SUV_{max} values from the ^{18}F-FDG-PET scan for different tissue types were then compared to each other and the surgically extracted tissue from the patient was analyzed to obtain information on the biological factors that affect the signal in HP ^{13}C-MRI.

9.2 Methods

Study design

The HP ^{13}C-MRI and ^{18}F-FDG-PET/MRI imaging of a patient with an ovarian tumour preformed for this work were completed as part of the MISSION-ovary (Molecular Imaging and Spectroscopy with Stable Isotopes in Oncology and Neurology - ovary) study.

Clinical details of patient

A 70-year-old woman with an ovarian mass was recruited for HP ^{13}C-MRI and ^{18}F-FDG-PET/MRI imaging. The patient first presented to her general practitioner (GP) after noticing a purple discolouration around her umbilicus. US at that time revealed a large soft tissue mass and further evaluation was carried out with a CT scan.

CT confirmed a large complex soft tissue mass in the midline of the abdomen appearing to arise in the pelvis from the right ovary and which measured a maximum of 187 x 136 mm in

axial dimensions. Multiple areas of calcification were also noted superiorly and there was a moderate volume of ascites. No definite discrete peritoneal deposits or omental cake could be identified. Images from the CT scan of the tumour are shown in Figure 9.2. The serum tumour marker and other blood results taken under the research protocol before imaging are given in Table 9.1:

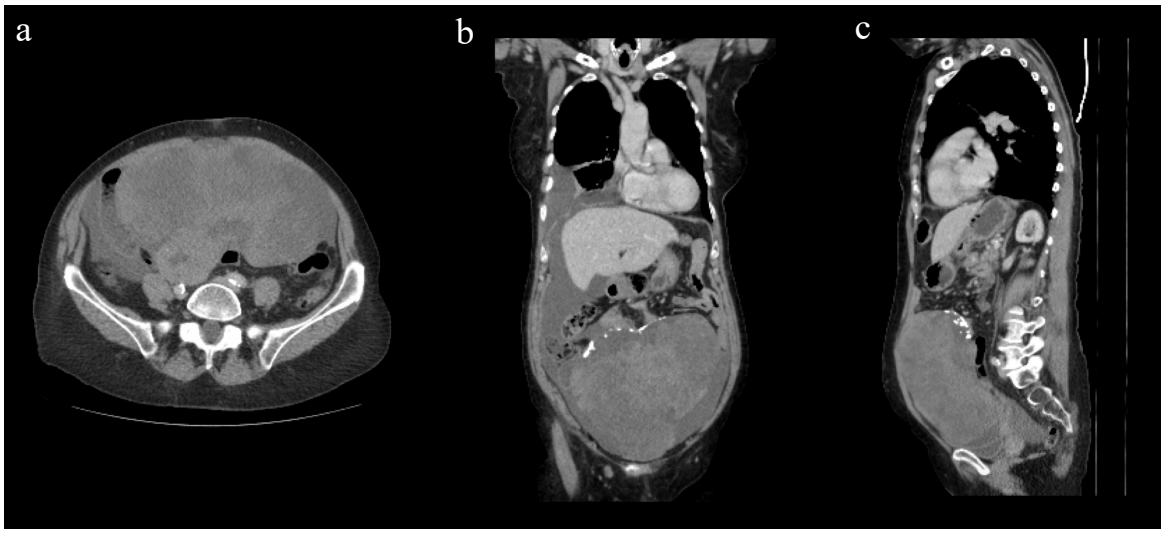

Figure 9.2: CT scan of first HP ^{13}C-MRI and ^{18}F-FDG-PET/MRI case. (a) axial image, (b) coronal reformatted image, (c) sagittal reformatted image.

Serum marker	Result	Normal range	Units
CA125 (carcinoma antigen 125)	473	0-35	U/L
CEA (carcinoembryonic antigen)	1.9	0.0-5.0	μg/L
AFPT (alpha fetoprotein)	3	0-10	kU/L
Intact hCG (human chorionic gonadotropin)	4.4	0.0-4.0	U/L
Free hCG (human chorionic gonadotropin)	<0.2	0.0-0.2	U/L
Oestrogen	98	<118	pmol/L
FSH (follicle stimulating hormone)	37.6	21-140	U/L
Glucose	5.4	-	mmol/L
Lactate	2.3	0.1-1.8	mmol/L
LDH (lactate dehydrogenase)	143	100-190	U/L
ALT (alanine transaminase)	13	7-14	U/L

Table 9.1: Blood test results for the first hyperPET patient.

After discussion at the MDT, primary surgery was scheduled to obtain a histological diagnosis. The patient was recruited to MISSION-ovary prior to surgery despite no histological diagnosis based on an RMI score at recruitment of 3 (complex mass and ascites on US) x 3 (post-menopausal score) x 473 (CA-125 level in U/L) = 4257, corresponding to a high chance of malignancy (RMI score > 200). The patient was also found to have other serum tumour marker results that were consistent with HGSOC (see Table 9.1). The subsequent post-operative histology after the MISSION-ovary research study imaging had been performed in this patient however showed that this lesion was a fibroma which was an unlikely finding giving the pre-operative diagnostic test results.

^{18}F-FDG-PET/MRI imaging

^{18}F-FDG-PET/MRI scanning was performed on the patient five days before surgery using a 3 T PET-MR scanner (Signa, GE Healthcare, Waukesha WI) at the Wolfson Brain Imaging Centre (WBIC), Cambridge Biomedical Campus, Cambridge. The patient was fasted for 12

hours prior to her ^{18}F-FDG-PET/MRI examination. After an uptake period lasting 60 min following intravenous injection of 4 MBq/kg ^{18}F-FDG (Alliance Medical), the participant underwent the PET acquisition and simultaneous MRI which lasted 30 minutes and covered an anatomical area from just above the diaphragm to the mid-thigh.

A single blood sample was acquired immediately prior to the ^{18}F-FDG injection to measure plasma glucose concentration and other blood markers. PET/MR acquisition was performed in caudo-cranial direction using 3 bed positions (8 min/bed position) with the patient placed in the supine position. PET emission data were reconstructed into a 256x256 image matrix with 2.34x2.34x2.78 mm voxels, using time-of-flight ordered subsets expectation-maximisation (TOF-OSEM) with 2 iterations and 28 subsets. Corrections for randoms, dead time, normalisation, attenuation, scatter and sensitivity and isotope decay were applied as implemented on the scanner by the manufacturer, together with a 6-mm FWHM Gaussian filter post reconstruction. MR for attenuation correction (MRAC) utilised the vendor-supplied two-point Dixon sequence. T_2-weighted proton MRI images were also acquired during imaging.

HP ^{13}C-MRI imaging technique

HP ^{13}C-MR was undertaken the day after PET imaging using a 3T MR system (MR750, GE Healthcare, Waukesha WI) in the Addenbrooke's Hospital Magnetic Resonance Imaging and Spectroscopy unit. At the time of the PET imaging, it was not possible to acquire HP ^{13}C-MR imaging on the PET/MRI system due to a Quality Control (QC) failure with the hyperpolarizer at the WBIC.

Pharmacy kits/fluid paths for insertion into the clinical hyperpolarizer (SPINlab, 5T, Research Circle Technology, Niskayuna, NY) were filled under sterile conditions. 1.47g [1-^{13}C]pyruvate acid (Sigma Aldrich, St Louis, Missouri, USA) containing 15 mM of an electron paramagnetic agent (EPA, Syncom, Groningen, Netherlands) was sealed in a vial; 38 mL sterile water was used for dissolution; 19 mL sterile water with 17.5 mL NaOH/Tris/EDTA (2.4%, 4.03%, and 0.033% w/v respectively, Royal Free Hospital, London) was used as a buffer for neutralisation. Pharmacy kits were stored in a freezer at -20 °C for at least two weeks prior to use. The vial containing the frozen pyruvate/EPA mix was defrosted in the helium

pressurised airlock in the hyperpolarizer for one hour. The sample was irradiated at 139 GHz at ~0.8 K for approximately three hours. Following rapid dissolution, the pyruvic acid was neutralised with the buffer and QC checks were performed by an integrated QC module which measured: pyruvate and EPA concentration, pH, temperature, sample polarization and volume of dissolute. The release criteria for injection were: pyruvate concentration 220-280 mM; radical concentration < 3 μM; pH 6.7-8.1; and temperature 25-37 ºC. QC checks on the dissoluted hyperpolarized ^{13}C-pyruvate that was injected into the patient produced results of:

Polarisation: 16.1%

Pyruvate concentration: 265 mM

EPA concentration: 0.8 μM

pH: 7.2

Temperature: 33.1°C

Volume of pyruvate: >40mL

After release from the QC, the HP ^{13}C-pyruvate sample was passed through a radio frequency (RF) shielded hatch and injected with an automated Medrad pump set to deliver the injection at 5 mL/s and a dose 0.4 mL/kg (Medrad, Warrendale, Pennsylvania, USA). The hyperpolarized pyruvate injection was followed by a 25 ml 0.9% saline bolus infusion at 5 mL/s to accelerate delivery of the pyruvate to the tumour. The actual volume of pyruvate injected into the patient was 27.9 mL and the time from dissolution to injection was 51s.

A delay of 16 s was allowed for the pyruvate to undergo metabolism to lactate in the tissue. ^{13}C-MRSI (magnetic resonance spectroscopic imaging) was performed using an IDEAL spiral pulse sequence with nominal flip angle 20°, acquisition time 120 s, FoV 36 x 36cm, in-plane resolution 18 x 18 mm and five slices each 3.5 cm thick positioned across the pelvic mass with a 5 mm gap between the slices. Transmit Gain and center frequency (f0) were determined using a Bloch-Siegert method. A clamshell body coil from GE was used for RF

excitation and an 8-channel abdominal array from Rapid (Rimpar, Germany) was used as the receive coil. Five spectral peaks were imaged: ^{13}C-pyruvate, ^{13}C-lactate, ^{13}C-pyruvate hydrate (the hydrated form of pyruvate which exchanges with the unhydrated form), ^{13}C-bicarbonate (produced from ^{13}C-carbon dioxide catalysed by carbonic anhydrase *in vivo*) and ^{13}C-alanine. The spectra were recorded at 30 timepoints, each 4 s apart. Data were reconstructed using Matlab (The Mathworks, MA, USA). Time-averaged images of ^{13}C-pyruvate, ^{13}C-lactate and ^{13}C-bicarbonate over all timepoints were calculated for each slice. Reconstruction was preformed by Dr Mary McLean from Cancer Research UK and the University of Cambridge Department of Radiology.

9.3 Results

Figure 9.3 shows the ^{18}F-FDG-PET/MRI imaging appearance for a slice through the mass. The ^{18}F-FDG uptake appeared spatially very heterogenous. SUV_{max} of the mass was 1.54. Figure 9.4 shows the spectra and images of different ^{13}C molecules. Summed metabolite maps are shown in Figure 9.5 with the corresponding ^{18}F-FDG-PET images for comparison. Figure 9.6 displays graphically the relationship of SUV_{max} to HP ^{13}C-pyruvate signal for selected tissue types.

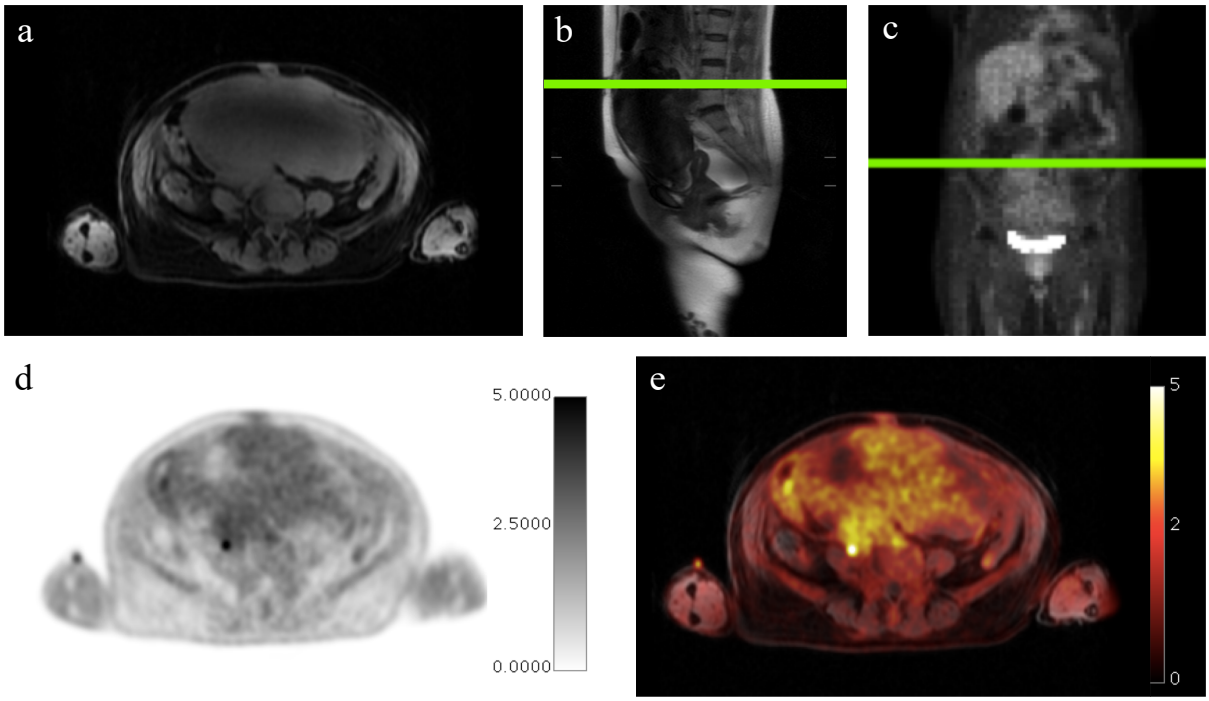

Figure 9.3: ^{18}F-FDG-PET/MRI imaging. (a) Axial proton image through the pelvic mass, (b) sagittal section showing the level of the axial slice, (c) coronal section showing level of axial slice, (d) ^{18}F-FDG-PET image, scale bar represents SUV values, (e) fusion of ^{18}F-FDG-PET and proton MRI, scale bar represents SUV.

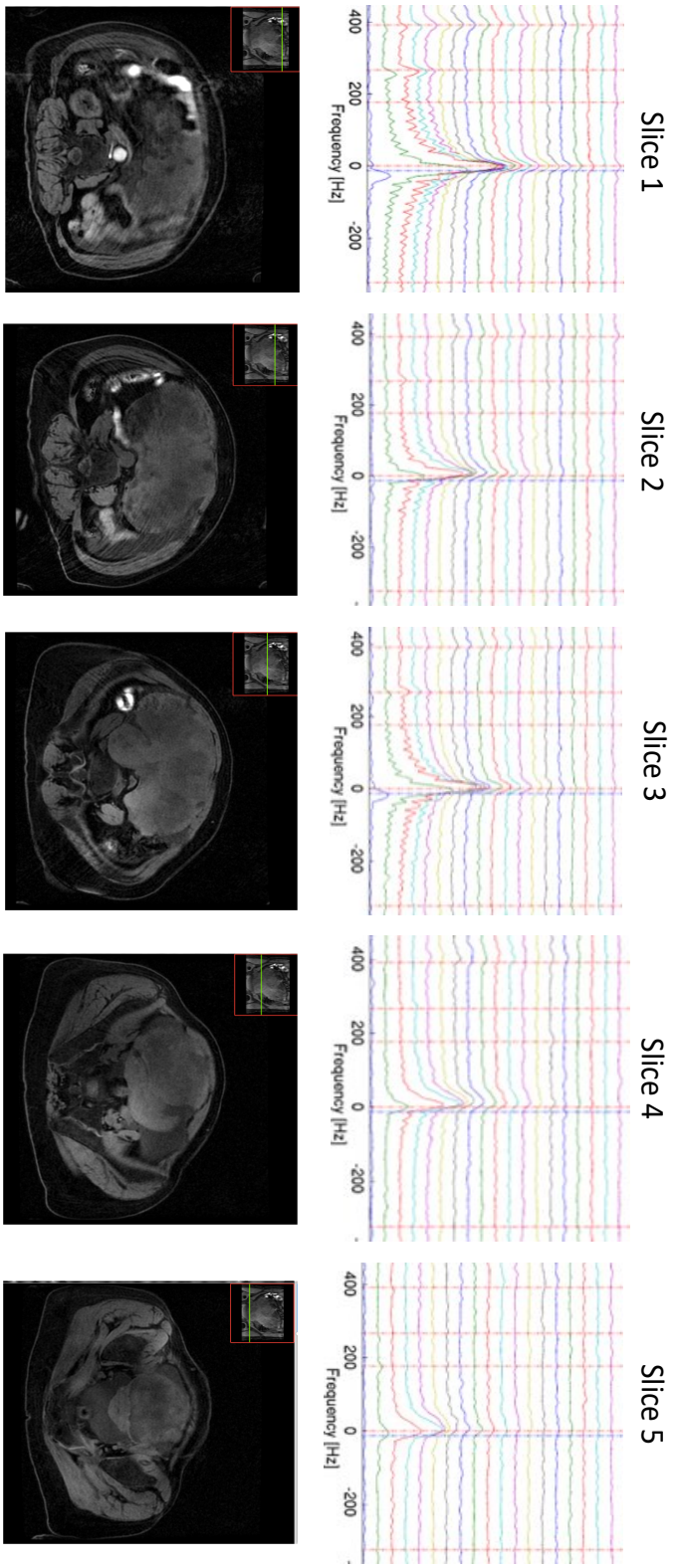

Figure 9.4: ^{13}C-MRI slice positions shown on proton images (bottom) and dynamic spectra (top) imaged through the ovarian mass.

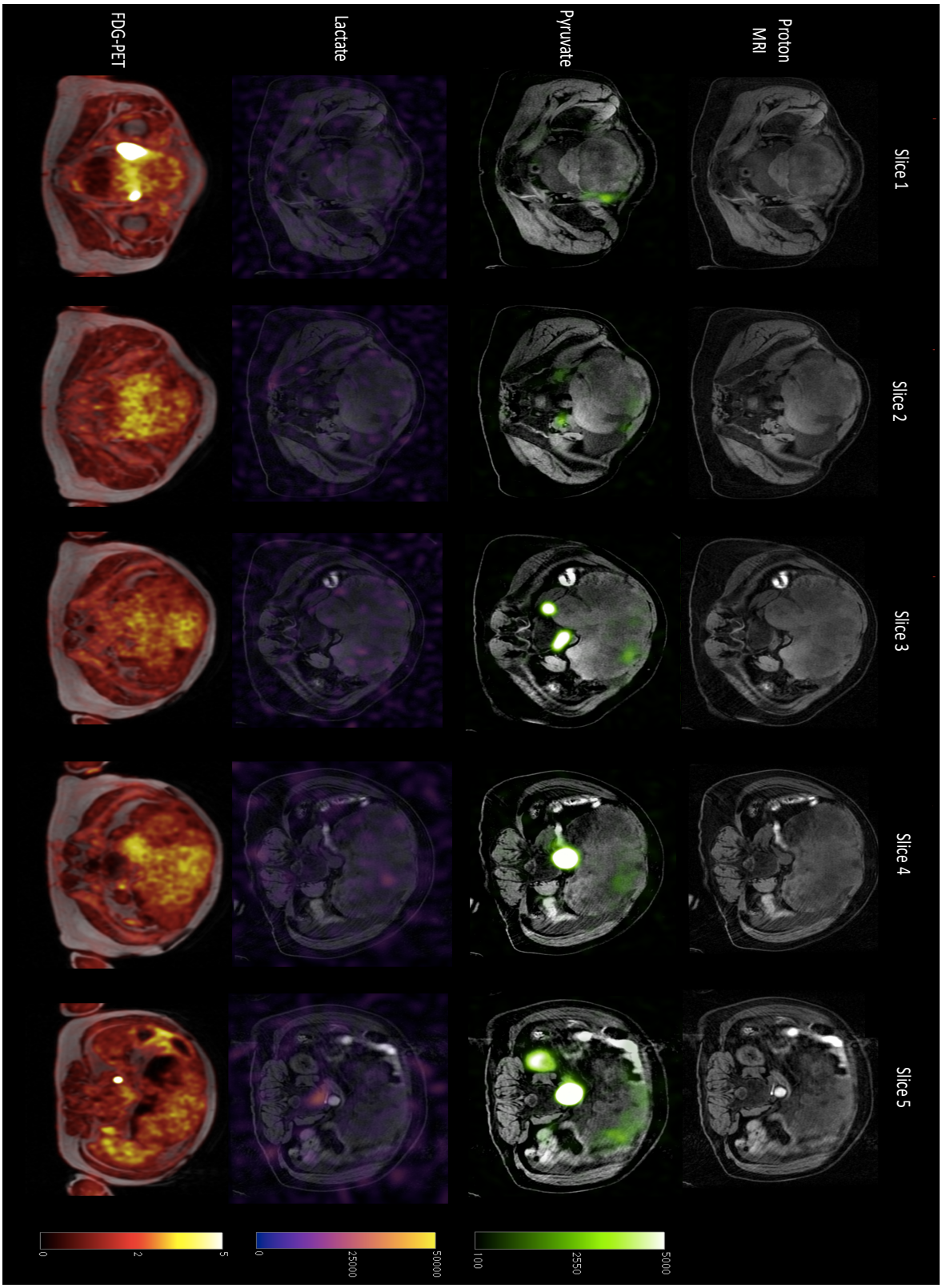

Figure 9.5: ^{13}C-MRI metabolite maps showing the spatial distribution for pyruvate and lactate and the corresponding ^{18}F-FDG-PET images.

Two approaches were used to evaluate the metabolism of the ^{13}C-pyruvate: firstly a ratiometric approach of ^{13}C-lactate-to-pyruvate (summed over the time course), as a simple surrogate for the exchange reaction. Secondly, a 2-site exchange model was used to calculate maps of k_{PL}, the apparent exchange rate constant for the LDH reaction which also incorporates perfusion and transport as described by Khegai (230). Due to the very low lactate signal because the tumour was non-malignant these evaluations of metabolism failed to produce meaningful results as noise levels were similar to lactate levels making measurements unreliable.

9.4 Discussion

This work presents the first example of HP ^{13}C-MRI of an ovarian mass in a human. There have been several pre-clinical studies which assessed the combination of FDG-PET and HP ^{13}C-MRI: for example, *in vitro* studies have shown that the treatment response measurements are similar for the two techniques in breast cancer models (231) and recent work has shown the feasibility of this imaging in canine cancer models (232). There is currently a single published human study that compared HP ^{13}C-MRI with ^{18}F-FDG-PET/CT in a glioma patient but not with ^{18}F-FDG-PET/MRI (233). The ovarian case presented here extends these previous pieces of work to show that the combination of ^{18}F-FDG-PET/MRI and HP ^{13}C-MRI is possible in a human for the first time.

Ovarian cancer is metabolically active and well perfused and therefore a good model for studying cancer metabolism. The patient in this work was recruited onto the study due to a high suspicion for HGSOC but the lesion was unfortunately found to be benign after extraction at surgery. The uptake of ^{18}F-FDG and the formation of ^{13}C-lactate were much lower than was expected at recruitment due to the benign nature of the mass. Nonetheless, this work has demonstrated proof-of-principle that combined ^{18}F-FDG-PET/MRI and HP ^{13}C-MR can be carried out in a clinical setting.

The HP ^{13}C-MRI data collected here was analysed both from spectra and from constructed images. On the summed spectra, there were peaks detected for ^{13}C-pyruvate, ^{13}C-lactate and ^{13}C-pyruvate hydrate but not for ^{13}C-bicarbonate or ^{13}C-alanine. Although ^{13}C-bicarbonate is generated in healthy tissue such as the normal brain and heart where there

are high levels of PDH, it is rarely seen in tumours. ^{13}C-alanine is detected in muscle and in the liver where there are high levels of ALT and was not expected to be found in an ovarian mass.

There was sufficient signal in this case to generate ^{13}C-pyruvate images which appeared to have reflected tissue perfusion. Although ^{13}C-lactate images were produced (Figure 9.5), given the benign nature of the lesion, these demonstrated only low level ^{13}C-lactate levels and the images were too noisy for detailed analysis such as with kinetic modelling to calculate k_{PL} and ^{13}C-lactate-to-pyruvate maps.

Importantly however, there was a visible difference in the areas of uptake of ^{18}F-FDG and ^{13}C-pyruvate signal both for tumour and for healthy tissue. This is a promising result which supports the possibility that ^{18}F-FDG-PET and HP ^{13}C-MRI measure different aspects of glucose metabolism and suggests that HP ^{13}C-MRI may have a complementary role to ^{18}F-FDG-PET in metabolic imaging. For example, ^{18}F-FDG-PET may measure GLUT transport and hexokinase activity for the first few steps in glycolysis whereas ^{13}C-pyruvate may measure perfusion and MCT transport. ^{13}C-lactate measurements in cases with better signal could also additionally probe the enzymatic steps glycolysis by assessing LDH activity. Further work is needed to identify which biological processes or properties of tissue are measured with HP ^{13}C-MRI: this question can partially be addressed by tissue analysis following HP ^{13}C-MRI imaging.

A quantitative comparison of ^{18}F-FDG-PET and HP ^{13}C-MRI could be carried out in the future in more metabolically-active tissue using a pixel-by-pixel image analysis approach; for the particular case used in this study, the uptake of both ^{13}C-pyruvate and ^{18}F-FDG-PET were low (tumour SUV_{max} = 1.54) as the mass was not a cancer, making it difficult to undertake such a direct comparison in the context of a low signal-to-noise ratio. Future work after this PhD is planned to address this through the recruitment of patients with confirmed HGSOC lesions that are more likely to be ^{18}F-FDG avid, to produce high concentrations of lactate (234) and to have high LDH concentrations (235) which would more likely be detectable with hyperpolarized carbon-13 imaging.

HP ^{13}C-pyruvate imaging may also be improved in the future by applying a correction to the signal from the perfusion measurements derived using dynamic contrast enhanced (DCE)

MRI. For example, by making use of K^{trans} (the volume transfer co-efficient and measure of capillary permeability) to adjust the hyperpolarized ^{13}C metabolite and kinetic rate constant maps. The much smaller molecular weight of pyruvate compared to gadolinium contrast agents may also mean that HP ^{13}C-MRI of pyruvate could be a more sensitive indicator of tissue permeability than DCE.

In conclusion, HP ^{13}C-MRI and ^{18}F-FDG-PET were successfully performed on the same patient for the first time. Two previous attempts at HP ^{13}C-MRI imaging in ovarian cancer patients at Cambridge failed. In the first case failure was due to dissolution into a solution of the wrong concentration for injection by the hyperpolarizer and in the second case the detector coil malfunctioned and prevented detection after injection of hyperpolarized ^{13}C-pyruvate into the patient. The results of the successful scan indicate that combined HP ^{13}C-MRI and ^{18}F-FDG-PET is feasible in a clinical setting. Further clinical studies are now needed to compare HP ^{13}C-MRI with tissue analysis to identify the specific metabolic properties of tissue that the HP ^{13}C-MRI molecules probe. In the future, the HP ^{13}C-MRI technique demonstrated here could be used to stratify tumours based on metabolic phenotype, genetics like the presence of a BRCA mutation and to detect early treatment response as has already been demonstrated in animal models.

Chapter 10

Magnetic resonance fingerprinting in ovarian cancer

10.1 Background

Quantitative parameter mapping is a more reproducible method of imaging than many forms of contrast generated with MRI, as it is not as dependent on the performance of the scanner hardware. Quantitative maps however have traditionally taken a long time to produce due to the need to repeat imaging multiple times with different acquisition parameter values and this has limited clinical utility. Magnetic resonance fingerprinting (MRF) provides a method to significantly shorten scan times and could allow parameter mapping to become practical in a clinical setting.

In MRF, a dictionary is created for each imaging session from a user prescribed set of imaging parameters usually derived from the Bloch equations such as T_1, T_2 and flip angle. Selection of imaging parameters for dictionary generation is based on the types of image reconstructions intended by the user. The greater the number of parameters that is included for dictionary creation, the longer it takes for the dictionary to be created and the greater the number of possible signal evolutions, which means more storage space is needed.

MRF may produce images that have different sensitivity to tissue properties than conventional proton imaging sequences because of its use of a theoretical modelling of the signal with selected MR imaging parameters and may lead to improved detection of tissue heterogeneity which could in turn relate to disease progression (236). While tissue heterogeneity can be detected on T_1 and T_2 weighted images, tissue heterogeneity from MRF may also be obtained more directly from quantitative maps which can be useful in the

rapidly evolving field of radiomics which at times aims to quantify heterogeneity on imaging (237).

Because MRF can examine a large number of MR parameters in a short period of time, it may add value to the detection of lesions in tumours that are located in anatomical areas with diverse tissue types in the background such as the female pelvis. As part of this PhD, a proof-of-concept study was designed where MRF was applied to the imaging of ovarian cancer and used to generate T_1, T_2 and PD maps to investigate whether MRF can be used provide information on the characterisation of ovarian masses in patients. Results from the work have been published in *IEEE Transactions on Radiation and Plasma Medical Sciences* (238).

10.2 Methods

Imaging

Imaging was performed on a 3.0 T MRI system (MR750, General Electric, Milwaukee, WI, USA) using a 32-channel abdominal coil. All patients were imaged in the supine position. The MRI protocol consisted of standard qualitative clinical sequences followed by a 2D steady-state-free-precession (SSFP) MRF sequence (239).

The MRF data was acquired using 979 frames with golden-angle spiral k-space interleafs. The golden-angle interleafs enabled the repetition time and flip angle lists used to match the values in Jiang et al. (240, 241). Further sequence parameters were: field-of-view = 380 x 380 mm^2; matrix = 192 x 192; voxel size = 2.0 x 2.0 x 3.0 mm^3; slice thickness = 3.0 mm; slice spacing = 1.0 mm; sampling bandwidth = ±250 kHz; TE = 1.8 ms; acquisition time = 15 sec/slice; and TR was varied based on Perlin noise. The max gradient strength per spiral was 17 mT/m and the max slew rate was 62 T/m/s. The gradient strength was limited to low maximum values to ensure that a large Nyquist FOV would be obtained to cover the whole abdomen. The scanner was operated by Dr Joshua Kaggie, an MRI physicist from the University of Cambridge Department of Radiology.

MRF Dictionary Simulation

Dictionary simulations of SSFP signal evolutions were performed using the extended phase graph formalism. The detailed ranges and incremental (step-size) changes used for T_1 and T_2 included in the dictionary are listed in Table 10.1. This range was chosen to extend sufficiently for capturing both low relaxation values, which occur in dense tissue, and high relaxation values, which occur in highly fluidic regions such as ascites. The increments were chosen to have higher densities near low relaxation values, where the increments correspond to a larger percentage change for each dictionary value.

Parameter	Range (ms)	Increment (ms)
T_1	10 - 400	10
	400 - 4000	20
T_2	2 - 20	1
	20 - 400	2
	400 - 2500	20

Table 10.1: Detailed ranges and incremental changes used for T_1 and T_2 in the dictionary

MRF Reconstruction and Analysis

After acquiring the data, each under-sampled spiral acquisition was reconstructed using a non-Cartesian FFT, resulting in 979 undersampled images. MRF uses a relatively simple pattern recognition algorithm to identify the tissue and its corresponding properties in each voxel. The inner products between the normalized measured signal evolution of each voxel and each normalized dictionary entry were then calculated with the dictionary entry returning the maximum value of the inner product, taken as the best representation of the acquired signal evolution and the respective T_1 and T_2 values are consequently assigned to the voxel. The proton density (PD) map was calculated as the scaling factor used to match the dictionary simulation with the measured signal evolution. Mean T_1 and T_2 values for the three tumour types were calculated in Matlab from regions-of-interest (ROIs) drawn using

software written in Python Language Reference (Python Software Foundation) version 2.7 with Matplotlib on four consecutive slices. The ROI analysis was also preformed by Dr Joshua Kaggie.

10.3 Results

Four patients were imaged: one borderline serous, two untreated high-grade serous (one with peritoneal deposits plus ascites and the other with the cancer located primarily in the ovary), and one post chemotherapy HGSOC. The generated T_1, T_2 and PD maps of the four patients are shown in Figure 10.1. Mean T_1 and T_2 values and their standard deviations (SDs) estimated from ROIs for each tumour type are listed in Table 10.2.

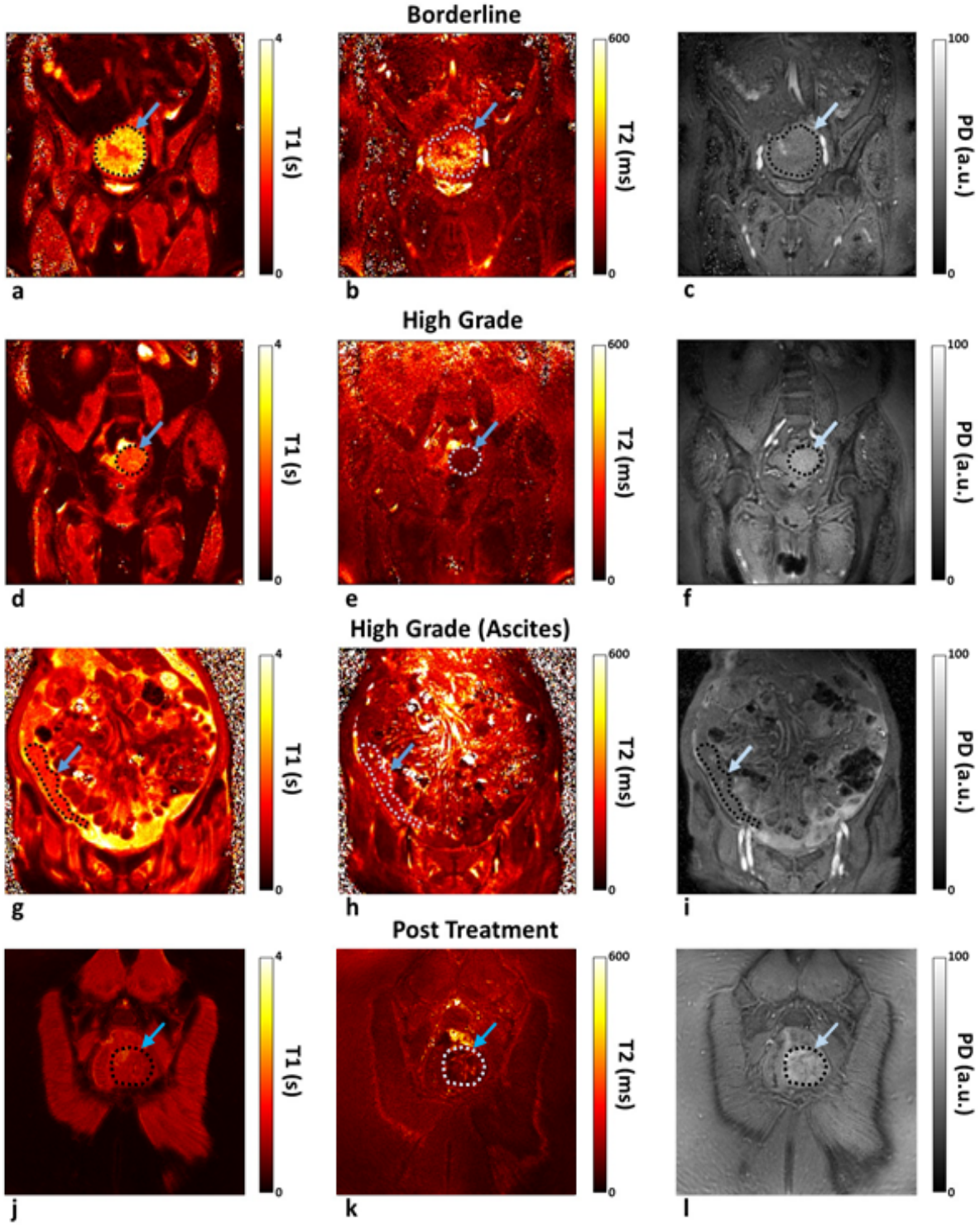

Figure 10.1: MRF generated T_1, T_2 and PD map

Tumour type	T_1 (ms)	T_2 (ms)
Borderline	2465 ± 101	225 ± 34
HGSOC (ovarian location)	1975 ± 191	94 ± 15
HGSOC (peritoneal deposits)	1621 ± 46	174 ± 26
Post-treatment HGSOC	1059 ± 55	116 ± 12

Table 10.2: MRF derived relaxation values of different ovarian tumour types

10.4 Discussion

Here we demonstrated the feasibility of using MRF for fast quantification of relaxation parameters in ovarian cancer. The borderline serous tumour had a higher T_1 value than the two high-grade carcinomas, which were easily distinguishable from each other on the MRF maps. The patient post-treatment demonstrated lower T_1 and T_2 values compared to the other three patients with borderline or high-grade carcinoma. Mean T_1 and T_2 relaxation times of the borderline ovarian tumour were longer by ~20% and ~58%, respectively, when compared with the high-grade tumours.

The sample size investigated here was small which makes it difficult to draw any definite conclusions from the findings. Further studies are required to confirm and verify these findings in a larger cohort and to demonstrate the robustness of the results. MRF-generated quantitative maps will also need to be compared to conventionally obtained parameter maps using a variable flip angle approach in the future. If these future comparisons validate MRF as a fast, reliable and enhanced alternative to the time-consuming “gold-standard” approaches, it could enable MRF to find a clinical role. The MRF method used here could also be improved by increasing its resolution to detect smaller tumour lesions with higher accuracy. In addition to relaxation times, the MRF methodology employed in this study could be expanded with measurements of other tissue properties such as diffusion and perfusion to gain more information for an improved classification of tumour masses.

In conclusion, this work is the first demonstration of MR Fingerprinting in ovarian cancer imaging in four subjects. The generated quantitative MRF maps in this proof-of-concept

work revealed that T_1 and T_2 differences can be detected and this could potentially be applied to better characterise tumour lesion. Further work is now needed to expand on these results by comparing the MRF generated maps with conventionally acquired T_1, T_2 and PD maps.

Chapter 11

Conclusions

11.1 Summary of imaging findings in ovarian cancer

Several novel imaging techniques to investigate ovarian cancer have been presented as part of this PhD dissertation and these have each been shown to provide information on different tumour properties, which could be of use clinically. DKI was shown to predict responders to cytotoxic drugs. ^{23}Na-MRI was found to measure cellularity that could be applied to monitoring treatment response. MT imaging was found to be a possible biomarker of tissue cellularlity and basement membrane integrity. HP ^{13}C-MRI of an ovarian mass was demonstrated for the first time and has the potential to give information on the metabolism of pyruvate, enzyme activity, transporter expression and genetic mutations in ovarian cancer. Finally, MRF was shown to provide quantitative parameter mapping that could improve imaging speed and reproducibility. Table 11.1 summarizes the pros and cons of each of the imaging techniques evaluated in this PhD.

Imaging technique	Advantages	Disadvantages	Tissue information provided
Diffusion kurtosis imaging (DKI)	1. Uses conventional proton imaging set-up 2. Parameter maps can be constructed offline on a separate computer saving scanner time.	1. Requires a scanner capable of high diffusion gradients 2. Due to low SNR, requires 3T or higher scanner 3. Longer scan time than for ADC mapping as images with larger number of b-values are required	1. Measures tissue heterogeneity 2. May relate to chemosensitivity and response to therapy 3. Like traditional DWI, DKI is affected by cellularity.
Sodium MRI (^{23}Na- MRI)	1. Non-invasively measures sodium concentration in tissue. 2. Provides the second largest endogenous MR signal after the hydrogen nucleus.	3. Requires a sodium coil and multi-nuclear scanner 4. Only feasible at 3T or higher due to low SNR 5. Long scan times 6. Sodium phantoms required for image calibration 7. High SAR for IWS imaging.	1. Inversely related to cellularity 2. May detect fluid accumulation from oedema/inflammation 3. Intracellular imaging may relate to tissue energy status and sodium transporter activity.
Magnetization transfer (MT) imaging	1. Fast scan and simple to acquire 2. Widely studied and physical origin well understood	1. Previously found to be of little clinical value in many diseases	1. Cellularity measurement 2. Tissue macromolecular content
Hyperpolarized carbon-13 spectroscopic imaging (HP ^{13}C-MRI)	1. Can provide real-time information on metabolism. 2. Can non-invasively map enzyme concentrations 3. May detect early metabolic response to treatment 4. Can measure downstream metabolites of pyruvate.	1. Requires a hyperpolarizer in a separate nearby shielded room from scanner 2. Requires 3T scanner or higher with multi-nuclear imaging capabilities. 3. Long preparation time required to sufficiently polarize sample 4. Expensive.	1. LDH enzyme activity 2. Endogenous lactate and pyruvate as these compete with C-13 labelled molecules and change the signal detected. 3. MCT transporter concentration 4. Tissue perfusion.
^{18}F-FDG-PET	1. Very sensitive at detecting increased metabolic activity 2. Shown to be effective at imaging cancer and detecting metastases.	3. Exposes patient and staff to radiation. 4. Requires preparation of FDG prior to imaging. 5. 60 to 90 minute waiting period required for uptake before imaging.	1. Hexokinase enzyme activity 2. GLUT transporter activity 3. Tissue perfusion 4. Cellularity 5. Metabolism of glucose
Magnetic resonance fingerprinting (MRF)	1. Very fast 2. Provides quantitative imaging	1. Takes a long time to construct parameter maps due to the need to generate a library. 2. New technique that is not well understood	1. Can measure the T1, T2 and proton density of tissue in addition to other properties like diffusion if set-up to do so.

Table 11.1: Summary of imaging techniques explored in this PhD

11.2 Future directions

The DKI results presented here require verification with larger patient numbers. The clinical implications of predicting the response of HGSOC to cytotoxic treatment with a non-invasive imaging technique are great however the number of patients used in this study was very small and the results are consequently prone to error.

The use of ^{23}Na-MRI to measure tumour cellularity may complement conventional cellularity measurements with DWI, additionally by combining total sodium measurements with intracellular weighted sodium (IWS) imaging, it is possible to have a measure of cell membrane integrity. ^{23}Na-MRI is affected by a variety of biological properties and comparison of imaging to tissue analysis is necessary to clarify the relative contributions of the different sodium transporters, perfusion effects, hypoxia and energy status changes in cancer. Higher field strength scanners such as 7T may improve the SNR of IWS imaging to detect the change in intracellular sodium with more specific physiological alterations in cancer.

MT imaging is a well-established MRI technique but despite this, the biological significance of MT is still poorly understood. The significance of the tumour microenvironment is now becoming increasingly apparent in oncology and MT imaging could re-emerge in radiology as a probe of extracellular matrix if larger studies can confirm the relationships suggested by the preliminary results found here.

HP ^{13}C-MRI is a financially costly technique that requires unique imaging expertise to be present at the imaging site. It the technique is to be translated into clinical practice then the most influential biological determinants of the HP ^{13}C-MRI signal must be determined to help identify a definite clinical application. There are a large number of possible biological properties of tissue that may affect the HP ^{13}C-MRI signal and the relative contribution of each must be understood if the imaging technique is to be used clinically. One method of achieving this could be to compare HP ^{13}C-MRI to tumour tissue derived at biopsy or surgery, where measurements have been made of the enzyme activities, transporter concentrations and endogenous metabolites concentrations.

Another major direction of current work in HP ^{13}C-MRI that was not explored in this PhD is the development of new tracers. The most promising options include carbon-13 labelled

fumarate whose metabolism to malate may be sensitive at detecting areas of necrosis within tumours (242). The challenges for fumarate imaging include the lower concentration of the tracer and the derived products compared to pyruvate and the relative lack of preclinical studies. The imaging of C-2 labelled pyruvate ([2-^{13}C]pyruvate) is also being assessed as a potential human tracer since it facilitates the passage of the C-13 label deeper into the citric acid cycle where chemical reactions and enzyme activities other than PDC, ALT, LDH and CA can be studied. Recent unpublished data has shown that this type of imaging may have clinical utility in the brain and in the heart but its role in cancer is uncertain; possibly because relatively few tumours have sufficient PDH to assess metabolism.

With the wide variety of MRI techniques available to clinicians and the unique information granted by each modality, the use more widespread use of MRF could allow multi-parametric imaging to be performed with greater efficiency and in a more cost-effective manner. A comparison of MRF-generated images with images obtained through dedicated MRI sequences that builds on the preliminary results of this PhD could help to establish MRF as a viable replacement for some types of traditional MRI.

The results of the research presented here emphasize the importance of expanding the use of clinical imaging from primarily a diagnostic tool used to obtain anatomical information into a role where it is used to address more relevant questions about tumour biology that can affect the way cancer is treated.

In summary, there is significant scope for non-invasive imaging of metabolic and microstructural information in ovarian and other cancers and through the work of this PhD, it has been demonstrated that several novel imaging tools could report on the tumour microenviroment in HGSOC and could find roles in the clinic in the future. After the proof-of-concept and feasibility study stages, the success of the imaging techniques studied here would eventually need to be evaluated against an outcome for patients such as progression free survival or an improvement in quality of life in prospective longitudinal trials as the ultimate goal of any medical imaging is to improve patient care.

References

1. Department of Health. Chief Medical Officer calls for action on women's health 2015 [cited 2016 03 Feb]. Available from: https://www.gov.uk/government/news/chief-medical-officer-calls-for-action-on-womens-health.

2. Cancer Research UK. The 10 Most Common Causes of Cancer Death in Females, UK, 2012 2012 [cited 2016 03 Feb]. Available from: http://www.cancerresearchuk.org/sites/default/files/cstream-node/cs_mort_10common_female.pdf.

3. Jiang R, Jiang J, Zhao L, Zhang J, Zhang S, Yao Y, et al. Diffusion kurtosis imaging can efficiently assess the glioma grade and cellular proliferation. 2015;6(39):42380.

4. Hambrock T, Somford DM, Huisman HJ, van Oort IM, Witjes JA, Hulsbergen-van de Kaa CA, et al. Relationship between apparent diffusion coefficients at 3.0-T MR imaging and Gleason grade in peripheral zone prostate cancer. 2011;259(2):453-61.

5. Ouwerkerk R, Jacobs MA, Macura KJ, Wolff AC, Stearns V, Mezban SD, et al. Elevated tissue sodium concentration in malignant breast lesions detected with non-invasive 23 Na MRI. 2007;106(2):151-60.

6. Ouwerkerk R, Bleich KB, Gillen JS, Pomper MG, Bottomley PAJR. Tissue sodium concentration in human brain tumors as measured with 23Na MR imaging. 2003;227(2):529-37.

7. Nelson SJ, Kurhanewicz J, Vigneron DB, Larson PE, Harzstark AL, Ferrone M, et al. Metabolic imaging of patients with prostate cancer using hyperpolarized [1-13C] pyruvate. 2013;5(198):198ra08-ra08.

8. Martens MH, Lambregts DM, Papanikolaou N, Heijnen LA, Riedl RG, zur Hausen A, et al. Magnetization transfer ratio: a potential biomarker for the assessment of postradiation fibrosis in patients with rectal cancer. 2014;49(1):29-34.

9. Ma D, Gulani V, Seiberlich N, Liu K, Sunshine JL, Duerk JL, et al. Magnetic resonance fingerprinting. 2013;495(7440):187.

10. Guarneri V, Piacentini F, Barbieri E, Conte PFJGo. Achievements and unmet needs in the management of advanced ovarian cancer. 2010;117(2):152-8.

11. Chen AP, Kurhanewicz J, Bok R, Xu D, Joun D, Zhang V, et al. Feasibility of using hyperpolarized [1-13C] lactate as a substrate for in vivo metabolic 13C MRSI studies. 2008;26(6):721-6.

12. Day SE, Kettunen MI, Gallagher FA, Hu D-E, Lerche M, Wolber J, et al. Detecting tumor response to treatment using hyperpolarized 13 C magnetic resonance imaging and spectroscopy. 2007;13(11):1382.

13. Kastan MB, Bartek JJN. Cell-cycle checkpoints and cancer. 2004;432(7015):316.

14. Seiden MV. "Gynecologic Malignancies". . In: In Longo DL KD, Jameson JL, Fauci AS, Hauser SL, Loscalzo J., editor. Harrison's Principles of Internal Medicine. 18th ed: McGraw-Hill.; 2012.

15. Meinhold-Heerlein I, Fotopoulou C, Harter P, Kurzeder C, Mustea A, Wimberger P, et al. Statement by the Kommission Ovar of the AGO: the new FIGO and WHO classifications of ovarian, fallopian tube and primary peritoneal cancer. 2015;75(10):1021-7.

16. Chen VW, Ruiz B, Killeen JL, Cote TR, Wu XC, Correa CN. Pathology and classification of ovarian tumors. Cancer. 2003;97(10 Suppl):2631-42. doi: 10.1002/cncr.11345. PubMed PMID: 12733128.

17. Serov SFS, Robert Edward; Sobin, Leslie H; World Health Organization;. HISTOLOGICAL TYPING OF OVARIAN TUMOURS: Geneva : World Health Organization; 1973. Available from: http://www.who.int/iris/handle/10665/41529#sthash.ySPsn6mX.dpuf.

18. Prat J, Oncology FCoG. Staging classification for cancer of the ovary, fallopian tube, and peritoneum. Int J Gynaecol Obstet. 2014;124(1):1-5. doi: 10.1016/j.ijgo.2013.10.001. PubMed PMID: 24219974.

19. Goff BA. Ovarian cancer: screening and early detection. Obstet Gynecol Clin North Am. 2012;39(2):183-94. doi: 10.1016/j.ogc.2012.02.007. PubMed PMID: 22640710.

20. Meyer T, Rustin GJJBjoc. Role of tumour markers in monitoring epithelial ovarian cancer. 2000;82(9):1535.

21. Jacobs I, Oram D, Fairbanks J, Turner J, Frost C, Grudzinskas JG. A risk of malignancy index incorporating CA 125, ultrasound and menopausal status for the accurate preoperative diagnosis of ovarian cancer. Br J Obstet Gynaecol. 1990;97(10):922-9. PubMed PMID: 2223684.

22. Excellence NNIfHaC. Ovarian cancer: recognition and initial management Apr 2011 [Feb 2016]. Available from: https://www.nice.org.uk/guidance/cg122/chapter/1-Guidance#management-of-advanced-stage-iiiv-ovarian-cancer.

23. Oikkonen J, Zhang K, Salminen L, Schulman I, Lavikka K, Andersson N, et al. Prospective Longitudinal ctDNA Workflow Reveals Clinically Actionable Alterations in Ovarian Cancer. 2019;3:1-12.

24. Valentini AL, Gui B, Miccò M, Mingote M, De Gaetano A, Ninivaggi V, et al. Benign and suspicious ovarian masses—MR imaging criteria for characterization: Pictorial review. 2012;2012.
25. Jung SE, Lee JM, Rha SE, Byun JY, Jung JI, Hahn STJR. CT and MR imaging of ovarian tumors with emphasis on differential diagnosis. 2002;22(6):1305-25.
26. Timmerman D, Ameye L, Fischerova D, Epstein E, Melis GB, Guerriero S, et al. Simple ultrasound rules to distinguish between benign and malignant adnexal masses before surgery: prospective validation by IOTA group. 2010;341:c6839.
27. Bazot M, Daraï E, Nassar-Slaba J, Lafont C, Thomassin-Naggara IJJocat. Value of magnetic resonance imaging for the diagnosis of ovarian tumors: a review. 2008;32(5):712-23.
28. Jacobs I, Oram D, Fairbanks J, Turner J, Frost C, Grudzinskas JJBAIJoO, et al. A risk of malignancy index incorporating CA 125, ultrasound and menopausal status for the accurate preoperative diagnosis of ovarian cancer. 1990;97(10):922-9.
29. Petricoin III EF, Ardekani AM, Hitt BA, Levine PJ, Fusaro VA, Steinberg SM, et al. Use of proteomic patterns in serum to identify ovarian cancer. 2002;359(9306):572-7.
30. Pomel C, Jeyarajah A, Oram D, Shepherd J, Milliken D, Dauplat J, et al. Cytoreductive surgery in ovarian cancer. 2007;7(1):210.
31. Makar AP, Tropé CG, Tummers P, Denys H, Vandecasteele KJTo. Advanced ovarian cancer: primary or interval debulking? Five categories of patients in view of the results of randomized trials and tumor biology: primary debulking surgery and interval debulking surgery for advanced ovarian cancer. 2016;21(6):745-54.
32. Malpica A, Deavers MT, Lu K, Bodurka DC, Atkinson EN, Gershenson DM, et al. Grading ovarian serous carcinoma using a two-tier system. 2004;28(4):496-504.
33. Ayhan A, Kurman RJ, Vang R, Logani S, Seidman JD, Shih I-MJTAjosp. Defining the cut-point between low-and high-grade ovarian serous carcinomas: a clinicopathologic and molecular genetic analysis. 2009;33(8):1220.
34. Gershenson DM, Sun CC, Lu KH, Coleman RL, Sood AK, Malpica A, et al. Clinical behavior of stage II-IV low-grade serous carcinoma of the ovary. 2006;108(2):361-8.
35. Santillan A, Kim Y, Zahurak M, Gardner G, Giuntoli R, Shih I, et al. Differences of chemoresistance assay between invasive micropapillary/low-grade serous ovarian carcinoma and high-grade serous ovarian carcinoma. 2007;17(3):601-6.
36. Holschneider CH, Berek JS. Ovarian cancer: epidemiology, biology, and prognostic factors. Semin Surg Oncol. 2000;19(1):3-10. PubMed PMID: 10883018.
37. Ries LA. Ovarian cancer. Survival and treatment differences by age. Cancer. 1993;71(2 Suppl):524-9. PubMed PMID: 8420672.

38. UK CR. Five-Year Relative Survival (%) by Stage, Adults Aged 15-99, Former Anglia Cancer Network.

39. Rubin SC, Randall TC, Armstrong KA, Chi DS, Hoskins WJ. Ten-year follow-up of ovarian cancer patients after second-look laparotomy with negative findings. Obstet Gynecol. 1999;93(1):21-4. PubMed PMID: 9916949.

40. Forstner R, Sala E, Kinkel K, Spencer JAJEr. ESUR guidelines: ovarian cancer staging and follow-up. 2010;20(12):2773-80.

41. Leeson S, Stuart N, Sylvestre Y, Hall L, Whitaker RJBo. Gynaecological cancer follow-up: national survey of current practice in the UK. 2013;3(7):e002859.

42. Kew F, Cruickshank DJIJoGC. Routine follow-up after treatment for a gynecological cancer: a survey of practice. 2006;16(1):380-4.

43. Jensen, J.H. and Helpern, J.A., 2010. MRI quantification of non-Gaussian water diffusion by kurtosis analysis. NMR in Biomedicine, 23(7), pp.698-710.

44. Madelin G, Regatte RRJJoMRI. Biomedical applications of sodium MRI in vivo. 2013;38(3):511-29.

45. Stobbe R, Beaulieu CJMRiMAOJotISfMRiM. In vivo sodium magnetic resonance imaging of the human brain using soft inversion recovery fluid attenuation. 2005;54(5):1305-10.

46. Nagel AM, Amarteifio E, Lehmann-Horn F, Jurkat-Rott K, Semmler W, Schad LR, et al. 3 Tesla sodium inversion recovery magnetic resonance imaging allows for improved visualization of intracellular sodium content changes in muscular channelopathies. 2011;46(12):759-66.

47. Leslie TK, James AD, Zaccagna F, Grist JT, Deen S, Kennerley A, et al. Sodium homeostasis in the tumour microenvironment. 2019.

48. Madelin G, Kline R, Walvick R, Regatte RR. A method for estimating intracellular sodium concentration and extracellular volume fraction in brain in vivo using sodium magnetic resonance imaging. Scientific reports. 2014;4:4763. doi: 10.1038/srep04763. PubMed PMID: 24755879; PubMed Central PMCID: PMC4762219.

49. Kaplan JH. Biochemistry of Na,K-ATPase. Annual review of biochemistry. 2002;71:511-35. doi: 10.1146/annurev.biochem.71.102201.141218. PubMed PMID: 12045105.

50. Brezis M, Rosen S. Hypoxia of the renal medulla--its implications for disease. The New England journal of medicine. 1995;332(10):647-55. doi: 10.1056/NEJM199503093321006. PubMed PMID: 7845430.

51. Suhail M. Na, K-ATPase: Ubiquitous Multifunctional Transmembrane Protein and its Relevance to Various Pathophysiological Conditions. Journal of clinical medicine research.

2010;2(1):1-17. doi: 10.4021/jocmr2010.02.263w. PubMed PMID: 22457695; PubMed Central PMCID: PMC3299169.

52. Petrushanko IY, Bogdanov NB, Lapina N, Boldyrev AA, Gassmann M, Bogdanova AY. Oxygen-induced Regulation of Na/K ATPase in cerebellar granule cells. The Journal of general physiology. 2007;130(4):389-98. doi: 10.1085/jgp.200709783. PubMed PMID: 17893192; PubMed Central PMCID: PMC2151649.

53. Hay N. Reprogramming glucose metabolism in cancer: can it be exploited for cancer therapy? Nature reviews Cancer. 2016;16(10):635-49. doi: 10.1038/nrc.2016.77. PubMed PMID: 27634447; PubMed Central PMCID: PMC5516800.

54. Annibaldi A, Widmann C. Glucose metabolism in cancer cells. Current opinion in clinical nutrition and metabolic care. 2010;13(4):466-70. doi: 10.1097/MCO.0b013e32833a5577. PubMed PMID: 20473153.

55. Pauwels EK, Ribeiro MJ, Stoot JH, McCready VR, Bourguignon M, Maziere B. FDG accumulation and tumor biology. Nuclear medicine and biology. 1998;25(4):317-22. PubMed PMID: 9639291.

56. Vansteenkiste JF. PET scan in the staging of non-small cell lung cancer. Lung cancer. 2003;42 Suppl 1:S27-37. PubMed PMID: 14611912.

57. Brown JM. Tumor hypoxia in cancer therapy. Methods in enzymology. 2007;435:297-321. doi: 10.1016/S0076-6879(07)35015-5. PubMed PMID: 17998060.

58. Costache MI, Ioana M, Iordache S, Ene D, Costache CA, Saftoiu A. VEGF Expression in Pancreatic Cancer and Other Malignancies: A Review of the Literature. Romanian journal of internal medicine = Revue roumaine de medecine interne. 2015;53(3):199-208. doi: 10.1515/rjim-2015-0027. PubMed PMID: 26710495.

59. Ferrer FA, Miller LJ, Andrawis RI, Kurtzman SH, Albertsen PC, Laudone VP, et al. Vascular endothelial growth factor (VEGF) expression in human prostate cancer: in situ and in vitro expression of VEGF by human prostate cancer cells. The Journal of urology. 1997;157(6):2329-33. PubMed PMID: 9146665.

60. Masoumi Moghaddam S, Amini A, Morris DL, Pourgholami MH. Significance of vascular endothelial growth factor in growth and peritoneal dissemination of ovarian cancer. Cancer metastasis reviews. 2012;31(1-2):143-62. doi: 10.1007/s10555-011-9337-5. PubMed PMID: 22101807; PubMed Central PMCID: PMC3350632.

61. Yancopoulos GD, Davis S, Gale NW, Rudge JS, Wiegand SJ, Holash JJN. Vascular-specific growth factors and blood vessel formation. 2000;407(6801):242.

62. Kowluru R, Bitensky MW, Kowluru A, Dembo M, Keaton PA, Buican T. Reversible sodium pump defect and swelling in the diabetic rat erythrocyte: effects on filterability and implications for microangiopathy. Proceedings of the National Academy of Sciences of the United States of America. 1989;86(9):3327-31. PubMed PMID: 2541440; PubMed Central PMCID: PMC287125.

63. Takeuchi A, Tatsumi S, Sarai N, Terashima K, Matsuoka S, Noma A. Ionic mechanisms of cardiac cell swelling induced by blocking Na+/K+ pump as revealed by experiments and simulation. The Journal of general physiology. 2006;128(5):495-507. doi: 10.1085/jgp.200609646. PubMed PMID: 17074975; PubMed Central PMCID: PMC2151580.

64. Yu XM, Groveman BR, Fang XQ, Lin SX. THE ROLE OF INTRACELLULAR SODIUM (Na) IN THE REGULATION OF CALCIUM (Ca)-MEDIATED SIGNALING AND TOXICITY. Health. 2010;2(1):8-15. doi: 10.4236/health.2010.21002. PubMed PMID: 21243124; PubMed Central PMCID: PMC3020095.

65. Milhaud J. New insights into water–phospholipid model membrane interactions. Biochimica et Biophysica Acta (BBA)-Biomembranes. 2004;1663(1):19-51.

66. Henkelman R, Stanisz G, Graham S. Magnetization transfer in MRI: a review. NMR in biomedicine. 2001;14(2):57-64.

67. Mehta RC, Pike GB, Enzmann DR. Magnetization transfer magnetic resonance imaging: a clinical review. Top Magn Reson Imaging. 1996;8(4):214-30. PubMed PMID: 8870180.

68. Barrett T, McLean M, Priest AN, Lawrence EM, Patterson AJ, Koo BC, et al. Diagnostic evaluation of magnetization transfer and diffusion kurtosis imaging for prostate cancer detection in a re-biopsy population. European radiology. 2017:1-10.

69. Tozer DJ, Rees JH, Benton CE, Waldman AD, Jäger HR, Tofts PS. Quantitative magnetisation transfer imaging in glioma: preliminary results. NMR in biomedicine. 2011;24(5):492-8.

70. Bonini RHM, Zeotti D, Saraiva LAL, Trad CS, Filho JMS, Carrara HHA, et al. Magnetization transfer ratio as a predictor of malignancy in breast lesions: preliminary results. Magnetic Resonance in Medicine: An Official Journal of the International Society for Magnetic Resonance in Medicine. 2008;59(5):1030-4.

71. Heller SL, Moy L, Lavianlivi S, Moccaldi M, Kim S. Differentiation of malignant and benign breast lesions using magnetization transfer imaging and dynamic contrast-enhanced MRI. Journal of Magnetic Resonance Imaging. 2013;37(1):138-45.

72. Outwater E, Schnall MD, Braitman LE, Dinsmore B, Kressel H. Magnetization transfer of hepatic lesions: evaluation of a novel contrast technique in the abdomen. Radiology. 1992;182(2):535-40.

73. Martens MH, Lambregts, D.M., Papanikolaou, N., Alefantinou, S., Maas, M., Manikis, G.C., Marias, K., Riedl, R.G., Beets, G.L. and Beets-Tan, R.G., 2016. Magnetization transfer imaging to

assess tumour response after chemoradiotherapy in rectal cancer. European radiology, 26(2), pp.390-397.

74. Mehrabian H, Myrehaug, S., Soliman, H., Sahgal, A. and Stanisz, G.J., 2018. Quantitative magnetization transfer in monitoring glioblastoma (GBM) response to therapy. Scientific reports, 8(1), p.2475.

75. Zaccagna F, Grist JT, Deen SS, Woitek R, Lechermann LM, McLean MA, et al. Hyperpolarized carbon-13 magnetic resonance spectroscopic imaging: a clinical tool for studying tumour metabolism. 2018;91(1085):20170688.

76. Ardenkjær-Larsen JH, Fridlund B, Gram A, Hansson G, Hansson L, Lerche MH, et al. Increase in signal-to-noise ratio of> 10,000 times in liquid-state NMR. 2003;100(18):10158-63.

77. Thie JAJTJoNM. Understanding the standardized uptake value, its methods, and implications for usage. 2004;45(9):1431.

78. Tomasi G, Turkheimer F, Aboagye EJMI, Biology. Importance of quantification for the analysis of PET data in oncology: review of current methods and trends for the future. 2012;14(2):131-46.

79. Prakash P, Cronin CG, Blake MAJAJoR. Role of PET/CT in ovarian cancer. 2010;194(6):W464-W70.

80. Avril N, Sassen S, Schmalfeldt B, Naehrig J, Rutke S, Weber WA, et al. Prediction of response to neoadjuvant chemotherapy by sequential F-18-fluorodeoxyglucose positron emission tomography in patients with advanced-stage ovarian cancer. 2005;23(30):7445-53.

81. Thrall MM, DeLoia JA, Gallion H, Avril NJGo. Clinical use of combined positron emission tomography and computed tomography (FDG-PET/CT) in recurrent ovarian cancer. 2007;105(1):17-22.

82. Vergote I, Tropé CG, Amant F, Kristensen GB, Ehlen T, Johnson N, et al. Neoadjuvant chemotherapy or primary surgery in stage IIIC or IV ovarian cancer. New England Journal of Medicine. 2010;363(10):943-53.

83. Cooke SL, Ng CK, Melnyk N, Garcia MJ, Hardcastle T, Temple J, et al. Genomic analysis of genetic heterogeneity and evolution in high-grade serous ovarian carcinoma. Oncogene. 2010;29(35):4905-13. doi: 10.1038/onc.2010.245. PubMed PMID: 20581869; PubMed Central PMCID: PMC2933510.

84. Schwarz RF, Ng CK, Cooke SL, Newman S, Temple J, Piskorz AM, et al. Spatial and temporal heterogeneity in high-grade serous ovarian cancer: a phylogenetic analysis. PLoS medicine. 2015;12(2):e1001789. doi: 10.1371/journal.pmed.1001789. PubMed PMID: 25710373; PubMed Central PMCID: PMC4339382.

85. McGuire WP, Hoskins WJ, Brady MF, Kucera PR, Partridge EE, Look KY, et al. Cyclophosphamide and cisplatin compared with paclitaxel and cisplatin in patients with stage III and stage IV ovarian cancer. New England Journal of Medicine. 1996;334(1):1-6.

86. Piccart MJ, Bertelsen K, James K, Cassidy J, Mangioni C, Simonsen E, et al. Randomized intergroup trial of cisplatin–paclitaxel versus cisplatin–cyclophosphamide in women with advanced epithelial ovarian cancer: three-year results. Journal of the National Cancer Institute. 2000;92(9):699-708.

87. Banerjee S, Kaye SB, Ashworth A. Making the best of PARP inhibitors in ovarian cancer. Nature reviews Clinical oncology. 2010;7(9):508.

88. O'Malley DM, Richardson DL, Rheaume PS, Salani R, Eisenhauer EL, McCann GA, et al. Addition of bevacizumab to weekly paclitaxel significantly improves progression-free survival in heavily pretreated recurrent epithelial ovarian cancer. Gynecologic oncology. 2011;121(2):269-72.

89. Hodi FS, Mihm MC, Soiffer RJ, Haluska FG, Butler M, Seiden MV, et al. Biologic activity of cytotoxic T lymphocyte-associated antigen 4 antibody blockade in previously vaccinated metastatic melanoma and ovarian carcinoma patients. Proceedings of the National Academy of Sciences. 2003;100(8):4712-7.

90. Rosenkrantz AB, Oei M, Babb JS, Niver BE, Taouli BJJoMRI. Diffusion-weighted imaging of the abdomen at 3.0 Tesla: Image quality and apparent diffusion coefficient reproducibility compared with 1.5 Tesla. 2011;33(1):128-35.

91. Braithwaite AC, Dale BM, Boll DT, Merkle EMJR. Short-and midterm reproducibility of apparent diffusion coefficient measurements at 3.0-T diffusion-weighted imaging of the abdomen. 2009;250(2):459-65.

92. Sala E, Kataoka MY, Priest AN, Gill AB, McLean MA, Joubert I, et al. Advanced ovarian cancer: multiparametric MR imaging demonstrates response-and metastasis-specific effects. Radiology. 2012;263(1):149-59.

93. Jensen JH, Helpern JA, Ramani A, Lu H, Kaczynski K. Diffusional kurtosis imaging: the quantification of non-gaussian water diffusion by means of magnetic resonance imaging. Magnetic resonance in medicine. 2005;53(6):1432-40. doi: 10.1002/mrm.20508. PubMed PMID: 15906300.

94. Jensen JH, Helpern JAJNiB. MRI quantification of non-Gaussian water diffusion by kurtosis analysis. 2010;23(7):698-710.

95. Li HM, Zhao SH, Qiang JW, Zhang GF, Feng F, Ma FH, et al. Diffusion kurtosis imaging for differentiating borderline from malignant epithelial ovarian tumors: A correlation with Ki-67 expression. Journal of Magnetic Resonance Imaging. 2017;46(5):1499-506.

96. Sun K, Chen X, Chai W, Fei X, Fu C, Yan X, et al. Breast cancer: diffusion kurtosis MR imaging—diagnostic accuracy and correlation with clinical-pathologic factors. Radiology. 2015;277(1):46-55.
97. Jiang R, Jiang J, Zhao L, Zhang J, Zhang S, Yao Y, et al. Diffusion kurtosis imaging can efficiently assess the glioma grade and cellular proliferation. Oncotarget. 2015;6(39):42380.
98. Nishimura R, Osako T, Okumura Y, Hayashi M, Arima N. Clinical significance of Ki-67 in neoadjuvant chemotherapy for primary breast cancer as a predictor for chemosensitivity and for prognosis. Breast cancer. 2010;17(4):269-75.
99. Kamoi S, Ohaki Y, Okada S, Matsushita N, Kawamura T, Araki T. Mitotic index and ki-67 nuclear antigen labeling index as predictors of chemotherapy response in uterine cervical carcinoma. Gynecologic oncology. 2001;83(3):555-9.
100. Chen Y, Ren W, Zheng D, Zhong J, Liu X, Yue Q, et al. Diffusion kurtosis imaging predicts neoadjuvant chemotherapy responses within 4 days in advanced nasopharyngeal carcinoma patients. Journal of Magnetic Resonance Imaging. 2015;42(5):1354-61.
101. Deen SS, Priest AN, McLean MA, Gill AB, Brodie C, Crawford R, et al. Diffusion kurtosis MRI as a predictive biomarker of response to neoadjuvant chemotherapy in high grade serous ovarian cancer. 2019;9(1):10742.
102. Eisenhauer E, Therasse P, Bogaerts J, Schwartz L, Sargent D, Ford R, et al. New response evaluation criteria in solid tumours: revised RECIST guideline (version 1.1). European journal of cancer. 2009;45(2):228-47.
103. Verheijen R, Kuijpers H, Van Driel R, Beck J, Van Dierendonck J, Brakenhoff G, et al. Ki-67 detects a nuclear matrix-associated proliferation-related antigen. II. Localization in mitotic cells and association with chromosomes. Journal of Cell Science. 1989;92(4):531-40.
104. Choudhury M, Goyal S, Pujani M. A cytohistological study of Ki-67 expression in ovarian tumors. Indian Journal of Pathology and Microbiology. 2011;54(1):21.
105. Sugahara T, Korogi Y, Kochi M, Ikushima I, Shigematu Y, Hirai T, et al. Usefulness of diffusion-weighted MRI with echo-planar technique in the evaluation of cellularity in gliomas. Journal of magnetic resonance imaging. 1999;9(1):53-60.
106. Yoshikawa MI, Ohsumi S, Sugata S, Kataoka M, Takashima S, Mochizuki T, et al. Relation between cancer cellularity and apparent diffusion coefficient values using diffusion-weighted magnetic resonance imaging in breast cancer. Radiation medicine. 2008;26(4):222-6.
107. Nonomura Y, Yasumoto M, Yoshimura R, Haraguchi K, Ito S, Akashi T, et al. Relationship between bone marrow cellularity and apparent diffusion coefficient. Journal of Magnetic Resonance Imaging. 2001;13(5):757-60.

108. Jensen JH, Helpern JA, Ramani A, Lu H, Kaczynski K. Diffusional kurtosis imaging: The quantification of non-gaussian water diffusion by means of magnetic resonance imaging. Magnetic resonance in medicine. 2005;53(6):1432-40.
109. Delgado AF, Fahlström M, Nilsson M, Berntsson SG, Zetterling M, Libard S, et al. Diffusion kurtosis imaging of gliomas grades II and III-a study of perilesional tumor infiltration, tumor grades and subtypes at clinical presentation. Radiology and Oncology. 2017;51(2):121-9.
110. Wang Q, Li H, Yan X, Wu C-J, Liu X-S, Shi H-B, et al., editors. Histogram analysis of diffusion kurtosis magnetic resonance imaging in differentiation of pathologic Gleason grade of prostate cancer. Urologic Oncology: Seminars and Original Investigations; 2015: Elsevier.
111. Lawrence EM, Warren AY, Priest AN, Barrett T, Goldman DA, Gill AB, et al. Evaluating prostate cancer using fractional tissue composition of radical prostatectomy specimens and pre-operative diffusional kurtosis magnetic resonance imaging. PloS one. 2016;11(7):e0159652.
112. Knox RJ, Friedlos F, Lydall DA, Roberts JJ. Mechanism of cytotoxicity of anticancer platinum drugs: evidence that cis-diamminedichloroplatinum (II) and cis-diammine-(1, 1-cyclobutanedicarboxylato) platinum (II) differ only in the kinetics of their interaction with DNA. Cancer research. 1986;46(4 Part 2):1972-9.
113. Horwitz S. Taxol (paclitaxel): mechanisms of action. Annals of oncology: official journal of the European Society for Medical Oncology. 1994;5:S3-6.
114. Schmeler KM, Sun CC, Bodurka DC, Deavers MT, Malpica A, Coleman RL, et al. Neoadjuvant chemotherapy for low-grade serous carcinoma of the ovary or peritoneum. Gynecologic oncology. 2008;108(3):510-4.
115. Itamochi H, Kigawa J, Sugiyama T, Kikuchi Y, Suzuki M, Terakawa N. Low proliferation activity may be associated with chemoresistance in clear cell carcinoma of the ovary. Obstetrics & Gynecology. 2002;100(2):281-7.
116. Vaughan S, Coward JI, Bast Jr RC, Berchuck A, Berek JS, Brenton JD, et al. Rethinking ovarian cancer: recommendations for improving outcomes. Nature Reviews Cancer. 2011;11(10):719.
117. Kurman RJ, Shih I-M. The Origin and pathogenesis of epithelial ovarian cancer-a proposed unifying theory. The American journal of surgical pathology. 2010;34(3):433.
118. Vencken P, Kriege M, Hoogwerf D, Beugelink S, van der Burg M, Hooning M, et al. Chemosensitivity and outcome of BRCA1-and BRCA2-associated ovarian cancer patients after first-line chemotherapy compared with sporadic ovarian cancer patients. Annals of oncology. 2011;22(6):1346-52.

119. Safra T, Rogowski O, Muggia FM. The effect of germ-line BRCA mutations on response to chemotherapy and outcome of recurrent ovarian cancer. International Journal of Gynecological Cancer. 2014;24(3):488-95.
120. Righetti SC, Della Torre G, Pilotti S, Ménard S, Ottone F, Colnaghi MI, et al. A comparative study of p53 gene mutations, protein accumulation, and response to cisplatin-based chemotherapy in advanced ovarian carcinoma. Cancer Research. 1996;56(4):689-93.
121. Parrish TB, Fieno DS, Fitzgerald SW, Judd RM. Theoretical basis for sodium and potassium MRI of the human heart at 1.5 T. Magnetic resonance in medicine. 1997;38(4):653-61. PubMed PMID: 9324333.
122. Deen SS, Riemer F, McLean MA, Gill AB, Kaggie JD, Grist JT, et al. Sodium MRI with 3D-cones as a measure of tumour cellularity in high grade serous ovarian cancer. 2019;6:156-62.
123. Gurney PT, Hargreaves BA, Nishimura DG. Design and analysis of a practical 3D cones trajectory. Magnetic resonance in medicine. 2006;55(3):575-82. doi: 10.1002/mrm.20796. PubMed PMID: 16450366.
124. Riemer F, Solanky BS, Stehning C, Clemence M, Wheeler-Kingshott CA, Golay X. Sodium ((23)Na) ultra-short echo time imaging in the human brain using a 3D-Cones trajectory. Magma. 2014;27(1):35-46. doi: 10.1007/s10334-013-0395-2. PubMed PMID: 23900703; PubMed Central PMCID: PMC3912357.
125. Riemer F, McHugh D, Zaccagna F, Lewis D, McLean MA, Graves MJ, et al. Measuring Tissue Sodium Concentration: Cross-Vendor Repeatability and Reproducibility of 23Na-MRI Across Two Sites. 2019.
126. Miller AJ, Joseph PM. The use of power images to perform quantitative analysis on low SNR MR images. Magnetic resonance imaging. 1993;11(7):1051-6. PubMed PMID: 8231670.
127. Stollberger R, Wach P. Imaging of the active B1 field in vivo. Magnetic resonance in medicine. 1996;35(2):246-51. PubMed PMID: 8622590.
128. Cunningham CH, Pauly JM, Nayak KS. Saturated double-angle method for rapid B1+ mapping. Magnetic resonance in medicine. 2006;55(6):1326-33. doi: 10.1002/mrm.20896. PubMed PMID: 16683260.
129. Christensen JD, Barrere BJ, Boada FE, Vevea JM, Thulborn KR. Quantitative tissue sodium concentration mapping of normal rat brain. Magnetic resonance in medicine. 1996;36(1):83-9. PubMed PMID: 8795025.
130. Ouwerkerk R, Jacobs MA, Macura KJ, Wolff AC, Stearns V, Mezban SD, et al. Elevated tissue sodium concentration in malignant breast lesions detected with non-invasive 23Na MRI. Breast

cancer research and treatment. 2007;106(2):151-60. doi: 10.1007/s10549-006-9485-4. PubMed PMID: 17260093.

131. Nagel AM, Bock M, Hartmann C, Gerigk L, Neumann JO, Weber MA, et al. The potential of relaxation-weighted sodium magnetic resonance imaging as demonstrated on brain tumors. Invest Radiol. 2011;46(9):539-47. doi: 10.1097/RLI.0b013e31821ae918. PubMed PMID: 21577129.

132. Morse CB, Norquist BM, Harrell MI, Agnew KJ, Gray HJ, Urban RR, et al. Neoplastic cellularity is associated with clinical and molecular features of high-grade serous ovarian carcinoma. Gynecologic oncology. 2016;143(2):389-92.

133. Rajan R, Poniecka A, Smith TL, Yang Y, Frye D, Pusztai L, et al. Change in tumor cellularity of breast carcinoma after neoadjuvant chemotherapy as a variable in the pathologic assessment of response. Cancer. 2004;100(7):1365-73.

134. Ogston KN, Miller ID, Payne S, Hutcheon AW, Sarkar TK, Smith I, et al. A new histological grading system to assess response of breast cancers to primary chemotherapy: prognostic significance and survival. The Breast. 2003;12(5):320-7.

135. Audeh MW, Carmichael J, Penson RT, Friedlander M, Powell B, Bell-McGuinn KM, et al. Oral poly (ADP-ribose) polymerase inhibitor olaparib in patients with BRCA1 or BRCA2 mutations and recurrent ovarian cancer: a proof-of-concept trial. The Lancet. 2010;376(9737):245-51.

136. Burger RA, Brady MF, Bookman MA, Fleming GF, Monk BJ, Huang H, et al. Incorporation of bevacizumab in the primary treatment of ovarian cancer. New England Journal of Medicine. 2011;365(26):2473-83.

137. Pardoll DM. The blockade of immune checkpoints in cancer immunotherapy. Nature Reviews Cancer. 2012;12(4):252.

138. Milligan L, McBride B. Energy costs of ion pumping by animal tissues. The Journal of nutrition. 1985;115(10):1374-82.

139. Bogdanova A, Ogunshola OO, Bauer C, Nikinmaa M, Gassmann M. Molecular mechanisms of oxygen-induced regulation of Na+/K+ pump. Chemoreception: Springer; 2003. p. 231-8.

140. Modica-Napolitano JS, Singh KK. Mitochondrial dysfunction in cancer. Mitochondrion. 2004;4(5):755-62.

141. Zheng J. Energy metabolism of cancer: Glycolysis versus oxidative phosphorylation. Oncology letters. 2012;4(6):1151-7.

142. Hay N. Reprogramming glucose metabolism in cancer: can it be exploited for cancer therapy? Nature Reviews Cancer. 2016;16(10):635.

143. Fraser SP, Diss JK, Chioni A-M, Mycielska ME, Pan H, Yamaci RF, et al. Voltage-gated sodium channel expression and potentiation of human breast cancer metastasis. Clinical Cancer Research. 2005;11(15):5381-9.

144. Roger S, Rollin J, Barascu A, Besson P, Raynal P-I, Iochmann S, et al. Voltage-gated sodium channels potentiate the invasive capacities of human non-small-cell lung cancer cell lines. The international journal of biochemistry & cell biology. 2007;39(4):774-86.

145. Gillet L, Roger S, Besson P, Lecaille F, Gore J, Bougnoux P, et al. Voltage-gated sodium channel activity promotes cysteine cathepsin-dependent invasiveness and colony growth of human cancer cells. Journal of Biological Chemistry. 2009;284(13):8680-91.

146. J Reshkin S, A Cardone R, Harguindey S. Na+-H+ exchanger, pH regulation and cancer. Recent patents on anti-cancer drug discovery. 2013;8(1):85-99.

147. Schmierer K, Scaravilli F, Altmann DR, Barker GJ, Miller DH. Magnetization transfer ratio and myelin in postmortem multiple sclerosis brain. Ann Neurol. 2004;56(3):407-15. doi: 10.1002/ana.20202. PubMed PMID: 15349868.

148. Kabani NJ, Sled JG, Chertkow H. Magnetization transfer ratio in mild cognitive impairment and dementia of Alzheimer's type. Neuroimage. 2002;15(3):604-10. doi: 10.1006/nimg.2001.0992. PubMed PMID: 11848703.

149. Boss A, Martirosian P, Kuper K, Fierlbeck G, Claussen CD, Schick F. Whole-body magnetization transfer contrast imaging. J Magn Reson Imaging. 2006;24(5):1183-7. doi: 10.1002/jmri.20754. PubMed PMID: 17031816.

150. Rosenkrantz AB, Storey P, Gilet AG, Niver BE, Babb JS, Hajdu CH, et al. Magnetization transfer contrast-prepared MR imaging of the liver: inability to distinguish healthy from cirrhotic liver. Radiology. 2012;262(1):136-43. doi: 10.1148/radiol.11111043. PubMed PMID: 22114240.

151. Kumar V, Jagannathan NR, Kumar R, Thulkar S, Gupta SD, Hemal AK, et al. Evaluation of the role of magnetization transfer imaging in prostate: a preliminary study. Magn Reson Imaging. 2008;26(5):644-9. doi: 10.1016/j.mri.2008.01.030. PubMed PMID: 18436407.

152. Pazahr S, Blume I, Frei P, Chuck N, Nanz D, Rogler G, et al. Magnetization transfer for the assessment of bowel fibrosis in patients with Crohn's disease: initial experience. MAGMA. 2013;26(3):291-301. doi: 10.1007/s10334-012-0355-2. PubMed PMID: 23138635.

153. Kobayashi S, Takeda K, Sakuma H, Kinosada Y, Nakagawa T. Uterine neoplasms: magnetization transfer analysis of MR images. Radiology. 1997;203(2):377-82. doi: 10.1148/radiology.203.2.9114091. PubMed PMID: 9114091.

154. Vavasour IM, Clark CM, Li DK, Mackay AL. Reproducibility and reliability of MR measurements in white matter: clinical implications. Neuroimage. 2006;32(2):637-42. doi: 10.1016/j.neuroimage.2006.03.036. PubMed PMID: 16677833.

155. Schneider CA, Rasband WS, Eliceiri KW. NIH Image to ImageJ: 25 years of image analysis. Nat Methods. 2012;9(7):671-5. PubMed PMID: 22930834.

156. Everitt B. The Cambridge dictionary of statistics. Cambridge, UK ; New York: Cambridge University Press; 1998. viii, 360 p. p.

157. Bella J, Brodsky B, Berman HM. Hydration structure of a collagen peptide. Structure. 1995;3(9):893-906.

158. Harel A, Eliav U, Akselrod S, Navon G. Magnetization transfer based contrast for imaging denatured collagen. Journal of Magnetic Resonance Imaging: An Official Journal of the International Society for Magnetic Resonance in Medicine. 2008;27(5):1155-63.

159. Laurent D, Wasvary J, Yin J, Rudin M, Pellas TC, O'Byrne E. Quantitative and qualitative assessment of articular cartilage in the goat knee with magnetization transfer imaging. Magnetic resonance imaging. 2001;19(10):1279-86.

160. Levental KR, Yu H, Kass L, Lakins JN, Egeblad M, Erler JT, et al. Matrix crosslinking forces tumor progression by enhancing integrin signaling. Cell. 2009;139(5):891-906.

161. Fishbein KW, Gluzband YA, Kaku M, Ambia-Sobhan H, Shapses SA, Yamauchi M, et al. Effects of formalin fixation and collagen cross-linking on T2 and magnetization transfer in bovine nasal cartilage. Magnetic resonance in medicine. 2007;57(6):1000-11.

162. NERENBERG PS, SALSAS-ESCAT R, STULTZ CM. Collagen-a necessary accomplice in the metastatic process. Cancer Genomics-Proteomics. 2007;4(5):319-27.

163. Lu P, Weaver VM, Werb Z. The extracellular matrix: a dynamic niche in cancer progression. J Cell Biol. 2012;196(4):395-406.

164. Kalluri R, Zeisberg M. Fibroblasts in cancer. Nature Reviews Cancer. 2006;6(5):392.

165. Cho A, Howell VM, Colvin EK. The extracellular matrix in epithelial ovarian cancer–a piece of a puzzle. Frontiers in oncology. 2015;5:245.

166. Cheon D-J, Tong Y, Sim M-S, Dering J, Berel D, Cui X, et al. A collagen-remodeling gene signature regulated by TGF-β signaling is associated with metastasis and poor survival in serous ovarian cancer. Clinical cancer research. 2013.

167. Fang M, Yuan J, Peng C, Li Y. Collagen as a double-edged sword in tumor progression. Tumor Biology. 2014;35(4):2871-82.

168. Terranova V, Llotta L, Russo RG, Martin G. Role of laminin in the attachment and metastasis of murine tumor cells. Cancer research. 1982;42(6):2265-9.

169. Hunt G. The role of laminin in cancer invasion and metastasis. Pathobiology. 1989;57(3):165-76.

170. Chia J, Kusuma N, Anderson R, Parker B, Bidwell B, Zamurs L, et al. Evidence for a role of tumor-derived laminin-511 in the metastatic progression of breast cancer. The American journal of pathology. 2007;170(6):2135-48.

171. Givant-Horwitz V, Davidson B, Reich R. Laminin-induced signaling in tumor cells. Cancer letters. 2005;223(1):1-10.

172. Vracko R. Basal lamina scaffold-anatomy and significance for maintenance of orderly tissue structure: a review. The American journal of pathology. 1974;77(2):313.

173. Yang J, Weinberg RA. Epithelial-mesenchymal transition: at the crossroads of development and tumor metastasis. Developmental cell. 2008;14(6):818-29.

174. Kiyoshima T, Kobayashi I, Matsuo K, Ishibashi Y, Miyoshi A, Akashi Y, et al. Immunohistochemical localization of laminin, collagen type IV and heparan sulfate proteoglycan in human colorectal adenocarcinoma: correlation with local invasive pattern and lymph node metastasis. Acta histochemica et cytochemica. 1998;31(1):39-47.

175. Firth NA, Reade PC. The prognosis of oral mucosal squamous cell carcinomas: a comparison of clinical and histopathological grading and of laminin and type IV collagen staining. Australian dental journal. 1996;41(2):83-6.

176. Arlinghaus LR, Dortch RD, Whisenant JG, Kang H, Abramson RG, Yankeelov TEJT. Quantitative magnetization transfer imaging of the breast at 3.0 T: reproducibility in healthy volunteers. 2016;2(4):260.

177. Berry I, Barker GJ, Barkhof F, Campi A, Dousset V, Franconi JM, et al. A multicenter measurement of magnetization transfer ratio in normal white matter. 1999;9(3):441-6.

178. Gatenby RA, Gillies RJ. Why do cancers have high aerobic glycolysis? Nat Rev Cancer. 2004;4(11):891-9. doi: 10.1038/nrc1478. PubMed PMID: 15516961.

179. Warburg O. On the origin of cancer cells. Science. 1956;123(3191):309-14. PubMed PMID: 13298683.

180. Hirschhaeuser F, Sattler UG, Mueller-Klieser W. Lactate: a metabolic key player in cancer. Cancer research. 2011;71(22):6921-5.

181. Vander Heiden MG, Cantley LC, Thompson CB. Understanding the Warburg effect: the metabolic requirements of cell proliferation. Science. 2009;324(5930):1029-33. doi: 10.1126/science.1160809. PubMed PMID: 19460998; PubMed Central PMCID: PMC2849637.

182. Walenta S, Mueller-Klieser WF. Lactate: mirror and motor of tumor malignancy. Semin Radiat Oncol. 2004;14(3):267-74. doi: 10.1016/j.semradonc.2004.04.004. PubMed PMID: 15254870.

183. Walenta S, Wetterling M, Lehrke M, Schwickert G, Sundfør K, Rofstad EK, et al. High lactate levels predict likelihood of metastases, tumor recurrence, and restricted patient survival in human cervical cancers. Cancer research. 2000;60(4):916-21.

184. Dimopoulos MA, Barlogie B, Smith TL, Alexanian R. High serum lactate dehydrogenase level as a marker for drug resistance and short survival in multiple myeloma. Annals of internal medicine. 1991;115(12):931-5.

185. Koukourakis M, Giatromanolaki A, Sivridis E, Bougioukas G, Didilis V, Gatter K, et al. Lactate dehydrogenase-5 (LDH-5) overexpression in non-small-cell lung cancer tissues is linked to tumour hypoxia, angiogenic factor production and poor prognosis. British journal of cancer. 2003;89(5):877-85.

186. Koukourakis MI, Giatromanolaki A, Simopoulos C, Polychronidis A, Sivridis E. Lactate dehydrogenase 5 (LDH5) relates to up-regulated hypoxia inducible factor pathway and metastasis in colorectal cancer. Clinical & experimental metastasis. 2005;22(1):25-30.

187. Schneider RJ, Seibert K, Passe S, Little C, Gee T, Lee BJ, et al. Prognostic significance of serum lactate dehydrogenase in malignant lymphoma. Cancer. 1980;46(1):139-43.

188. Markert CL. Lactate Dehydrogenase Isozymes: Dissociation and Recombination of Subunits. Science. 1963;140(3573):1329-30. doi: 10.1126/science.140.3573.1329. PubMed PMID: 17802174.

189. Kolev Y, Uetake H, Takagi Y, Sugihara K. Lactate dehydrogenase-5 (LDH-5) expression in human gastric cancer: association with hypoxia-inducible factor (HIF-1α) pathway, angiogenic factors production and poor prognosis. Annals of surgical oncology. 2008;15(8):2336-44.

190. Le A, Cooper CR, Gouw AM, Dinavahi R, Maitra A, Deck LM, et al. Inhibition of lactate dehydrogenase A induces oxidative stress and inhibits tumor progression. Proceedings of the National Academy of Sciences. 2010;107(5):2037-42.

191. Mathupala SP, Colen CB, Parajuli P, Sloan AE. Lactate and malignant tumors: a therapeutic target at the end stage of glycolysis. J Bioenerg Biomembr. 2007;39(1):73-7. doi: 10.1007/s10863-006-9062-x. PubMed PMID: 17354062; PubMed Central PMCID: PMC3385854.

192. Halestrap AP, Price NT. The proton-linked monocarboxylate transporter (MCT) family: structure, function and regulation. Biochem J. 1999;343 Pt 2:281-99. PubMed PMID: 10510291; PubMed Central PMCID: PMC1220552.

193. Morris ME, Felmlee MA. Overview of the proton-coupled MCT (SLC16A) family of transporters: characterization, function and role in the transport of the drug of abuse gamma-hydroxybutyric acid. AAPS J. 2008;10(2):311-21. doi: 10.1208/s12248-008-9035-6. PubMed PMID: 18523892; PubMed Central PMCID: PMC2574616.

194. Harris T, Eliyahu G, Frydman L, Degani H. Kinetics of hyperpolarized 13C1-pyruvate transport and metabolism in living human breast cancer cells. Proc Natl Acad Sci U S A. 2009;106(43):18131-6. doi: 10.1073/pnas.0909049106. PubMed PMID: 19826085; PubMed Central PMCID: PMC2775348.
195. Golman K, in 't Zandt R, Thaning M. Real-time metabolic imaging. Proc Natl Acad Sci U S A. 2006;103(30):11270-5. doi: 10.1073/pnas.0601319103. PubMed PMID: 16837573; PubMed Central PMCID: PMC1544077.
196. Golman K, Petersson JS. Metabolic imaging and other applications of hyperpolarized 13C1. Acad Radiol. 2006;13(8):932-42. doi: 10.1016/j.acra.2006.06.001. PubMed PMID: 16843845.
197. Matoba S, Kang JG, Patino WD, Wragg A, Boehm M, Gavrilova O, et al. p53 regulates mitochondrial respiration. Science. 2006;312(5780):1650-3. doi: 10.1126/science.1126863. PubMed PMID: 16728594.
198. Baysal BE, Ferrell RE, Willett-Brozick JE, Lawrence EC, Myssiorek D, Bosch A, et al. Mutations in SDHD, a mitochondrial complex II gene, in hereditary paraganglioma. Science. 2000;287(5454):848-51. PubMed PMID: 10657297.
199. Astuti D, Latif F, Dallol A, Dahia PL, Douglas F, George E, et al. Gene mutations in the succinate dehydrogenase subunit SDHB cause susceptibility to familial pheochromocytoma and to familial paraganglioma. Am J Hum Genet. 2001;69(1):49-54. doi: 10.1086/321282. PubMed PMID: 11404820; PubMed Central PMCID: PMC1226047.
200. Altenberg B, Greulich KO. Genes of glycolysis are ubiquitously overexpressed in 24 cancer classes. Genomics. 2004;84(6):1014-20. doi: 10.1016/j.ygeno.2004.08.010. PubMed PMID: 15533718.
201. Fang J, Quinones QJ, Holman TL, Morowitz MJ, Wang Q, Zhao H, et al. The H+-linked monocarboxylate transporter (MCT1/SLC16A1): a potential therapeutic target for high-risk neuroblastoma. Mol Pharmacol. 2006;70(6):2108-15. doi: 10.1124/mol.106.026245. PubMed PMID: 17000864.
202. Koukourakis MI, Giatromanolaki A, Harris AL, Sivridis E. Comparison of metabolic pathways between cancer cells and stromal cells in colorectal carcinomas: a metabolic survival role for tumor-associated stroma. Cancer Res. 2006;66(2):632-7. doi: 10.1158/0008-5472.CAN-05-3260. PubMed PMID: 16423989.
203. Koukourakis MI, Giatromanolaki A, Sivridis E, Gatter KC, Harris AL. Lactate dehydrogenase 5 expression in operable colorectal cancer: strong association with survival and activated vascular endothelial growth factor pathway—a report of the Tumour Angiogenesis Research Group. Journal of clinical oncology. 2006;24(26):4301-8.

204. Day SE, Kettunen MI, Gallagher FA, Hu DE, Lerche M, Wolber J, et al. Detecting tumor response to treatment using hyperpolarized 13C magnetic resonance imaging and spectroscopy. Nat Med. 2007;13(11):1382-7. doi: 10.1038/nm1650. PubMed PMID: 17965722.

205. Witney TH, Kettunen MI, Day SE, Hu DE, Neves AA, Gallagher FA, et al. A comparison between radiolabeled fluorodeoxyglucose uptake and hyperpolarized (13)C-labeled pyruvate utilization as methods for detecting tumor response to treatment. Neoplasia. 2009;11(6):574-82, 1 p following 82. Epub 2009/06/02. PubMed PMID: 19484146; PubMed Central PMCID: PMCPMC2685446.

206. Nelson SJ, Kurhanewicz J, Vigneron DB, Larson PE, Harzstark AL, Ferrone M, et al. Metabolic imaging of patients with prostate cancer using hyperpolarized [1-(1)(3)C]pyruvate. Science translational medicine. 2013;5(198):198ra08. doi: 10.1126/scitranslmed.3006070. PubMed PMID: 23946197; PubMed Central PMCID: PMC4201045.

207. Albers MJ, Bok R, Chen AP, Cunningham CH, Zierhut ML, Zhang VY, et al. Hyperpolarized 13C lactate, pyruvate, and alanine: noninvasive biomarkers for prostate cancer detection and grading. Cancer Res. 2008;68(20):8607-15. doi: 10.1158/0008-5472.CAN-08-0749. PubMed PMID: 18922937; PubMed Central PMCID: PMC2829248.

208. Ozols RF, Garvin AJ, Costa J, Simon RM, Young RC. Advanced ovarian cancer correlation of histologic grade with response to therapy and survival. Cancer. 1980;45(3):572-81. doi: 10.1002/1097-0142(19800201)45:3<572::AID-CNCR2820450325>3.0.CO;2-3.

209. Park I, Bok R, Ozawa T, Phillips JJ, James CD, Vigneron DB, et al. Detection of early response to temozolomide treatment in brain tumors using hyperpolarized 13C MR metabolic imaging. 2011;33(6):1284-90.

210. Aggarwal R, Vigneron DB, Kurhanewicz JJEu. Hyperpolarized 1-[13C]-Pyruvate Magnetic Resonance Imaging Detects an Early Metabolic Response to Androgen Ablation Therapy in Prostate Cancer. 2017;72(6):1028-9.

211. Kurhanewicz J, Vigneron DB, Brindle K, Chekmenev EY, Comment A, Cunningham CH, et al. Analysis of cancer metabolism by imaging hyperpolarized nuclei: prospects for translation to clinical research. 2011;13(2):81-97.

212. Day SE, Kettunen MI, Cherukuri MK, Mitchell JB, Lizak MJ, Morris HD, et al. Detecting response of rat C6 glioma tumors to radiotherapy using hyperpolarized [1-13C] pyruvate and 13C magnetic resonance spectroscopic imaging. 2011;65(2):557-63.

213. Serrao EM, Brindle KMJFio. Potential clinical roles for metabolic imaging with hyperpolarized [1-13C] pyruvate. 2016;6:59.

214. Wiesinger F, Weidl E, Menzel MI, Janich MA, Khegai O, Glaser SJ, et al. IDEAL spiral CSI for dynamic metabolic MR imaging of hyperpolarized [1-13C] pyruvate. 2012;68(1):8-16.
215. Adalsteinsson E, Irarrazabal P, Topp S, Meyer C, Macovski A, Spielman DMJMrim. Volumetric spectroscopic imaging with spiral-based k-space trajectories. 1998;39(6):889-98.
216. Daniels CJ, McLean MA, Schulte RF, Robb FJ, Gill AB, McGlashan N, et al. A comparison of quantitative methods for clinical imaging with hyperpolarized 13C-pyruvate. 2016;29(4):387-99.
217. Schroeder MA, Cochlin LE, Heather LC, Clarke K, Radda GK, Tyler DJJPotNAoS. In vivo assessment of pyruvate dehydrogenase flux in the heart using hyperpolarized carbon-13 magnetic resonance. 2008;105(33):12051-6.
218. Serrao EM, Rodrigues TB, Gallagher FA, Kettunen MI, Kennedy BW, Vowler SL, et al. Effects of fasting on serial measurements of hyperpolarized [1-13C] pyruvate metabolism in tumors. 2016;29(8):1048-55.
219. Domcke S, Sinha R, Levine DA, Sander C, Schultz N. Evaluating cell lines as tumour models by comparison of genomic profiles. Nat Commun. 2013;4:2126. doi: 10.1038/ncomms3126. PubMed PMID: 23839242; PubMed Central PMCID: PMC3715866.
220. Alano CC, Garnier P, Ying W, Higashi Y, Kauppinen TM, Swanson RA. NAD+ depletion is necessary and sufficient for poly(ADP-ribose) polymerase-1-mediated neuronal death. J Neurosci. 2010;30(8):2967-78. doi: 10.1523/JNEUROSCI.5552-09.2010. PubMed PMID: 20181594; PubMed Central PMCID: PMC2864043.
221. Ma Y, Chen H, Xia W, Ying W. Oxidative stress and PARP activation mediate the NADH-induced decrease in glioma cell survival. Int J Physiol Pathophysiol Pharmacol. 2011;3(1):21-8. PubMed PMID: 21479099; PubMed Central PMCID: PMC3068850.
222. Stordal B, Timms K, Farrelly A, Gallagher D, Busschots S, Renaud M, et al. BRCA1/2 mutation analysis in 41 ovarian cell lines reveals only one functionally deleterious BRCA1 mutation. Mol Oncol. 2013;7(3):567-79. doi: 10.1016/j.molonc.2012.12.007. PubMed PMID: 23415752; PubMed Central PMCID: PMC4106023.
223. Fong PC, Boss DS, Yap TA, Tutt A, Wu P, Mergui-Roelvink M, et al. Inhibition of poly(ADP-ribose) polymerase in tumors from BRCA mutation carriers. N Engl J Med. 2009;361(2):123-34. doi: 10.1056/NEJMoa0900212. PubMed PMID: 19553641.
224. Ledermann J, Harter P, Gourley C, Friedlander M, Vergote I, Rustin G, et al. Olaparib maintenance therapy in platinum-sensitive relapsed ovarian cancer. N Engl J Med. 2012;366(15):1382-92. doi: 10.1056/NEJMoa1105535. PubMed PMID: 22452356.
225. Domcke S, Sinha R, Levine DA, Sander C, Schultz N. Evaluating cell lines as tumour models by comparison of genomic profiles. Nature communications. 2013;4.

226. Langdon SP, Lawrie SS, Hay FG, Hawkes MM, McDonald A, Hayward IP, et al. Characterization and properties of nine human ovarian adenocarcinoma cell lines. Cancer Res. 1988;48(21):6166-72. PubMed PMID: 3167863.

227. Gallagher FA, Bohndiek SE, Kettunen MI, Lewis DY, Soloviev D, Brindle KMJJoNM. Hyperpolarized 13C MRI and PET: in vivo tumor biochemistry. 2011;52(9):1333-6.

228. Witney T, Kettunen M, Hu D, Gallagher F, Bohndiek S, Napolitano R, et al. Detecting treatment response in a model of human breast adenocarcinoma using hyperpolarised [1-13 C] pyruvate and [1, 4-13 C 2] fumarate. 2010;103(9):1400.

229. Gutte H, Hansen AE, Henriksen ST, Johannesen HH, Ardenkjaer-Larsen J, Vignaud A, et al. Simultaneous hyperpolarized 13C-pyruvate MRI and 18F-FDG-PET in cancer (hyperPET): feasibility of a new imaging concept using a clinical PET/MRI scanner. 2015;5(1):38.

230. Khegai O, Schulte R, Janich M, Menzel M, Farrell E, Otto A, et al. Apparent rate constant mapping using hyperpolarized [1–13C] pyruvate. 2014;27(10):1256-65.

231. Witney TH, Kettunen MI, Day SE, Hu D-e, Neves AA, Gallagher FA, et al. A comparison between radiolabeled fluorodeoxyglucose uptake and hyperpolarized 13C-labeled pyruvate utilization as methods for detecting tumor response to treatment. 2009;11(6):IN11.

232. Gutte H, Hansen AE, Larsen M, Rahbek S, Henriksen ST, Johannesen HH, et al. Simultaneous hyperpolarized 13C-pyruvate MRI and 18F-FDG PET (HyperPET) in 10 dogs with cancer. 2015;56(11):1786-92.

233. Miloushev VZ, Granlund KL, Boltyanskiy R, Lyashchenko SK, DeAngelis LM, Mellinghoff IK, et al. Metabolic Imaging of the Human Brain with Hyperpolarized 13C Pyruvate Demonstrates 13C Lactate Production in Brain Tumor Patients. 2018:canres. 0221.2018.

234. Yüce K, Baykal C, Genc C, Al A, Ayhan AJEjogo. Diagnostic and prognostic value of serum and peritoneal fluid lactate dehydrogenase in epithelial ovarian cancer. 2001;22(3):228-32.

235. Koukourakis MI, Kontomanolis E, Giatromanolaki A, Sivridis E, Liberis VJG, investigation o. Serum and tissue LDH levels in patients with breast/gynaecological cancer and benign diseases. 2009;67(3):162-8.

236. Schwarz RF, Ng CK, Cooke SL, Newman S, Temple J, Piskorz AM, et al. Spatial and temporal heterogeneity in high-grade serous ovarian cancer: a phylogenetic analysis. PLoS medicine. 2015;12(2):e1001789.

237. Tofts P. Quantitative MRI of the brain: measuring changes caused by disease: John Wiley & Sons; 2005.

238. Kaggie J, Deen S, Schulte R, Addley H, Sala E, Brenton J, et al. Feasibility of Quantitative Magnetic Resonance Fingerprinting in Ovarian Tumours for T1and T2Mapping. 2019.

239. Ma D, Gulani V, Seiberlich N, Liu K, Sunshine JL, Duerk JL, et al. Magnetic resonance fingerprinting. Nature. 2013;495(7440):187-92.
240. Jiang Y, Ma D, Keenan KE, Stupic KF, Gulani V, Griswold MA. Repeatability of magnetic resonance fingerprinting T1 and T2 estimates assessed using the ISMRM/NIST MRI system phantom. Magnetic Resonance in Medicine. 2017;78(4):1452-7.
241. Jiang Y, Ma D, Seiberlich N, Gulani V, Griswold MA. MR fingerprinting using fast imaging with steady state precession (FISP) with spiral readout. Magnetic Resonance in Medicine. 2015;74(6):1621-31.
242. Gallagher FA, Kettunen MI, Hu D-E, Jensen PR, Karlsson M, Gisselsson A, et al. Production of hyperpolarized [1, 4-13C2] malate from [1, 4-13C2] fumarate is a marker of cell necrosis and treatment response in tumors. Proceedings of the National Academy of Sciences. 2009;106(47):19801-6.